Search for Magnetic Monopoles with the NOνA Far Detector

Zukai Wang

Ningbo, Zhejiang, China

B.S., Lanzhou University, 2009

A Dissertation presented to the Graduate Faculty

of the University of Virginia in Candidacy for the Degree of

Doctor of Philosophy

Department of Physics

University of Virginia

November, 2015

Abstract

The magnetic monopole is a hypothetical particle, which is an important field configuration in many Grand Unified Theories, and whose mass may vary from 10^4 to 10^{18} GeV. The quantization of magnetic charge derived by Dirac in 1931 suggests the heavy ionization nature of magnetic monopoles. The NOνA collaboration is using the NOνA far detector – the largest scintillator detector in the world – to search for signals of relic monopoles that might have been produced in the early universe. To achieve this, we have simulated the propagation of non-relativistic monopoles with a uniform distribution of velocity within the range $10^{-4} \lesssim \beta \lesssim 0.2$, and the corresponding detector response. To record potential monopole-like events, we have developed a data-driven trigger system with two monopole triggers (the fast monopole trigger and the slow monopole trigger). This analysis focuses on the data recorded by the fast monopole trigger, which is sensitive to monopoles with velocity $\beta \gtrsim 10^{-3}$. We have performed a blind analysis on a total live time of 1628.2 hours of data recorded by the fast monopole trigger. We present the updated flux limits with 90% CL (confidence level) as a function of monopole mass and velocity.

We approve the dissertation of Zukai Wang.

Supervisor: Prof. Craig Dukes	Date
Committee Member: Prof. Bob Hirosky	Date
Committee Member: Prof. P.Q. Huang	Date
Committee Member: Prof. Edward Murphy	Date

Acknowledgements

My advisor, Professor Craig E Dukes, suggested searching for magnetic monopoles as my thesis topic. Though this gradually turned out to be a long and difficult work beyond my original expectation, I am deeply grateful to his decision with his experience and great insight in physics. As the challenges of modern physics are achieved one by one, the remaining tasks for young graduate students to choose are somehow becoming more and more restricted in one specific and limited area. However, magnetic monopoles, which did not arise my interest in my undergraduate years, turned out more and more appealing. The broad coverage of magnetic monopoles turned out to be beyond my original expectation as well. Thanks to this topic, I got the chance to work on many aspects of an experiment, including simulation, trigger, reconstruction and analysis. This work also pushed me to go through the elegant theoretical work done by previous generations of great physicists. Reading the history of physicists' efforts in searching for magnetic monopoles in various ways also turned out to be a great joy for me after work.

I also owe a lot to my colleagues in NOνA and Fermilab fellows who supported this work. The co-chair of the NOνA exotics group, Professor Alec T. Habig, has given many useful suggestions throughout this thesis research work. Professor Habig is also a key role player in NOνA DAQ and data-driven trigger group. The monopole triggers could not have been implemented and run stably without his great effort and support. Great appreciation to Dr. Gavin Davis who helped me a lot in getting

familiar with NOνA software framework when I got started, Many thanks to Dr. Brian Rebel and Dr. Robert Hatcher, who helped me in setting up simulation of magnetic monopoles into the NOνA software framework. Many thanks to Dr. Chris Green, who was always willing to take my subtle coding questions and give me useful suggestions in algorithm designing.

Great support also came from my colleagues in UVa Intensity Frontier group: Professor Craig Group, Dr. Ralf Ehrlich and Dr. Yuri Oksuzian. The work would never have been finished without the helpful discussions and suggestions from them. Professor Group is also the convener in NOνA computing group, who helped a lot in getting the computing resources for me in monopole simulation and offline data reconstruction work. And finally, special thanks to Dr. Martin Frank and Dr. Andrew Norman, who were both my fellow colleagues and my partners who worked together in the data-driven trigger implementation. As the key players in the data-driven trigger group, we worked together to set up the entire framework from scratch starting in November of 2012. Within 17 months, two monopole triggers together with other data-driven triggers started running successfully on NOνA far detector. This came to be the best part of this thesis, and the most progressive part in my Ph.D. years.

Contents

1 Introduction to Magnetic Monopoles **2**

1.1 Magnetic Monopoles in Classical Electrodynamics 2

1.2 Quantization of Monopole Charge 4

1.3 Predictions of the Magnetic Monopole Mass 6

1.4 Magnetic Monopoles in Cosmology 8

1.5 Magnetic Monopole Detection Techniques 11

1.5.1 Induction 12

1.5.2 Catalysis of Proton Decay 15

1.5.3 Ionization 16

1.5.4 Summary of Monopole Energy Loss Calculations 21

1.6 Acceptance of Magnetic Monopoles In Surface Detectors 23

1.7 Present Limits on Magnetic Monopoles Searches 25

2 The NOνA Far Detector at Ash River **28**

2.1 Detector Design 28

2.2 Photodetector 31

2.3 Front End Electronics 31

2.4 The Data Acquisition System 36

2.4.1 Dual-Correlated-Sampling Triggering Algorithm 37

2.4.2 Nanoslice Format 38

2.4.3 The DAQ Data Formats 41
2.5 Single Cell Hit Calibration 42

3 Simulation of Magnetic Monopoles 49
3.1 Simulation of the Response of the Front-End Board 51
3.2 Isotropic Generator 55
3.3 Simulation of Monopole's Propagation 55
3.4 Light Yield Simulation 58
3.5 Cosmic Ray Simulation 61
3.6 The Monte Carlo Signal Data Set 62

4 The Fast Monopole Trigger 63
4.1 Introduction to the Data-Driven Trigger System 63
4.2 The Fast Monopole Trigger Algorithm 66
4.2.1 Slicing Algorithms for the Fast Monopole Trigger 67
4.2.2 Monte Carlo Tests of Space-time Slicing Performance and Efficiency 71
4.2.3 Fast Monopole Trigger Cuts 74
4.2.4 Fast Monopole Trigger Efficiency and Performance 79

5 Offline Reconstruction of Fast Monopole Tracks 83
5.1 Monopole Track Trajectory Reconstruction 84
5.2 Monopole Velocity Reconstruction 87
5.3 Reconstruction Validation 91

6 Offline Data Analysis 96
6.1 Data Selection and Live Time Calculation 96
6.2 Preselection Cuts 101
6.2.1 Cut 1: Saturated Hits Number 101

6.2.2 Cut 2: Track Fatness . . . 102
6.2.3 Cut 3: Velocity Validation . . . 105
6.2.4 Cut 4: Bremsstrahlung Rejection . . . 108
6.2.5 Cut 5: Maximum Gap Cuts . . . 111
6.2.6 Cut 6: Time Window for Non-relativistic Tracks . . . 112
6.2.7 Cut 7: Penetration . . . 113
6.2.8 Summary of Preselection Cuts . . . 113
6.3 Function Discriminant Analysis . . . 114
6.4 Background Prediction and Detection Efficiency . . . 121
6.5 Investigation of a Heavily Ionizing Flash Event . . . 124

7 Results **129**
7.1 Search Result . . . 129
7.2 Monopole Flux Upper Limits in NOνA . . . 129

8 Conclusions and Future Work **133**
8.1 Conclusion . . . 133
8.2 Future Work . . . 134

A Slow Magnetic Monopole Trigger **136**
A.1 Slow Monopole Trigger . . . 136
A.1.1 Triangle Algorithm of the Slow Monopole Trigger . . . 137
A.1.2 Triangle Algorithm Complexity and computation time . . . 143
A.1.3 Slow Monopole Trigger Efficiency and Performance . . . 144
A.2 Combined Monopole Trigger Efficiency and Performance . . . 145

Bibliography **151**

List of Figures

1.1 Classical illustration of positron-monopole scattering. 4

1.2 Result from ATLAS of searching for Dirac monopoles. 6

1.3 Illustration of induction detection of monopoles. 13

1.4 Induced current in the ring as a monopole passes through. 14

1.5 Diagram of proton decay catalyzed by monopole. 15

1.6 Illustration of detecting proton decay catalyzed by monopole in IceCube. 16

1.7 Illustration of modeling monopole energy loss in conductor. 20

1.8 The summary of energy loss theoretical calculation. 22

1.9 Exposure solid angle calculation illustration. 24

1.10 Exposure solid angle acceptance of the NOνA far detector. 25

1.11 Present non-relativistic monopole search limits. 27

2.1 The two NOνA detectors. 29

2.2 NOνA extrusion module layout. 30

2.3 Schematic layout of the FEB. 33

2.4 Simulated APD response to a muon hit. 34

2.5 Hit time fit illustration with DSO data 35

2.6 Topology of the NOνA data acquisition system. 37

2.7 The noise spectrum in DSO scan data. 38

2.8 Distribution of RMS of 2,000 ADC values of all channels. 39

2.9 Nanoslice format with 4 ADC samples of the amplifier waveform. . . 40
2.10 Illustration of improvements in time resolution after pulse fitting. . . 43
2.11 Comparison between the fitted pulse height and residual time of simulated hits with MC truth. 44
2.12 The DSO trace of a saturated hit in a channel of the far detector. . . 45
2.13 Timing resolution vs. number of samples per hit. 45
2.14 Attenuation curve for a typical channel in the far detector. 47
2.15 DCS value vs. corrected photo electron number 47
2.16 DSO scan trace and determination of threshold for a channel. 48

3.1 Event display of a simulated monopole track. 50
3.2 Traversal times for monopoles with different velocities. 51
3.3 Simulated monopole DSO traces. 52
3.4 Detector response simulation validation 54
3.5 Entry surface ID in isotropic simulation. 56
3.6 The local coordinate system setup. 56
3.7 Isotropic angular distribution of simulated monopoles. 57
3.8 Simulated slow monopole energy loss compared to theoretical prediction. 58
3.9 Energy loss of simulated slow monopoles with systematic uncertainty. 59
3.10 Visible energy fraction vs. monopole speed. 60
3.11 Saturated hits ratio vs. monopole speed 61

4.1 Schematic of the DAQ and DDT system. 64
4.2 Illustration of the trigger time window. 65
4.3 The event display of a simulated monopole event. 66
4.4 The event display of a real cosmic-ray event. 67
4.5 Flow chart of TimeSlice and its service modules. 68
4.6 Flow chart of SpaceSlice. 70

4.7 Purity and inclusiveness of monopole slices. 71
4.8 Slicing efficiency vs. monopole speed. 73
4.9 MC truth information of simulated monopoles that fail slicing. . . . 73
4.10 MC truth direction of simulated monopoles that failed slicing. 74
4.11 Overlapping space and time distribution of fast monopole slices for minimum-bias data. 74
4.12 The fraction of overlapping space and time of fast monopole slices for MC monopoles. 75
4.13 The distribution of the number of high-energy hits and mean DCS value per slice for minimum-bias data. 75
4.14 The distribution of the number of high-energy hits and mean DCS value per slice for MC monopoles. 75
4.15 Far detector hits DCS spectrum 80
4.16 The fast monopole trigger efficiency determined by Monte Carlo. . . . 81
4.17 Fast monopole trigger rates 82

5.1 Event display illustration of offline monopole track reconstruction of a simulated monopole. 84
5.2 Event display illustration of offline monopole track reconstruction of real cosmic-ray tracks in real data. 86
5.3 Illustration of the offline monopole velocity fit. 88
5.4 The time profile of all the modules related to the monopole triggers . 90
5.5 Distribution of the ratio of the reconstructed velocity to the true velocity. 91
5.6 Velocity reconstruction validation. 91
5.7 Entry position reconstruction validation. 92
5.8 Exit position reconstruction validation. 93
5.9 Visible energy reconstruction validation. 94

6.1 Typical distribution of the median MIP hit rate per cell per subrun. . 97
6.2 Typical distribution of the slices per subrun. 98
6.3 Typical distribution of the 2D only track fraction per subrun. 98
6.4 The fraction of active channels. 99
6.5 The live time fraction. 100
6.6 The corrected fast monopole trigger rate. 101
6.7 The saturated hits number distribution. 102
6.8 DCS spectrum of X and Y view hits. 103
6.9 Track fatness distribution. 104
6.10 Velocity fitting error distribution. 106
6.11 Statistical relative velocity uncertainty distribution. 107
6.12 Reconstructed $\beta_{sat}/\beta_{nonsat}$ distribution. 108
6.13 Reconstructed β distribution. 109
6.14 Event display of a high-energy muon with bremsstrahlung radiation. . 110
6.15 Reconstructed δ distribution. 110
6.16 The maximum gap cut. 111
6.17 The time window size distribution of slow ($\beta < 0.3$) tracks. 112
6.18 The distance between the entry (exit) hit in the track to the detector surface. 113
6.19 Monopole classification illustration. 115
6.20 Monopole identification output. 116
6.21 The FDA scores after preselection cut 1. 117
6.22 The FDA scores after preselection cut 1 and cut 2. 118
6.23 The FDA scores after preselection cut 1 through cut 3. 118
6.24 The FDA scores after preselection cut 1 through cut 4. 119
6.25 The FDA scores after the preselection cut 1 through cut 5. 119
6.26 The FDA scores after the preselection cut 1 through cut 6. 120

6.27 Correlation matrix of the two training variables, β and ρ. 120
6.28 Background prediction. 121
6.29 Number of years per event vs. FDA cut. 122
6.30 Final monopole detection efficiency. 123
6.31 Event display of an interesting heavily ionizing flash event. 125
6.32 Pattern of FEB flash hits. 126
6.33 Event display of the flash track. 126
6.34 Event display of a heavily ionizing flash event reconstructed in the slicer. 127

7.1 Control region check before box opening. 130
7.2 Final monopole flux upper limit. 132

8.1 Combined flux upper limits. 134

A.1 Illustration of the view check process in the slow monopole trigger. . 137
A.2 Illustration of the triangle algorithm. 138
A.3 Absolute difference of a true and calculated hit time. 140
A.4 Slow monopole trigger algorithm flow chart 142
A.5 Slow monopole trigger algorithm complexity vs. computation time . . 144
A.6 Slow monopole trigger efficiency with different DCS cuts 145
A.7 Slow monopole trigger rates 146
A.8 The combined efficiency of monopole triggers 147
A.9 The time profile of all the modules related to the monopole triggers . 147

List of Tables

1.1 Summary of predicted magnetic monopole properties. 11

1.2 Limits on the cosmic magnetic monopole flux from the MACRO experiment 26

2.1 Summary of the far detector geometry. 30

2.2 Surface areas of different detectors. 31

2.3 The composition of the NOνA liquid scintillator. 32

3.1 The rate of cosmic-ray particles entering NOνA far detector. 62

4.1 The list of parameters cut on for the fast monopole trigger. 78

4.2 Summary of trigger cuts performance 79

5.1 Uncertainties in the reconstructed trajectory points. 89

6.1 Summary of the preselection cuts performance 114

7.1 Tabulated monopole flux upper limits. 131

A.1 List of parameters in the slow monopole trigger. 141

Chapter 1

Introduction to Magnetic Monopoles

In this chapter we introduce the idea of the magnetic monopole starting from the context of classical electrodynamics, and briefly review the most profound theoretical concepts concerning magnetic monopoles in modern physics. Though they have never been discovered, the properties of monopoles are constrained by different theories and models, which determines the detection technologies that can be used to probe them. A brief summary of the current upper limit on the flux set by different experiments is also presented. Finally, we roughly calculate the acceptance of the NOνA detector for monopoles with a simple model.

1.1 Magnetic Monopoles in Classical Electrodynamics

Though the idea of the magnetic monopole is permitted in the framework of classic electrodynamics, the majority of physicists in 19th century ignored the possibility despite a more symmetric (and beautiful) form of the Maxwell Equations:

$$\nabla \cdot \vec{D} = 4\pi\rho_e \,, \tag{1.1a}$$

$$\nabla \cdot \vec{B} = 4\pi\rho_m \,, \tag{1.1b}$$

$$\nabla \times \vec{H} = \frac{1}{c}\frac{\partial \vec{D}}{\partial t} + \frac{4\pi}{c}\vec{J}_e \,, \tag{1.1c}$$

$$-\nabla \times \vec{E} = \frac{1}{c}\frac{\partial \vec{B}}{\partial t} + \frac{4\pi}{c}\vec{J}_m \,. \tag{1.1d}$$

Here ρ_e is the electric charge density, ρ_m is the magnetic charge density, $\vec{J}_e$ is the electric current density, and $\vec{J}_m$ is the magnetic current density.

Now consider the following duality transform to the electromagnetic charge densities:

$$\begin{bmatrix} \rho'_e \\ \rho'_m \end{bmatrix} = \begin{bmatrix} \cos\theta & -\sin\theta \\ \sin\theta & \cos\theta \end{bmatrix} \begin{bmatrix} \rho_e \\ \rho_m \end{bmatrix} . \tag{1.2}$$

Correspondingly, the current densities should be transformed in the same way:

$$\begin{bmatrix} \vec{J}'_e \\ \vec{J}'_m \end{bmatrix} = \begin{bmatrix} \cos\theta & -\sin\theta \\ \sin\theta & \cos\theta \end{bmatrix} \begin{bmatrix} \vec{J}_e \\ \vec{J}_m \end{bmatrix} . \tag{1.3}$$

If we apply the same transformation to the electromagnetic field as well, we find:

$$\begin{bmatrix} \vec{E}' & \vec{D}' \\ \vec{H}' & \vec{B}' \end{bmatrix} = \begin{bmatrix} \cos\theta & -\sin\theta \\ \sin\theta & \cos\theta \end{bmatrix} \begin{bmatrix} \vec{E} & \vec{D} \\ \vec{H} & \vec{B} \end{bmatrix} . \tag{1.4}$$

We find all the primed quantities still satisfy the generalized Maxwell Eqs. 1.1. The invariance of the Maxwell equations to the duality transform illustrates that it is a convention to set the charges of an electron to be $q_e = -e$ and $q_m = 0$. Thus, searching for magnetic monopoles is actually searching for another electromagnetic charge dimension.

Since $\vec{B}$ is odd under time reversal, ρ_m is a pseudo-scalar, which is revealed in Eq. 1.1b. Given that ρ_e is a scalar, any particle carrying both electric and magnetic charges, called a dyon, would naturally break symmetry under time reversal. This argument is given by D. Jackson [1]. He also notes in his book that "future developments may link electromagnetic, weak, and perhaps strong, interactions and utilize particles carrying magnetic charges as the vehicle for violation of space inversion and time reversal symmetries". At the same time (in 1974) when the second edition of this textbook was published, Hooft [2] and Polyakov [3] showed that magnetic monopoles are a necessary consequence of a class of theories, which are presently called Grand Unified Theories (GUTs).

1.2 Quantization of Monopole Charge

The concept of charge quantization can be derived semi-classically with a simple model. Consider a positron-monopole scattering problem in the framework of classical electrodynamics. For convenience, we set the coordinate system as illustrated in Fig. 1.1, and assume the impact parameter b is large enough that the positron is not deflected throughout its trajectory.

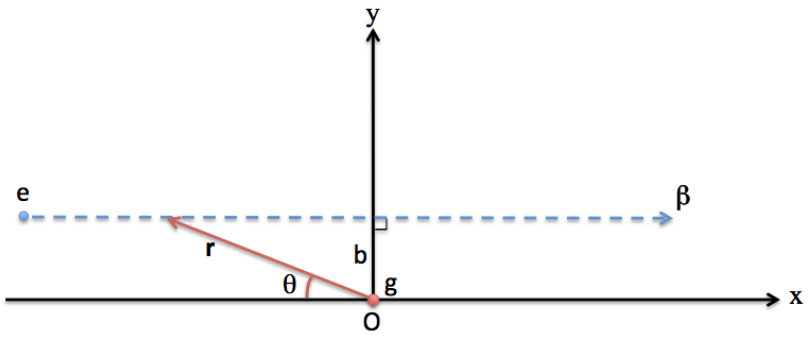

Figure 1.1: Illustration of positron-monopole scattering. A positron coming from $(-\infty, b)$ in the XY plane has an impact parameter b, with $\vec{\beta} = \beta\hat{\mathbf{e}}_\mathbf{x}$. A stationary magnetic monopole, with magnetic charge g, is sitting at the origin.

According to Eq. 1.1b, the magnetic field $\vec{B}$ generated by the magnetic monopole

is:

$$\vec{B} = -g\nabla\frac{1}{r}\,. \tag{1.5}$$

The overall impulse I from the magnetic monopole to the positron is in the z direction, with magnitude given by:

$$I = \int_{-\infty}^{\infty} e\beta B\sin\theta dt = \int_{0}^{\pi} \frac{e\beta g\sin\theta}{bc} d\theta = \frac{2eg}{bc}\,. \tag{1.6}$$

Using the same assumption Bohr applied to his hydrogen model: any change of angular momentum must occur in integral multiples of $\hbar$, we have

$$\Delta L = Ib = n\hbar\,. \tag{1.7}$$

Plugging this result into Eq. 1.6, we obtain the Dirac quantization condition:

$$2eg = n\hbar c\,. \tag{1.8}$$

This argument was first given by A.S. Goldhaber [4], and is included in D. Jackson's textbook [1] as well. The quantization condition was first derived by Dirac in 1931 by considering the phase change $\Delta\alpha$ of the wave function of an electron circulating around a infinitely long and infinitely thin solenoid, which is usually referred to as a Dirac string [5]:

$$\Delta\alpha = \frac{e}{\hbar c}\oint \vec{A}\cdot d\vec{l} = \frac{e}{\hbar c}4\pi g\,. \tag{1.9}$$

The phase change should be equal to $2n\pi$, which results in the same quantization condition given in Eq. 1.7. From the Eq. 1.8, we notice the magnetic charge is quantized in units of $\frac{1}{2\alpha}e \approx 68.5e$, which is usually referred to as the Dirac charge. A particle carrying a magnetic charge of 1 Dirac charge and 0 electric charge is referred to as Dirac monopole. This illustrates the fact that magnetic monopoles should be

heavily ionizing as shown by Bethe-Bloch formula, which states that the energy loss is proportional to the square of the charge of the particle. In the next section, we present the monopole energy loss in matter in detail.

1.3 Predictions of the Magnetic Monopole Mass

In the previous sections, we treated a magnetic monopole as a point magnetic charge both in the realm of classical electrodynamics and under the framework of quantum mechanics when deriving the Dirac's quantization condition. One of the most crucial questions remaining to be answered is: what is the mass of a monopole?

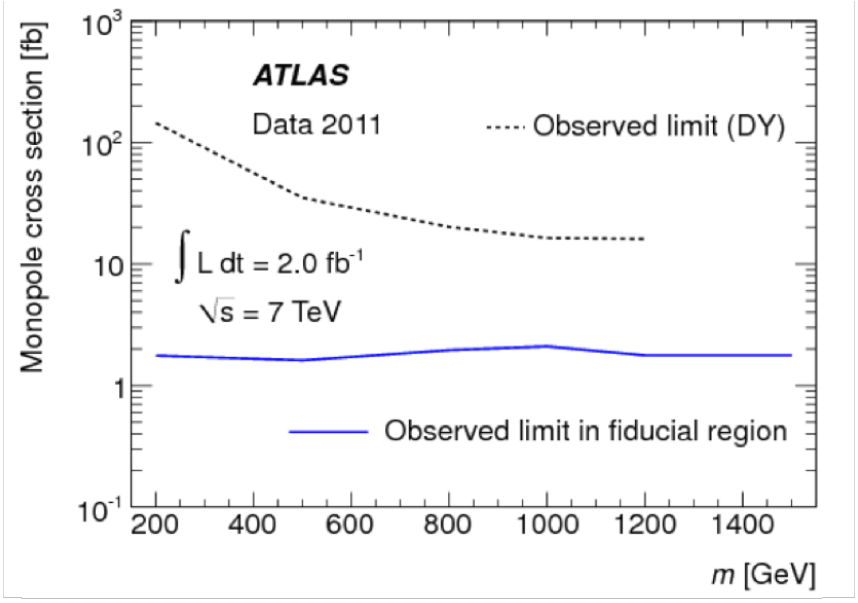

Figure 1.2: The upper limit of the cross section to produce magnetic monopoles at 95% CL measured by the ATLAS experiment, as a function of the monopole mass assuming one Dirac magnetic charge [7].

Like how most elementary particles are discovered, physicists have been searching for magnetic monopoles produced by colliders. The CDF collaboration performed a direct search for pair productions of monopoles with one Dirac magnetic charge, in $p\bar{p}$ collisions at a center-of-mass energy $\sqrt{s}$=1.96 TeV. They claim at 95% CL

that no monopoles with mass lower than 360 GeV exist, assuming a Drell-Yan pair-production mechanism [6]. The ATLAS collaboration performed a search at a even larger center-of-mass energy of $\sqrt{s}$=7 TeV [7]. Their result shown in Fig. 1.2, did not produce any evidence of monopole production.

In 1974, G. 't Hooft [2] showed that a magnetic monopole is a regular solution of the field equations within the context of SU(2). He predicted the monopole mass to be:

$$M_m = \frac{4\pi}{e^2} M_W C(\xi) = 137 M_W C(\xi)\,, \tag{1.10}$$

where $\xi = \frac{M_H^2}{M_W^2}$, M_H is the Higgs mass, and M_W is the intermediate boson mass. The function C is obtained numerically, and almost independent of the dimensionless parameter ξ. This intuitive work inspired later theoretical works in predicting monopoles in Grand Unified Theories.

The well-established, especially after the discovery of the Higgs boson, standard model is based on the $SU(3)_C \times [SU(2)_L \times U(1)_Y]$ where $SU(3)_C$ describes the gluon structure of QCD, and $[SU(2)_L \times U(1)_Y]$ describes the electroweak interactions. The invention of Grand Unified Theories was greatly inspired by the famous Glashow-Weinberg-Salam model which unifies the weak interaction and electromagnetic interaction via the breakdown of $[SU(2)_L \times U(1)_Y] \rightarrow U(1)_Q$ [8].

The basic idea of Grand Unified Theories (GUT) is very simple: try to find a simple group that unites the strong, weak and electromagnetic interactions above a sufficiently high mass scale M_X with a single coupling constant α_X. A typical Grand Unified Theory breaks down to the $SU(3)_C \times [SU(2)_L \times U(1)_Y]$ standard model at the mass scale M_X through the spontaneous symmetry breaking mechanism. Georgi and Glashow came to a conclusion, in 1974, that $SU(5)$ is "the gauge group of the

world" [9], which is the only simple[1] choice to be a Grand Unified Theory. Following their footsteps, Dokos and Tomaras [10] came up with an $SU(5)$ model with

$$SU_5 \xrightarrow{M_X} SU(3) \times SU(2) \times U(1)\,, \tag{1.11}$$

which has a monopole with charge $g = e/(2\alpha)$ and mass $M_m \sim 4\pi M_X/\alpha_X$. For a unification scale of 10^{16} GeV, the monopole would have a mass $M_m \sim 10^{17} - 10^{18}$ GeV [11].

1.4 Magnetic Monopoles in Cosmology

As mentioned above, a GUT monopole could be far more massive than the energy scale of any existing or foreseeable accelerators. However, monopoles could have been produced in the early universe described by the big bang theory. This theory describes the kinematics of the universe by the Robertson-Walker space-time metric and the dynamic evolution of the universe is governed by the Einstein-Friedman equations.[2] Immediately after the big bang, the universe went through a phase transition at a temperature $T_C \sim M_X$ (the typical mass of the gauge bosons of GUT). The Higgs field acquired vacuum expectation values pointed in different directions in the symmetry space in different domains within it that it remained correlated. The monopole configuration arose at the intersection points of several such domains [12] as a stable topological defect. Thus the number density of monopoles (n_M) in the early universe was of the order of:

$$n_M \sim \frac{1}{d_H^3} \sim \frac{T_C^6}{m_P^3}\,, \tag{1.12}$$

where d_H is the horizon, which corresponds to the maximum distance the light can travel after $t = 0$, and the Planck mass $m_P = 1.22 \times 10^{19}$ GeV/c^2. As the universe

[1] A group is considered simple if it contains no non-trivial invariant subgroups.
[2] This theory is also known as the standard cosmology.

expanded, the number density of monopoles should have dropped together with the entropy density, s:

$$\frac{n_M}{s} \sim \frac{T_C^3}{m_P^3}\,. \tag{1.13}$$

The value of entropy density today is about 10^3 cm^{-3} [13]. Meanwhile we can express the monopole mass density m_M in terms of the critical density $\rho_{critical}$:

$$\rho_M = \Omega_M \rho_{critical} = \frac{3H^2\Omega_M}{8\pi G}\,, \tag{1.14}$$

where G is the gravitational constant and Ω_M is the monopole mass fraction in the total matter mass of the universe. The Hubble constant H, characterizing the expansion rate of the universe, is usually expressed as:

$$H = \frac{100 \text{ km/s}}{Mpc} h\,. \tag{1.15}$$

Plugging the numerical expression for the critical density in Eq. 1.14, we have:

$$\rho_{critical} = 1.88 \times 10^{-29} \Omega_M h^2 (\text{g/cm}^3)\,. \tag{1.16}$$

The most recent measurement of the Hubble constant is from the Planck Collaboration [14], suggesting the value of h is about 0.678, indicating $\Omega_M h^2 < 0.46$ which leads to an upper limit of the monopole abundance. Since the mass of all the monopoles should not exceed the entire present matter mass of the universe, we obtain:

$$n_M \lesssim 0.5 \times 10^{-22} \left(\frac{10^{17} \text{ GeV}}{m_M}\right) \text{ cm}^{-3}\,. \tag{1.17}$$

This implies an upper limit on the monopole flux as well. Assuming the monopole flux is isotropic and every monopole is traveling with a same speed v_m, we have a

very simple relation between the monopole flux and the abundance:

$$F_M = \frac{n_M v_M}{4\pi} \,. \tag{1.18}$$

To determine the flux upper limit, we will need to estimate the velocity of monopoles.

The average galactic magnetic field $B \sim 3\mu$G would accelerate the monopoles to the following speed v_M depending on the monopole mass m_M [11]:

$$v_M \sim \begin{cases} c, & m_M \lesssim 10^{11} \ \text{GeV} \,, \\ 10^{-3} c \left(\dfrac{10^{17} \ \text{GeV}}{m_M} \right)^{1/2}, & m_M \gtrsim 10^{11} \ \text{GeV} \,. \end{cases} \tag{1.19}$$

This relation can be understood qualitatively by considering a very simple case. Assume a monopole with mass m_M and magnetic charge $g = 2e/\alpha$ was initially at rest and then accelerated by the galactic magnetic field B. The velocity of the monopole after traveling a distance of L would be:

$$v_M = \sqrt{\frac{2gBL}{m_M}} \sim 10^{-3} c \left(\frac{L}{10^{21} \ \text{cm}} \frac{10^{17} \ \text{GeV}}{m_M} \right)^{1/2} . \tag{1.20}$$

We can give an upper flux limit estimation by combining Eq. 1.17, Eq. 1.18, and Eq. 1.20 for monopoles with mass of 10^{17} GeV:

$$F_M(m_M = 10^{17} \ \text{GeV}) \lesssim 1.2 \times 10^{-16} (\ \text{cm}^{-2} \ \text{s}^{-1} \ \text{sr}^{-1}) \,. \tag{1.21}$$

This result is very close to the result obtained by Parker [15] in 1970:

$$F_M < \begin{cases} 10^{-15} \ \text{cm}^{-2} \ \text{s}^{-1} \ \text{sr}^{-1}, & m_M \lesssim 10^{17} \ \text{GeV} \,, \\ 10^{-15} \left(\dfrac{m_M}{10^{17} \ \text{GeV}} \ \text{cm}^{-2} \ \text{s}^{-1} \text{sr}^{-1} \right), & m_M \gtrsim 10^{17} \ \text{GeV} \,. \end{cases} \tag{1.22}$$

which is known as the Parker bound. Parker obtained this limit by comparing the energy loss rate of the galactic field consumed in accelerating the monopoles to the regeneration rate of the galactic field. Considering the evolution of the galactic field, a tighter bond has been obtained [16]:

$$F_M < \left(\frac{m_M}{10^{17}\ \text{GeV}} + 3 \times 10^{-6} \right) \times 10^{-16} (\ \text{cm}^{-2}\text{s}^{-1}\text{sr}^{-1}) \,. \tag{1.23}$$

Equation 1.23, known as the extended Parker bound, is coincidentally even closer to the result in Eq. 1.21 obtained by our naive model.

1.5 Magnetic Monopole Detection Techniques

Given the properties of magnetic monopoles (see Table 1.1) which have been briefly discussed in previous sections, physicists have designed various techniques to search for them. A lot of effort has been spent in the search of possible super massive big bang relics.

Table 1.1: Summary of predicted magnetic monopole properties.

Property	Quantity	Description
Magnetic Charge	$g = \frac{n}{2\alpha} e$	n is an integer.
Electronic Charge	$m \cdot e$	m is an integer. A particle carrying both electric and magnetic charges is usually referred to as a dyon.
Mass	$M_m = 1.4 \sim 10^{15}$ TeV	The lower mass limit is set by collider experiments while the upper mass limit varies in different models.
Velocity	Unknown	Possible to be any velocity below the speed of light and heavily dependent on mass.

All searches fall into three major categories: induction, ionization and proton decay catalysis, based on the detection techniques. These three categories correspond to three levels of model-dependence, from low to high respectively. Induction experiments search for any particles possessing magnetic charge, thus they are not model dependent. Most experiments searching for monopoles via their ionization assume the ionization energy loss of monopoles is significantly larger than minimum ionizing energy loss, due to the large magnitude of the magnetic charge which is suggested by the Dirac quantization condition. Those that do not require large ionization require a penetrating track that is subluminal. Experiments based on the assumption that magnetic monopoles can catalyze the proton decay (and of course, assuming protons do decay), are the most heavily model dependent. If a slowly moving monopole catalyzes proton decay, such experiments would observe a number of proton decays producing π_0s along the trajectory in sequential order, from which the velocity of the monopole can be reconstructed by the time-of-flight inside the detector.

1.5.1 Induction

This detection technique is based on the long-range electromagnetic interaction of the monopole with the microscopic state of a superconducting ring. Consider a magnetic monopole with magnetic charge g moving at velocity v along the axis perpendicular to and through the center of a superconducting ring of radius r, as illustrated in Fig. 1.3.

Applying the generalized Maxwell Eq. 1.1 and integrating over the area in the ring,

$$\iint_S (-\nabla \times \vec{E}) \cdot d\vec{S} = \iint_S \left(\frac{1}{c} \frac{\partial \vec{B}}{\partial t} + \frac{4\pi}{c} \vec{J_m} \right) \cdot d\vec{S} \,. \tag{1.24}$$

Assume at $t = 0$, the monopole passes through the ring center and applying Stokes's

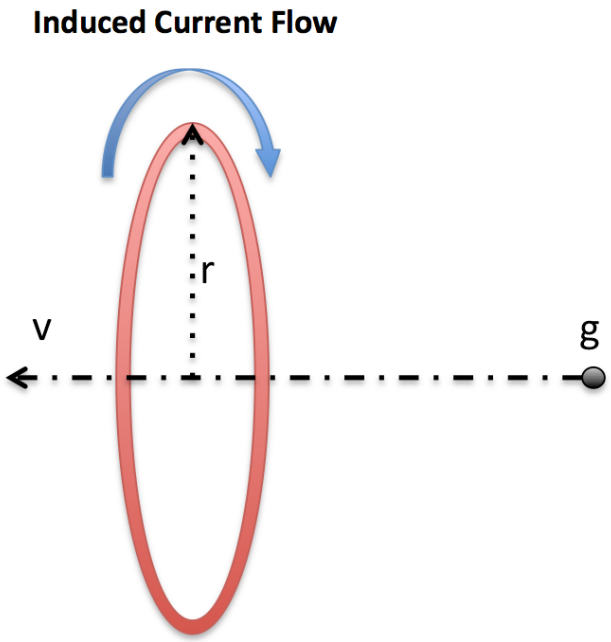

Figure 1.3: Illustration of the induced current from a magnetic monopole passing through a loop wire.

theorem to Eq. 1.24, we have:

$$-\oint_l \vec{E}\cdot\vec{l} = \frac{1}{c}\frac{\partial\phi}{\partial t} + \frac{4\pi}{c}g\delta(t)\,. \tag{1.25}$$

Being superconducting, the electric field $\vec{E}$ should vanish in the ring. Integrating Eq. 1.25 over the time period $(-\infty, t]$, gives the total flux through the ring as a function of time:

$$\Delta\phi(t) = -\frac{4\pi}{c}g\theta(t)\,, \tag{1.26}$$

where $\theta(t)$ is the step function. The flux $\Delta\phi$ consists of two parts: the monopole's contribution $\Delta\phi_g$ and the contribution from the induced current I, which is $\Delta\phi_s = -IL$, where L is the self-inductance of the ring. The monopole's contribution can be obtained by integrating the magnetic field generated by its magnetic charge over the

time interval:

$$\phi_g(t) = 2\pi g\left[1 - 2\theta(t) + \frac{\gamma v t}{\sqrt{(\gamma v t)^2 + r^2}}\right]. \tag{1.27}$$

Subtracting this part from the total flux through the ring at time t, we obtain the induced current as a function of time (see Fig. 1.4):

$$I(t) = \frac{2\pi g}{L}\left[1 + \frac{\gamma v t}{\sqrt{(\gamma v t)^2 + r^2}}\right]. \tag{1.28}$$

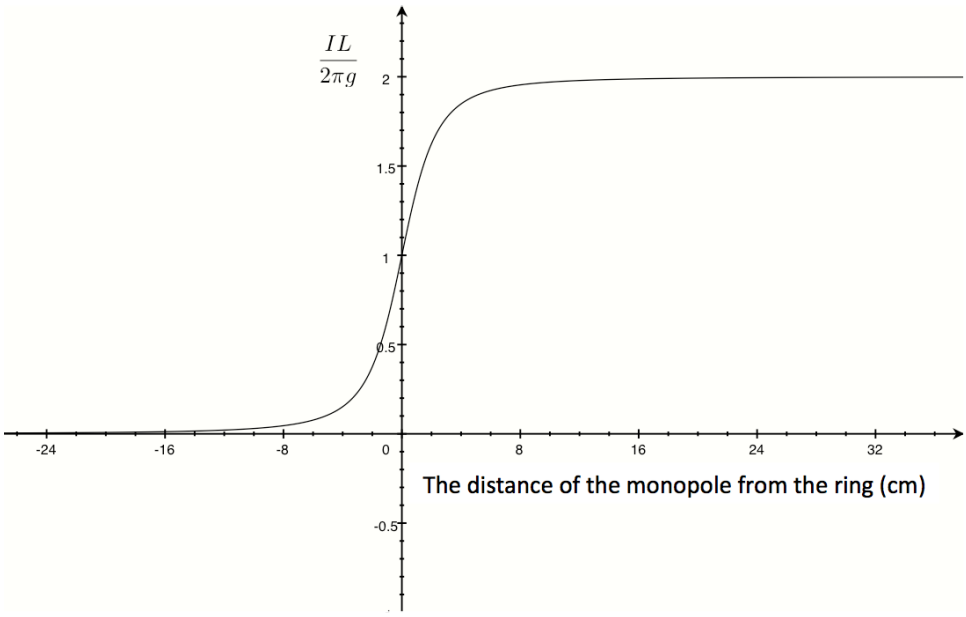

Figure 1.4: The quantity of $IL/(2\pi g)$ as a function of the monopole's distance from a superconductive ring with radius 2.5 cm.

Ideally, with a monopole traveling along the axis, one can check the Dirac quantization condition and measure the velocity of the monopole by measuring the induced current. Blas Cabrera and collaborators at Stanford University set up this kind of experiment with a four-turn, 5 cm-diameter loop, positioned with its axis vertical, connected to the superconducting input coil of a SQUID (superconducting quantum interference device) magnetometer [17]. He reported a single candidate event during the 151 days of running of his experiment in 1982, which was not con-

firmed. If this candidate event is considered to be spurious, his data set an upper limit of 6.1×10^{-10} cm^{-2} s^{-1} sr^{-1}, which is much larger than the Parker bound. This fact illustrates the largest difficulty in searching for monopoles with induction technology: it is hard to implement the demanding superconductive devices and technologies on large scales. The best limit given by an induction detector was obtained by the second generation Stanford detector. After running with 214 days as of Oct 4th, 1983, Blas Cabrera's group obtained a 90% CL limit on monopole flux of 2.1×10^{-11} cm^{-2} s^{-1} sr^{-1} [18].

1.5.2 Catalysis of Proton Decay

In the standard model protons are theoretically stable due to baryon number conservation. Some grand unified theories explicitly break baryon number conservation, and the rate of decay can be significantly increased by magnetic monopole, as illustrated in Fig. 1.5.

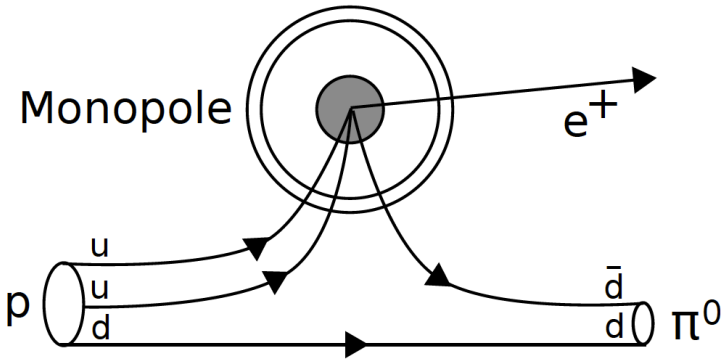

Figure 1.5: Illustration of a proton decay into a positron and a neutral pion catalyzed by a GUT monopole [19].

The possible capability of monopoles to catalyze proton decay would lead to striking experimental signatures. The IceCube experiment, using the detection of Cherenkov light from secondary charged particles, has performed a non-relativistic monopole

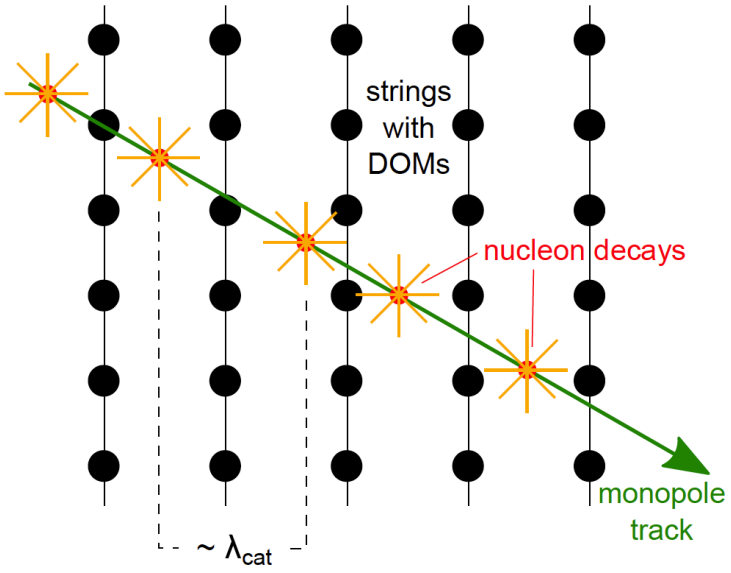

Figure 1.6: Illustration of the signature of a non-relativistic magnetic monopole (green) catalyzing nucleon decays (red) along its track in the IceCube experiment. The resulting nucleon decays are symbolized by orange rays [19].

search based on this assumption. If monopoles can catalyze proton decay, it will leave a track of neutral pions, as shown in Fig. 1.6.

Based on this assumption, the IceCube collaboration set a monopole flux upper limit to a level of $10^{-18}(10^{-17})$ cm^{-2} sr^{-1} s^{-1} at 90% CL for catalysis cross sections of $10^{-22}(10^{-24})$ cm^2 [19].

1.5.3 Ionization

Having discussed the most straightforward means of detecting magnetic monopoles by induction detectors, as well as the detection relying on the assumption that monopoles catalyze proton decay, we turn to the third means of detection: ionization. Any charged particle carrying electromagnetic charge will deposit some amount of energy by the ionization process and excitation of atoms when it is moving in matter. Thus scintillator, gas detectors, and nuclear track detectors, are sensitive to monopoles, as all fall into this category of detection technology. One disadvantage

of this detection technique is that it is difficult to tell whether a charged particle possesses magnetic charge solely from the energy deposit information. So a careful review of the theoretical models is necessary to predict the energy loss of monopole through matter and the light yield in the scintillator. And care must be taken in the analysis of the data to eliminate all other possible sources of such signatures.

To calculate the energy loss of monopoles passing through matter, we need to consider how the energy of the monopole is transferred to the surrounding medium. There are basically three ways where the energy can be dissipated:

- **Ionization** – The energy is transferred to the production of free electrons;
- **Atomic Excitation** – The energy is transferred to atoms of higher energy states;
- **Elastic Collisions with Atoms** – The energy is transferred to the kinematic momenta of atoms or nuclei.

The fraction of the energy loss of the three types depends only on the velocity of the monopole, assuming the mass of the monopole is very large compared to electrons or atoms. The ionizing energy dominates the total energy loss when the monopole is relativistic. At slower monopole speeds, atomic excitation starts to dominate the energy loss. If the monopole is very slow ($\beta < 10^{-4}$), it cannot excite atoms, and the energy loss is due to atoms (nuclei) recoiling. However, the cross section for atomic recoils is negligible and hence the energy loss is small. Few theoretical models predict monopoles with velocity $\beta < 10^{-4}$, thus we don't take the last type of energy loss into account.

Case 1: Relativistic Magnetic Monopoles

Consider the ionization energy loss for relativistic monopoles passing through matter. To simplify the problem, ignore the binding energy of electrons, and assume all the ionization energy loss is transferred to the kinetic energy ω of electrons. The electron production spectrum per unit length per unit energy is given by

$$\frac{dn}{d\omega dx} = \frac{4\pi N_{el}}{\omega_m}\frac{d\sigma}{d\Omega}\,, \tag{1.29}$$

where N_{el} is the electron density, $\omega_m = 2m_e c^2\beta^2\gamma^2$, is the classical kinematic limit of energy transfer, and $\frac{d\sigma}{d\Omega}$ is the total differential cross section in the ionization process. The ionization energy loss is given by

$$-\frac{dE}{dx} = \int_{\omega(b_{max})}^{\omega(b_{min})} \omega\frac{dn}{d\omega dx}d\omega\,, \tag{1.30}$$

where b is the impact parameter. The de Broglie wavelength of the electron in the center-of-momentum frame is the minimum value of b: $b_{min} = \hbar/m_e\gamma\beta c$. The maximum impact parameter is determined by the adiabatic limit: $b_{max} = \gamma\beta c/\omega$.

The cross section is calculated using Y. Kazama, C. N. Yang and A. S. Goldhaber's study [20] of the scattering of a spin-$\frac{1}{2}$ fermion by a fixed magnetic monopole. By using the tabulated values for the KYG (Kazama-Yang-Goldhaber) cross section, Ahlen [21] worked out the explicit form:

$$-\frac{dE}{dx} = \frac{4\pi N_{el}e^2g^2}{m_e c^2}\left[ln\left(\frac{2m_e c^2\beta^2\gamma^2}{I}\right) - \frac{K(|g|)}{2} - \frac{1}{2} - \frac{\delta}{2} - B(|g|)\right], \tag{1.31a}$$

$$B(g) = \begin{cases} 0.248, |g| = 137e/2 \\ 0.672, |g| = 137e \end{cases} \quad K(|g|) = \begin{cases} 0.406, |g| = 137e/2 \\ 0.346, |g| = 137e \end{cases}. \tag{1.31b}$$

I is the mean ionization potential, m_e is the electron mass and δ is the density

effect correction. This equation is consistent with the conjecture raised in the end of previous section, with the analogy to the Bethe-Bloch formula.

Case 2: Subluminal Magnetic Monopoles

Determining the energy loss of slow ($\beta \ll 1/137$) charged particles is much harder than calculating the energy loss of relativistic particles. One important reason for this is one can no longer neglect the binding energy of electrons and treat them as free, a basic approximation which was adopted by Beth [22] and Bloch [23]. Despite the difficulty, Fermi and Teller [24] first established a very simple model in 1947 to calculate the energy loss of a slow charged particle passing through matter, by modeling matter as a degenerate Fermi gas. To calculate the energy loss of slow monopoles, Ahlen and K. Kinoshita [25] further developed an approach by Lindhard [26] which uses the generalized Maxwell's equations to describe a degenerate Fermi gas. Another approach was taken in 1972 by Martem'yanov and Khakimov [27], who used a variant of a method given in Landau's textbook [28], and obtained the stopping power of slow monopoles in a conductor. These two independent (thanks to the cold war) and very different approaches surprisingly came to a good agreement.

Almost every theoretical calculation of the energy loss of slow charged particles leads to the following proportional relation to the velocity of the particle:

$$\frac{dE}{dx} = Cg^2\beta\,. \tag{1.32}$$

where the C is a material dependent constant and g is the electromagnetic charge the particle carries. This is what we use in the simulation for slow monopoles.

Instead of going through their detailed derivations, I present a very simple model to calculate magnetic monopoles energy loss in a conductor, as was first done by Ahlen

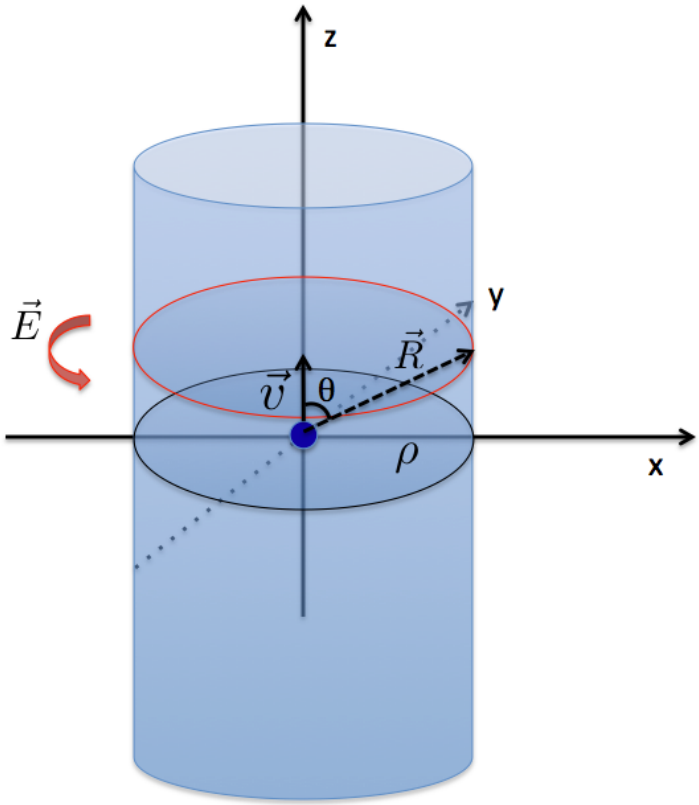

Figure 1.7: Illustration of simple model used to calculate the magnetic monopole's energy loss in conductor.

and K. Kinoshita [25]. Assume a magnetic monopole is traveling along the z axis with constant velocity $\vec{v}$ inside an infinite conducting medium with conductivity σ, as illustrated in Fig. 1.7. Consider the electric field the magnetic monopole generates at the moment when the magnetic monopole is passing through the origin. With the analogy to the Biot-Savart law, we obtain the electric field at the wire at radius ρ:

$$E(\theta, \rho) = \frac{gv\rho}{c\rho^3/\sin^3\theta} = \frac{g\beta\sin^2\theta}{\rho^2}\,. \tag{1.33}$$

The energy dissipated in the wire is then obtained by applying Ohm's Law:

$$d\epsilon = \sigma E^2 2\pi\rho\; d\rho\; dz\; dt = \frac{1}{v}\sigma E^2 2\pi\rho\; d\rho\; dz\; dz\,. \tag{1.34}$$

Integrating over all space, we get the total energy dissipation per unit length:

$$\frac{dE}{dx} = \iiint_V \frac{d\epsilon}{dz} dV = \int_0^{\pi} d\theta \int_{\Lambda}^{\infty} \frac{2\pi\sigma E(\theta,\rho)^2\rho^2}{v\sin^2\theta} d\rho = \frac{\pi^2\sigma}{\Lambda c} g^2\beta\,. \tag{1.35}$$

The parameter Λ in Eq. 1.35 is just a lower cut-off distance needed to avoid a singularity. However it has its own physical meaning as one of the parameters characterizing the properties of the material.

Thus we obtain the form given in Eq. 1.32 via a very simple but intuitive model. The Ahlen and Kinoshita result [25] rigorously derived from generalized Maxwell's Equations is:

$$-\frac{dE}{dx} = \frac{2\pi N_e g^2 e^2 \beta}{m_e c v_F}\left[ln\left(\frac{2m_e v_F \Lambda}{\hbar}\right) - \frac{1}{2}\right], \tag{1.36}$$

where the Fermi velocity $v_F = \frac{\hbar}{m_e}(3\pi^2 N_e)^{\frac{1}{3}}$. For conductors, Λ is the mean free path between the magnetic monopole and electrons; for nonconductors, Λ equals r_0 (Bohr radius). This result is only valid for monopoles in the speed region of $10^{-4} < \beta < 0.01$.

1.5.4 Summary of Monopole Energy Loss Calculations

We have briefly discussed the monopole energy loss in two different cases: ionization dominates when the monopole is fast, atomic excitation dominates when the monopole is sufficiently slow. In both regions, the energy loss is well described, as shown in Fig. 1.8. However, in the intermediate velocity region $\beta \sim 10^{-2} - 10^{-1}$, the situation becomes complicated and neither ionization nor atomic excitation is negligible. In that region what is typically done is to perform a polynomial interpolation of Eq. 1.31 and Eq. 1.36 between the two separated well understood velocity regions, which is implemented in our simulation (to be discussed in detail in Chapter 3).

Heavy ionization is one of the most distinguishable features for the monopole signals we are relying on to carry out this analysis, so estimating the uncertainty of this energy loss is crucial. For monopoles with $\beta \geq 0.1$, the uncertainty in the dE/dx formula (Eq. 1.31) is estimated to be 3% [21]. For slower monopoles with $\beta < 0.01$, no solid estimation of the uncertainty exists in the theoretical literature. Hence we adopt an estimate of 100% upper error and 40% lower uncertainty, based on an estimate made by Groom [29] for the energy loss in silicon shown in Fig. 1.8.

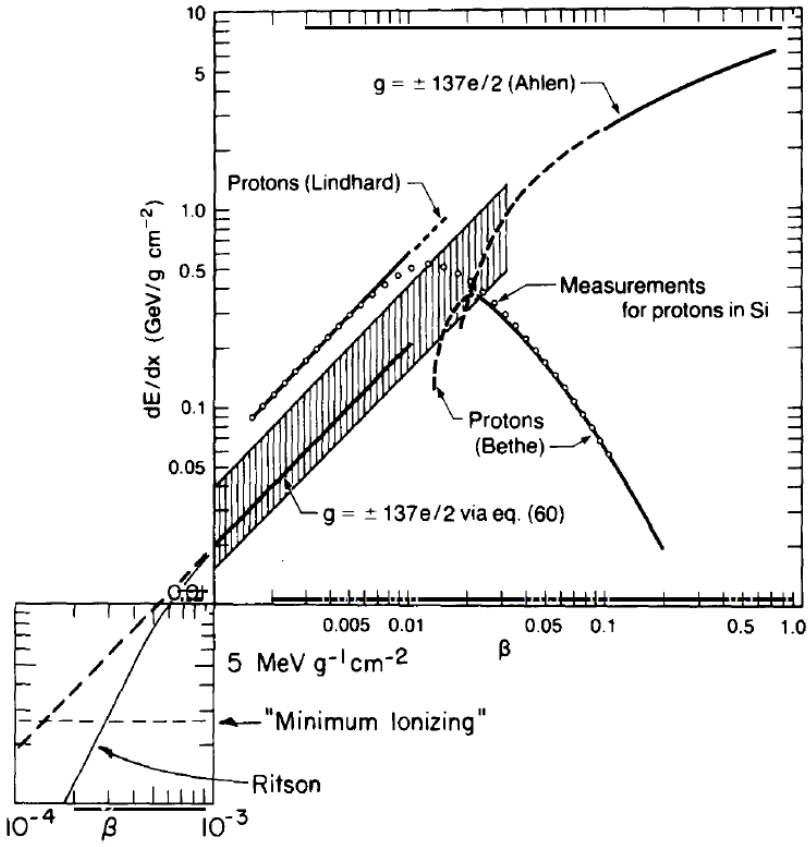

Figure 1.8: Energy loss for monopoles with g =±137e/2 in silicon as a function of the velocity of the magnetic monopole, which is adapted from Groom's review paper [29].

1.6 Acceptance of Magnetic Monopoles In Surface Detectors

In this section we calculate the acceptance for monopoles of a surface detector, like the NOνA far detector, with a qualitative method in estimating the energy loss of monopoles through the atmosphere and Earth.

We adopt a simplified geometry model for Earth and its atmosphere as illustrated in Fig. 1.9. The acceptance depends on whether monopoles have sufficient energy to reach the detector after penetrating air and the earth. Denote L the path length in the earth and ΔL as the path length in the atmosphere that a magnetic monopole has to go through to reach the NOνA far detector. Applying Eq. 1.36, we can obtain a rough estimation of the energy loss $(\delta E_{earth}(L) + \delta E_{air}(\Delta L))$ of a magnetic monopole of a given velocity. The kinetic energy E_p of the magnetic monopole must be greater than the total energy loss for it to reach the NOνA far detector.

With the approximation that the monopole velocity remains constant (so we have a constant energy loss) throughout its path to the far detector, we can derive the effective acceptance solid angle (Ω) of magnetic monopoles with a certain mass and velocity.

The minimum path a monopole can take through the atmosphere is ΔR when it is vertically incident. If $E_p \leqslant \frac{dE}{dx}_{air} \Delta R$, the monopole cannot penetrate the atmosphere to reach the detector. The longest path the monopole can have through the atmosphere without penetrating the earth is $\Delta L = \sqrt{(R+\Delta R)^2 - R^2}$ when it is horizontal. If $E_p \leqslant \frac{dE}{dx}_{air} \sqrt{(R+\Delta R)^2 - R^2}$, the magnetic monopole cannot come up from below ($L = 0$ and $\theta < \frac{\pi}{2}$).

$$\Omega = \mathrm{Max}\left(0, 2\pi \frac{E_p^2 + 2RE_p \frac{dE}{dx}_{air} - (2R+\Delta R)\Delta R \frac{dE}{dx}_{air}^2}{2RE_p \frac{dE}{dx}_{air}}\right). \tag{1.37}$$

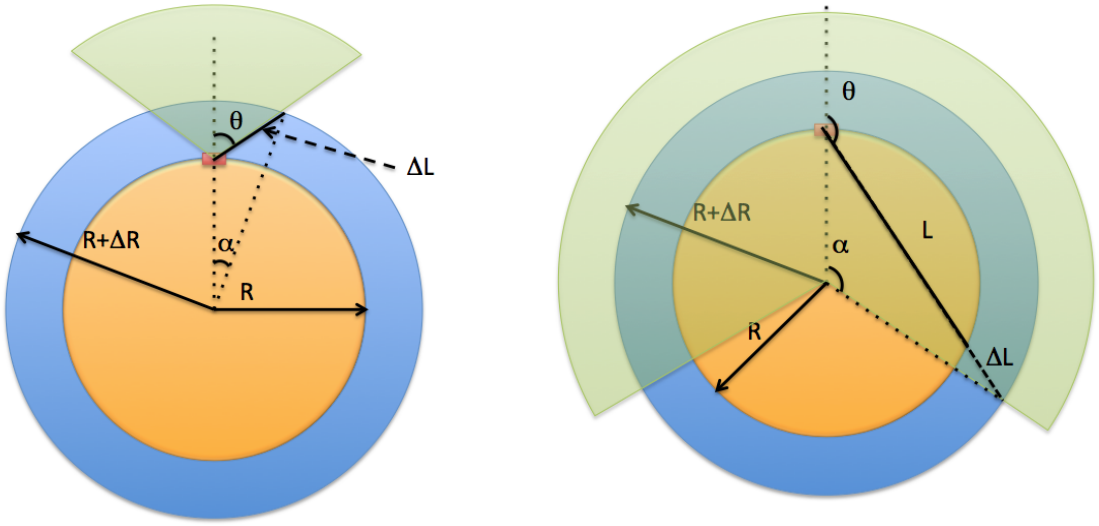

(a) (b)

Figure 1.9: Geometry used to determine the effective acceptance solid angle, which is shown as the light green area. (a) $\theta \leqslant \frac{\pi}{2}$: atmosphere magnetic monopoles that do not penetrate the earth; (b) $\theta > \frac{\pi}{2}$: Earth-penetrating monopoles. The NOνA far detector is shown in red, the atmosphere is blue, and the earth is yellow. R is the radius of Earth and ΔR is the effective thickness of the atmosphere. L is the path length through the earth and ΔL is the path length through the atmosphere.

Otherwise, the monopole has sufficient kinetic energy to make it through part of Earth, like the case shown in Fig. 1.9 (b). We obtain the largest possible acceptance solid angle $\Omega = 2\pi(1 - \cos\theta_{max})$, when

$$\cos\theta_{max} = -\frac{(L+\Delta L)^2 + R^2 - (R+\Delta R)^2}{2R(L+\Delta L)}\,. \tag{1.38}$$

If $E_p \geqslant \frac{dE}{dx}_{air}\Delta R + 2\frac{dE}{dx}_{earth}R$, the monopole has enough energy to reach the detector from any direction. In this case $\theta_{max} = \pi$ and we have a total acceptance solid angle of 4π.

The acceptance angle shown in Fig.1.10 is calculated for monopoles that only carry a unit Dirac magnetic charge. With this assumption, a GUT magnetic monopole with mass of 10^{16} GeV and $\beta = 10^{-3}$ will completely penetrate Earth. For monopoles with

more magnetic charge or additional electronic charge, more kinetic energy is needed for them to penetrate through the atmosphere and the earth due to the increased energy loss.

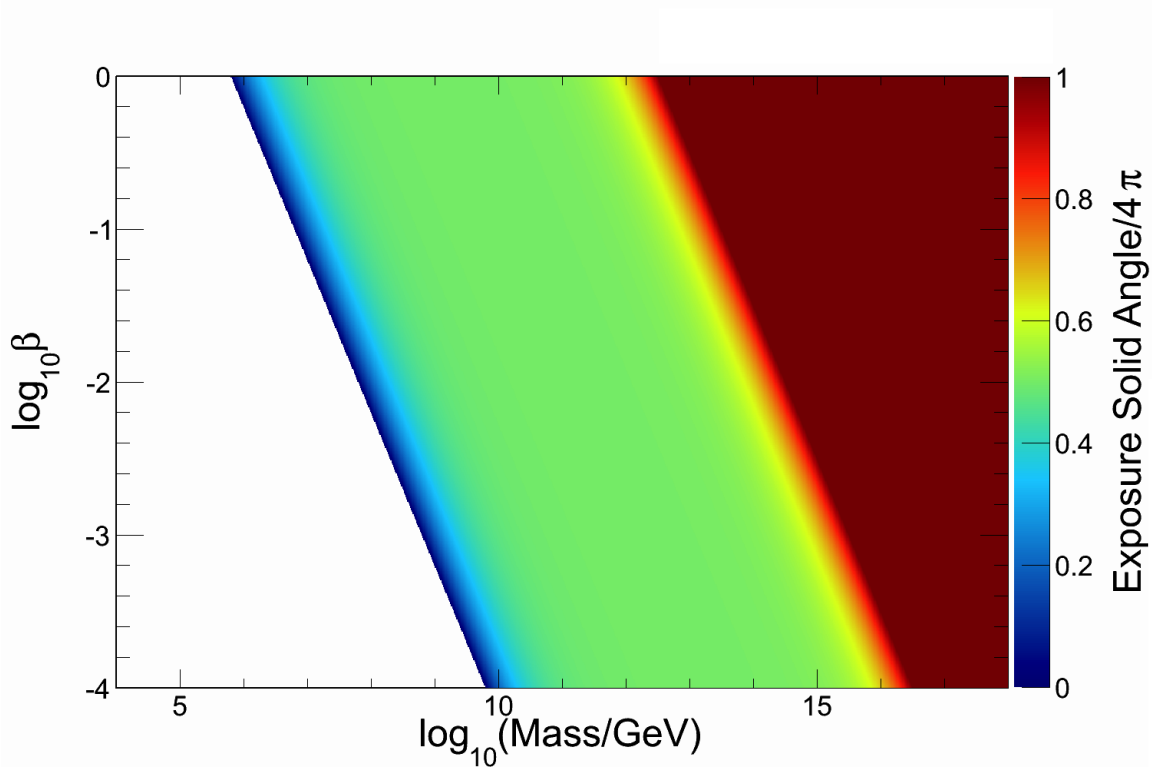

Figure 1.10: The magnetic monopole solid angle acceptance of the NOνA far detector as a function of monopole mass and velocity. We have assumed monopoles of a single Dirac charge (g_D) and no additional electronic charge.

1.7 Present Limits on Magnetic Monopoles Searches

To date there is no experimental evidence for magnetic monopoles, only limits on their flux as a function of mass and velocity. Present limits are shown in Fig. 1.11.

The IceCube [30] collaboration is searching for extra-galactic neutrinos with a large detector under the ice surface at the South Pole. Taking advantage of its enormous effective detector surface area, they have the most sensitive upper flux limit: 3.0×10^{-18} cm^{-2}s^{-1}sr^{-1} with 90% CL, for relativistic monopoles with $\beta \gtrsim 0.8$.

For searches below $\beta = 0.8$, Fig. 1.11 shows a rough sketch of the best (lowest) upper flux limits at the 90% CL set by different experiments searching for cosmic magnetic monopoles without the assumption that monopoles may catalyze proton decay.[3]

Table 1.2: Limits on the cosmic magnetic monopole flux from the MACRO experiment. The limits depend on the magnetic monopole mass and on its velocity [31].

Flux ($cm^{-2}s^{-1}sr^{-1}$)	Mass (GeV/c^2)	Velocity (β)
$\leq 1.4 \times 10^{-16}$	$\gtrsim 10^{10}$	$> 10^{-1}$
$\leq 1.4 \times 10^{-16}$	$\gtrsim 10^{16}$	$> 10^{-4}$
$\leq 2.8 \times 10^{-16}$	$\gtrsim 10^{6}$	$> 10^{-1}$
$\leq 2.8 \times 10^{-16}$	$\gtrsim 10^{10}$	$> 10^{-4}$

MACRO [31] has the best limits for super heavy GUT monopoles, shown in Table 1.2, and their sensitivity covers most of the phase space in Fig. 1.11. However, due to the underground location of the MACRO detector, they are not sensitive to lower-energy monopoles, which are blocked by the earth. The SLIM detector [32], built at a high altitude (5230 m a.s.l), covers a blind region for low mass monopoles which do not have enough energy to penetrate the entire atmosphere.

There remains a "virgin land" in the phase space map, which NOνA is uniquely sensitive to, as shown in the blue region of Fig. 1.11.

[3]The energy loss is adopting the simplified model described in the previous section.

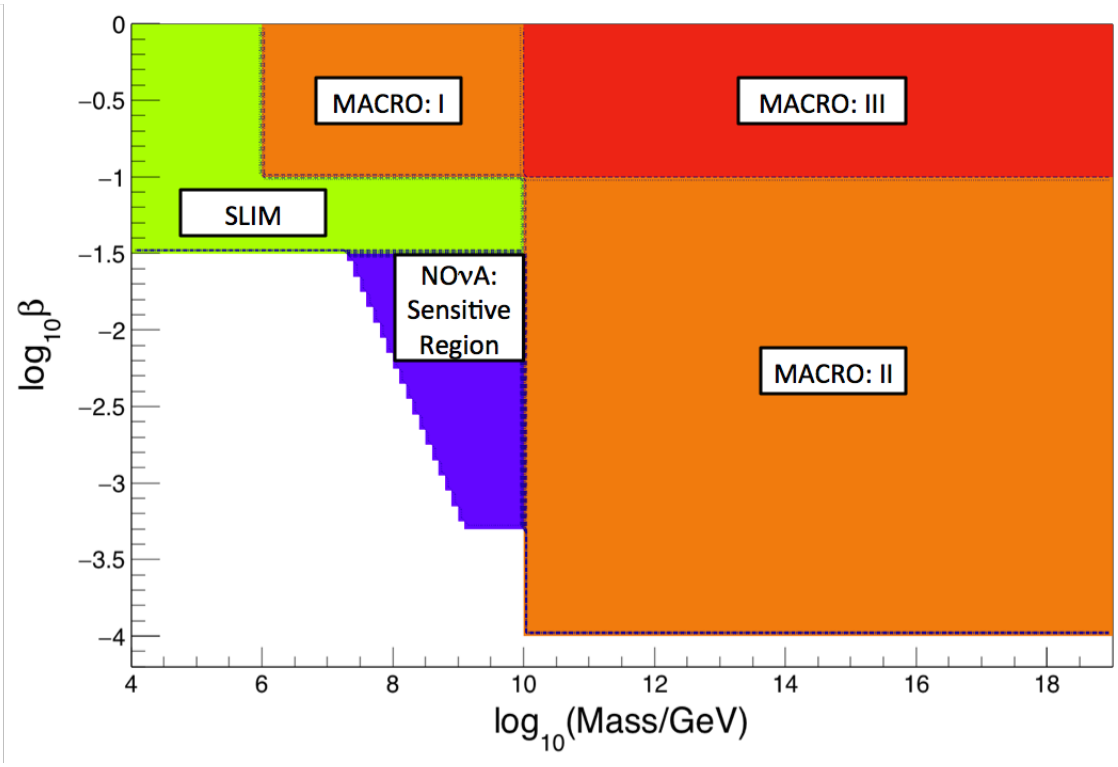

Figure 1.11: The upper flux limits at 90% CL of searches for non-relativistic ($\beta < 0.8$) monopoles as a function of monopole mass and velocity, set by MACRO (I and II: 2.8×10^{-16} cm^{-2}s^{-1}sr^{-1}; III: 1.4×10^{-16} cm^{-2}s^{-1}sr^{-1}) and SLIM (1.3×10^{-15} cm^{-2}s^{-1}sr^{-1}). The limits are calculated for monopoles with a single Dirac magnetic charge and no additional electric charge, without the assumption of catalyzing proton decay. The region which has not been covered by previous experiments, and which NOνA has no sensitivity is blank.

Chapter 2

The NOνA Far Detector at Ash River

NOνA is a currently active long-baseline neutrino oscillation experiment using the recently upgraded NuMI beam at Fermilab to measure $\nu_\mu \to \nu_e$ and $\overline{\nu}_\mu \to \overline{\nu}_e$ oscillations [33]. A 300 ton near detector is at Fermilab where the NuMI neutrino beam is produced, and a 14 kiloton far detector is located 810 kilometers away in Ash River, MN to observe the oscillated beam. The detectors are highly active and finely grained tracking calorimeters consisting of planes of extruded plastic (PVC) cells filled with scintillator-doped mineral oil. The far detector, due to its surface location, size, and excellent granularity, has been chosen for the search of cosmic magnetic monopoles. Thus for the remainder of this thesis, we focus on the far detector.

2.1 Detector Design

The NOνA far detector consists of 896 planes of extruded highly reflective polyvinyl chloride cells, alternating between horizontal and vertical orientations to provide three-dimensional tracking. A loop of wavelength-shifting fiber runs the length of each cell, with both ends of the fiber terminating at one pixel of a 32-pixel avalanche

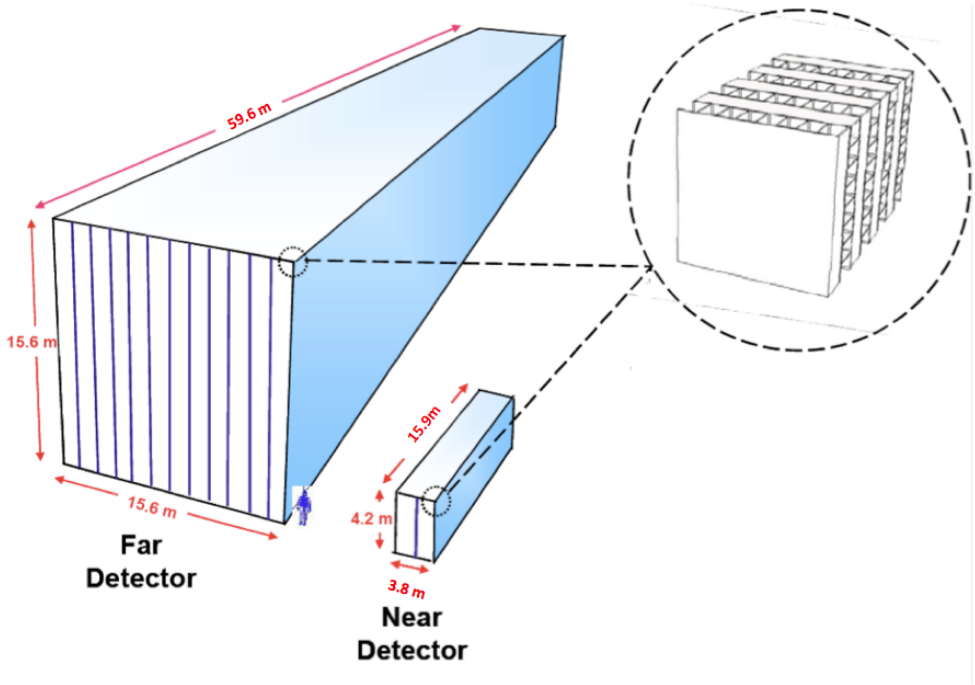

Figure 2.1: The two NOνA detectors. The inset figure shows that each detector has an identical alternating plane structure composed of vertical and horizontal cells.

photon-diode (APD) array, which is amplified and read out by a front-end board (FEB). Sixty four FEBs (2048 cells) feed into a data concentrator module (DCM) which groups the data into time-ordered packets to be sent to a computer buffer farm for further processing and triggering. Power to the APDs, FEBs, and DCMs is provided by the University of Virginia designed and fabricated power distribution system.

Each plane of the NOνA far detector has 384 cells, giving a total number of 344,064 cells. The detector coordinate system is the following: the positive X axis points roughly west and is parallel to the horizontal cells, the positive Y axis points up and is aligned with the vertical cells, the positive Z axis points roughly north and is normal to the PVC planes. The origin of the coordinate system is centered on the upstream face of the first (most southerly) plane. The geometry parameters of the

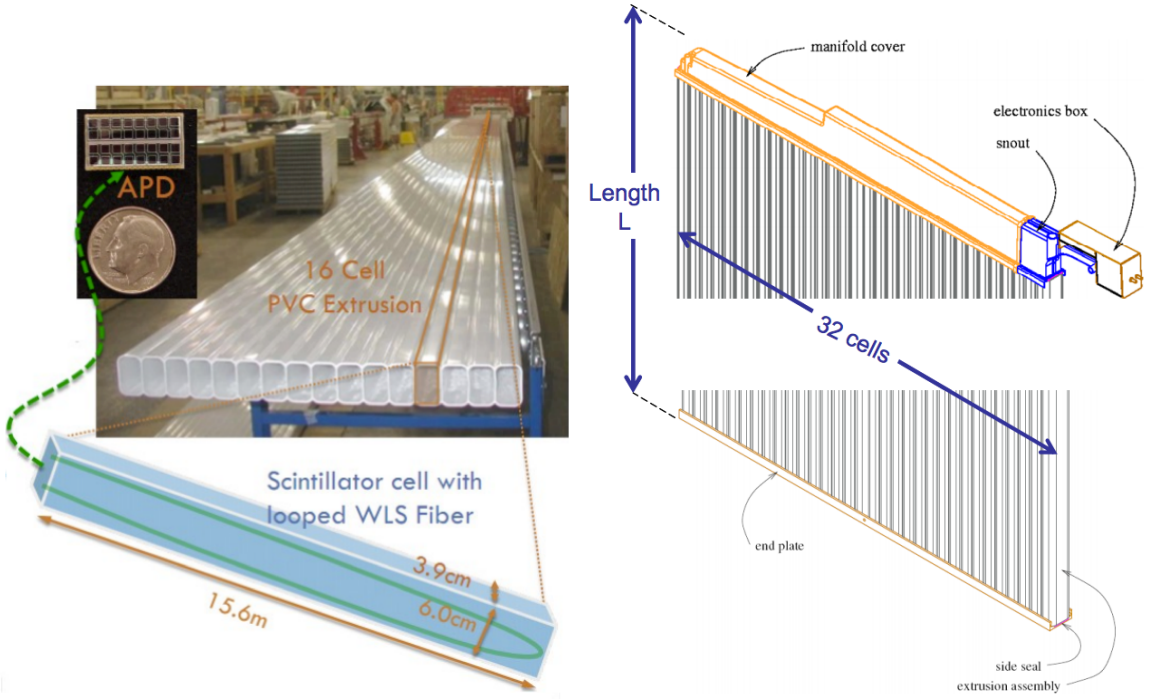

(a) (b)

Figure 2.2: A NOνA extrusion module constructed from two side-by-side 16-cell PVC extrusions and capped at both ends to contain the liquid scintillator. The manifold end routes the 64 fiber ends to a cookie which couples to the avalanche photodiode array and associated electronics. The length L with the end plate and manifold is 15.7 meters for all the modules at the far detector [33].

Table 2.1: The summary of the far detector geometry.

Quantity	Value
Number of Planes	896
Cells per Plane	384
Cell Depth	5.64 cm
Cell Width	3.60 cm
Size (X)	[-758, 765] cm
Size (Y)	[-749, 765] cm
Size (Z)	[0, 5962] cm

far detector are summarized in Table 2.1.

Assuming an isotropic flux of magnetic monopoles, a larger surface area leads to a larger acceptance. As illustrated in Table 2.2, the NOνA far detector has the largest surface area among all the previous monopole search experiments, except IceCube.

Table 2.2: The surface area of the NOνA far detector, MACRO detector, SLIM detector and OHYA detector.

Experiment	NOνA	MACRO [31]	SLIM [32]	OHYA [34]
Surface Area (m^2)	4082	3482	427	2000

2.2 Photodetector

When a particle deposits energy in the scintillating oil (whose components are listed in Table 2.3), light is created. Some of this light gets into the 0.7-mm diameter optical fiber from where it is absorbed and re-emitted, and then part is captured via total internal reflection and transported to an avalanche photo-diode (APD) [33]. The APD has 32 pixels, each 2×1 mm^2, in order to read out both ends of a cell's fiber. The APD quantum efficiency is about 80% for the spectrum of light delivered by the fiber. It converts the light into an electric signal and amplifies it by roughly a factor of 100. This signal is proportional to the energy deposited until saturation. The NOνA APDs typically operate between 350V - 450V with a standing current of approximately 1 nA per 32-channel APD array. They are cooled to -15 C to reduce their noise.

2.3 Front End Electronics

A front-end board was developed that: (1) amplifies and shapes the signals from the APDs; (2) digitizes the signals; (3) zero-suppresses the data; (4) formats and time stamps the data and sends it to a DCM; and (5) hosts the circuits that cools

Table 2.3: The composition of the NOνA liquid scintillator [36].

Component	Purpose	Mass Fraction
mineral oil ($CH_{2.02}$)	solvent	94.63%
pseudo-cumene (C_9H_{12})	scintillant	5.23%
PPO ($C_{15}H_{11}NO$)	wavelength shifter	0.14%
bis-MSB	wavelength shifter	0.0016%
Stadis-425	antistatic dopant	0.001%
Vitamin E	antioxidant	0.001%

the APD. A custom low-noise ASIC was developed for NOνA to amplify the small signals from the extremely long fibers in the far detector [33]. A schematic of the ASIC is shown in Fig. 2.3. Signals from individual APD pixels are processed through individual amplifier and pulse-shaping stages before being multiplexed to a 12-bit ADC in sets of 8 channels. The 8:1 multiplexing of the APD channels results in each APD channel being sampled every 500 ns.

The front-end electronics board (FEB) is connected to an APD carrier board through a short ribbon cable. In addition to the ASIC and ADC, the front-end board contains a connector for communication to the DCM, the thermoelectric cooler controller circuitry, DACs and ADCs for control and monitoring, and an FPGA for digital signal processing, I/O functions, and general board monitoring.

The amplified signal A is described by the function:

$$A = Norm \cdot exp[-(t - t_0)/F]\{1 - exp[-(t - t_0)/R)]\} + B\,, \tag{2.1}$$

where the rise time R is 382 ns, the fall time F is 7000 ns, t_0 is the cell hit time (residual time), B is the noise baseline of the channel, and $Norm$ is an overall normalization constant proportional to the energy deposition of the cell hit and related to the position of the hit in the cell.

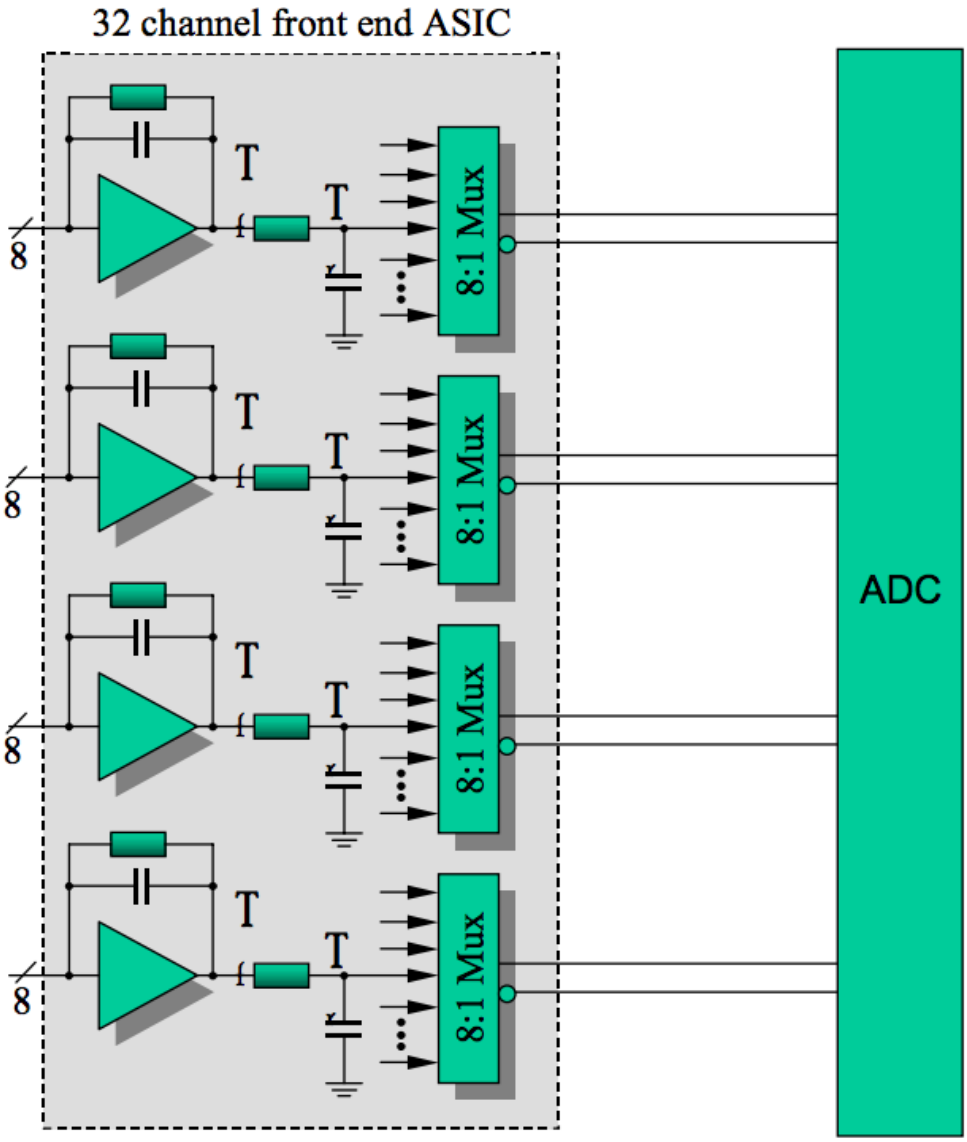

Figure 2.3: Schematic of the ASIC and ADC used in the FEB [33].

Equation 2.1 is valid for all fast charged particles whose energy deposit occurs in a time less than the rise time of the amplifier. For slowly moving exotic particles, this equation has to be modified, as will be discussed in detail in the next chapter. As shown in Fig. 2.4, the amplifier response can be used to get finer timing resolution, than by simply using the 500 ns ADC sampling time interval. This is done by performing a fit to the ADC samples: to determine the pulse-height N, the baseline B and the residual time t_0. Given the three degrees of freedom, at least 4 sample points are needed to perform the fit. More samples are preferred, but DAQ bandwidth and storage limitations preclude reading out any more samples. The four samples are chosen to be one baseline sample and three following samples on the ASIC curve, as illustrated in Fig. 2.5.

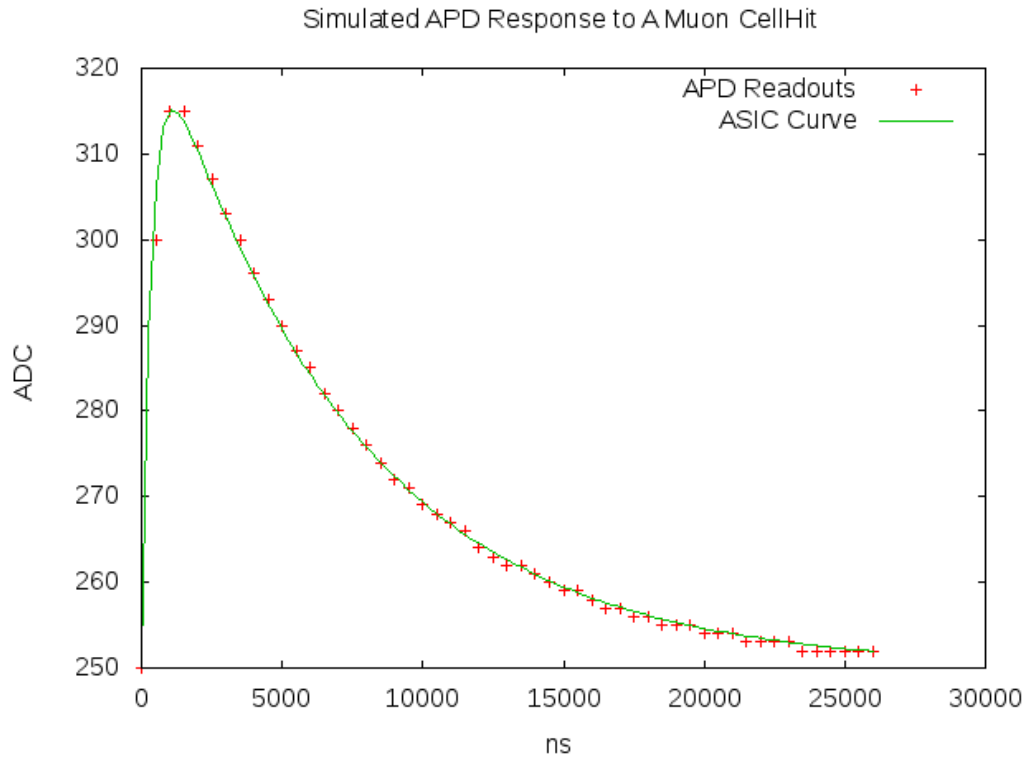

Figure 2.4: A simulation (with noise turned off) of the FEB response from a cell hit caused by a muon. Zero-suppression has been disabled. The red crosses correspond to each ADC sample every 500 ns and the green line is the best fit response curve given by Eq. 2.1.

As mentioned above, the pulse-height is proportional to the energy deposit in the cell, as well as the actual position of the hit due to the light attenuation in the fiber. The final calibrated time of the cell hit is corrected by the time of flight of the photons in the fiber. Note that the longitudinal position of a hit cannot be determined from the cell itself, but requires additional hits from the other view. Cell hits in X (vertical) planes only provide the information of X and Z coordinate information, and similarly for the Y (horizontal) planes. For the remainder of this thesis, the longitudinal (X) coordinates in Y planes or the Y coordinates in X planes are referred to as W positions. The W position is crucial for both time and energy calibration of a single cell hit, but can be only obtained from matched tracks in both the X and Y views.

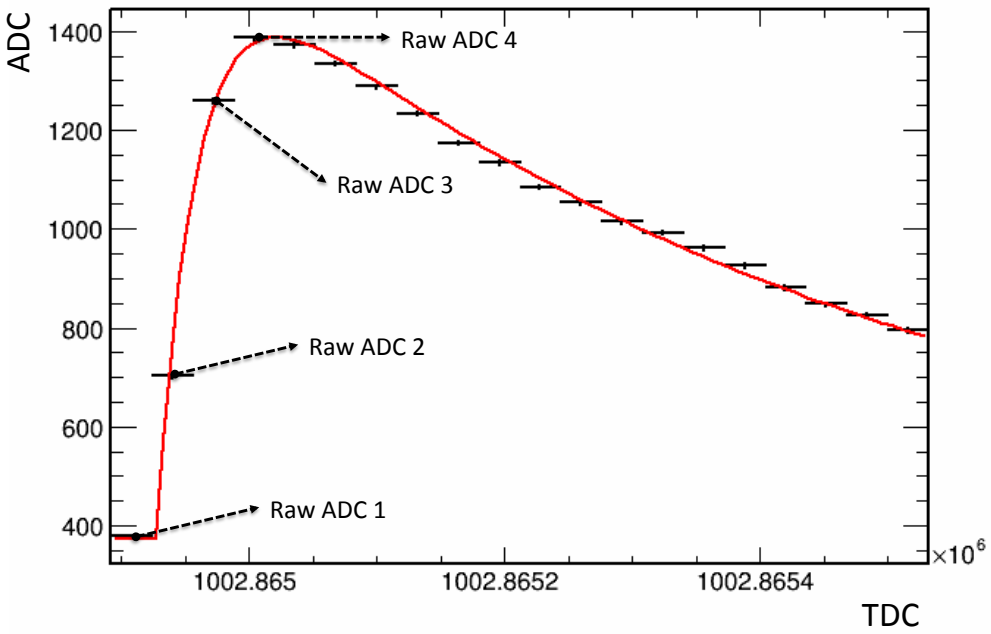

Figure 2.5: A typical digitized pulse taken with zero-suppression disabled. The four labeled points are what would be read out in DCS mode.

2.4 The Data Acquisition System

NOνA uses a novel data acquisition (DAQ) system based on a continuous dead-time-less readout of the front-end electronics, extended buffering of the data stream and asynchronous software triggering. The DAQ system, shown schematically in Fig. 2.6, is composed of four main components: a timing and command distribution system, an array of Data Concentrator Modules (DCM), a Gbit Ethernet network, and a buffer farm. Timing synchronization and command packets for the DCMs come from the timing and command system consisting of one Master Timer Unit and 28 Slave Timing Distribution Units (STDU) that act as a separate network backbone for these signals. Digitized data from up to 64 front-end boards are routed through CAT5 cables to a DCM. The DCMs send data to the buffer farm, so that each processor of the farm has access to a time slice of all of the channels in the far detector. This is done using commercial switches and a Gbit Ethernet network. The buffer farm and DCMs are under the control of a Run Control Computer [33].

The FEB collects nanoslices from its 32 channels and sends them on to the Data Concentrator Module (DCM). The DCM collects data from 64 FEBs and assembles their nanoslices into a collection called a mircroslice that has a duration of 50 μs. The DCM also expands the relative 32 bit time stamp of the nanoslices with an additional 24 bits stored in the microslice header to form a 56 bit absolute time stamp. With a 64 MHz clock, this allows us to encode 35 years worth of ticks (15.625 ns between two consecutive ticks) without rolling over. The DCM prepares the data for network transfer by assembling microslices into a millislice. A millislice contains 5 ms of data, about the optimal data size for network transfer. Gathering the information of every millislice, we then have a milliblock: the information of the entire detector in 5 ms. Each data-driven trigger (to be discussed in details in Chapter 4) decision is made based on analysis one milliblock of data.

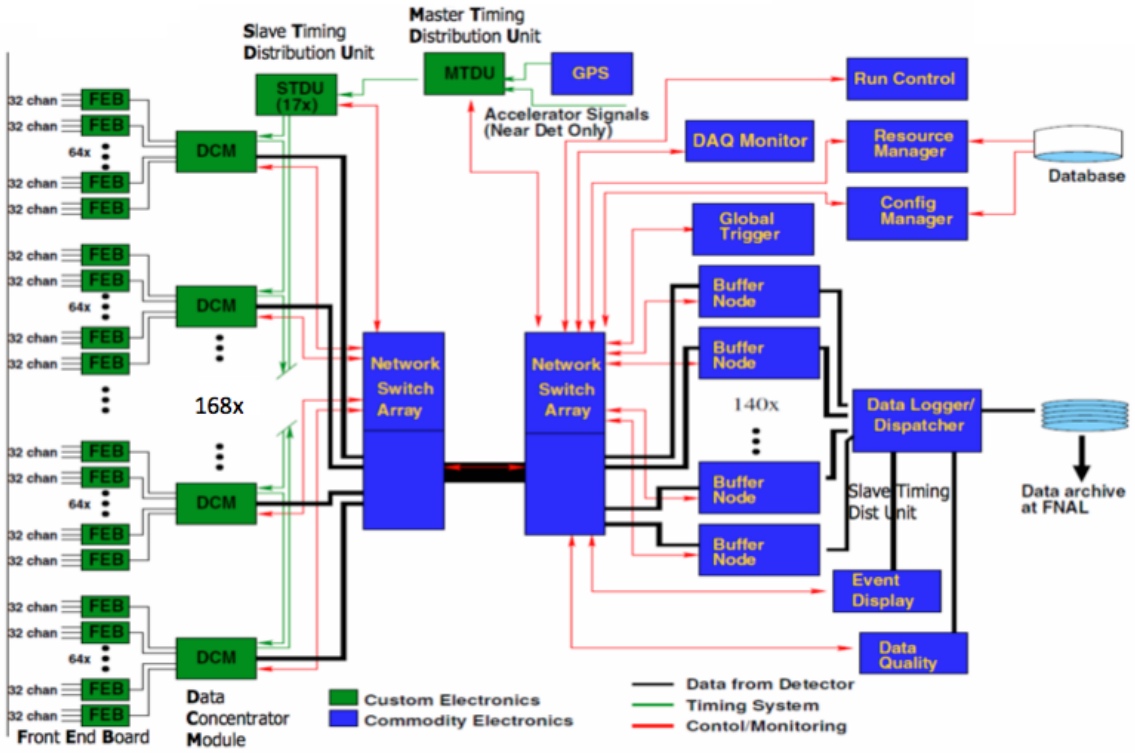

Figure 2.6: Topology of the NOνA data acquisition system.

2.4.1 Dual-Correlated-Sampling Triggering Algorithm

In the front-end board a so-called "dual-correlated-sampling" (DCS) algorithm is used to decide whether a hit has occurred in a particular cell, where by hit we mean a number of photoelectrons greater than a threshold, typically greater than about 1/5 MIP. Although the fundamental clock period of 1 tick is 15.625 ns, the multiplexing in the front-end board is such that each channel is sampled once every 32 ticks, or 500 ns. The ADC values and corresponding times (TDC) can be regarded as two long arrays of integers, which are denoted as ADC_i and TDC_i in the remainder of the thesis. The difference between ADC values that are 1500 ns apart ($DCS_i = ADC_{i+3} - ADC_i$), referred to as the dual-correlated-sampling value, is calculated. If DCS_i is above a threshold (which varies from 40-50 ADC for a typical channel), this channel's data are sent to the DCM. It is then disabled until the $DCS_{i+n} < 0.5 DCS_i$ after 32 ticks.

This sending of only that data greater than a threshold is called zero suppression.

The DCS threshold is determined by a DSO scan taken before a data-taking run starts. It varies from channel (pixel of APD) to channel. During the DSO scan we take 2,000 consecutive ADC samples, or effectively 1 ms of data for each channel (Fig. 2.7), that is, zero suppression is turned off. The RMS (σ, see Fig. 2.8) of the values of each channel is calculated, effectively measuring the noise of the APD and front-end electronics. The threshold is set to be 4σ greater than the noise mean of that corresponding channel. Channels with large noise values (large σ) are masked off.

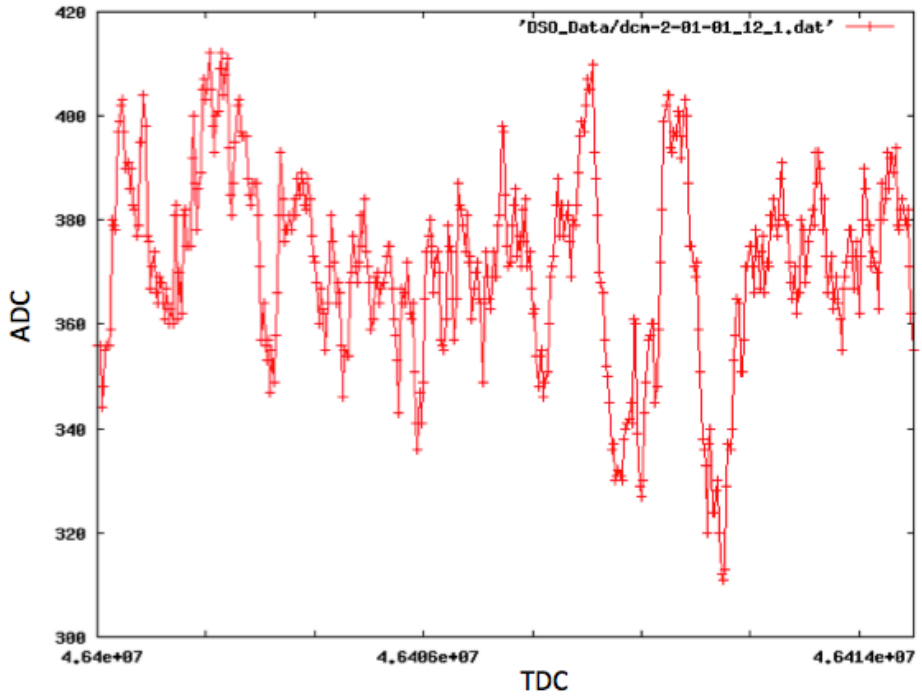

Figure 2.7: Typical noise spectrum from a DSO scan of a channel.

2.4.2 Nanoslice Format

The information of a hit: the time, ADC values and address of the cell, are recorded in a nanoslice. The nanoslice format (Fig. 2.9) consists of a header (cell id and status),

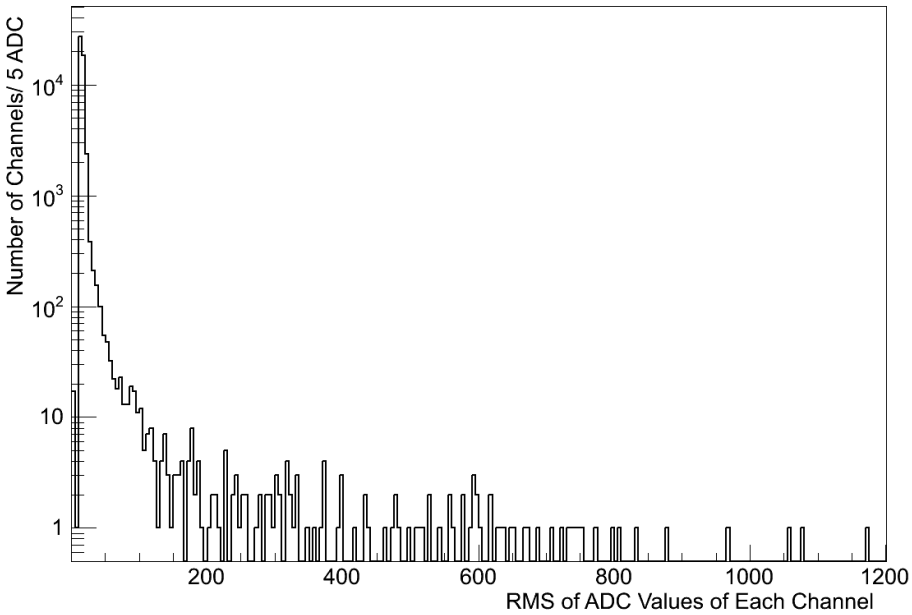

Figure 2.8: The distribution of the RMS noise values of the far detector channels obtained by a DSO scan.

time stamp and data payload. Note that the front-end board can output hits with effectively any number of ADC values. The number four NOνA has chosen is a compromise between event size and pulse shape reconstruction, as we will discuss in the following section.

The first word of a nanoslice is the nanoslice header, whose first three bits correspond to

$$\text{DM} = \text{Debug Mode} = \begin{cases} 1, & \text{Debug Mode} \\ 0, & \text{Normal.} \end{cases}$$

$$\text{DP} = \text{Data Present} = \begin{cases} 1, & \text{Hit Present} \\ 0, & \text{Empty Nanoslice.} \end{cases}$$

$$\text{LS} = \text{Link Status} = \begin{cases} 1, & \text{Link OK} \\ 0, & \text{Link ERROR.} \end{cases}$$

The remaining bits of the nanoslice header are described as follows.

- **DFT** - Data format type indicator. This field denotes a packet as either a data packet or status packet. For fixed length data packets this has the value 001.
- **FEB ID** - Front end board "Link" identifier for the DCM, range 0-63.
- **FEB Status** - Front end board status. This represents the readout mode that the current packet was generated under. This ranges from simple DCS to DSO mode.
- **Pixel Address** - APD Pixel address number, range 0-31.
- **Version** - Major version of the nanoslice format. For variable size nanoslices the word size of the nanoslice is stored in the parent microslice header.
- **SEQ** - FEB frame sequence number. Incremented by one on each frame from a given FEB.

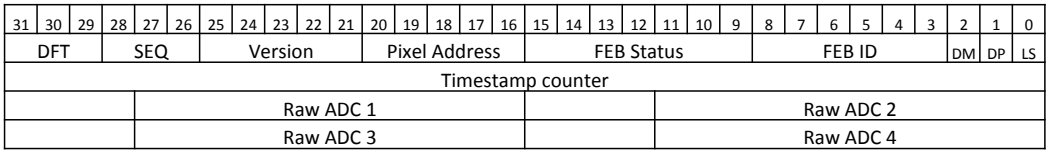

Figure 2.9: Nanoslice format with 4 ADC samples of the amplifier waveform.

A nanoslice contains all the information of a cell hit, which is the fundamental unit we reconstruct physics events based on.

2.4.3 The DAQ Data Formats

The NOνA experiment has a raw data format that is a hierarchical concatenation of different data blocks that arise at each level of the data acquisition chain. The general ordering of the data formats is in terms of the data unit at each level of processing, with higher level formats including the smaller units in a packed form with appropriate headers. The ordering is specified as [35]:

- **Run** – A run is a sequential collection of triggered events written out to permanent storage that corresponds to a distinct period of time, normally on the order of hours. It includes the required detector and trigger information that is sufficient to describe the detector and run time parameters of the DAQ system. Not all configuration information is embedded in the run file, but instead some segments of this information are written to a master database.

- **SubRun** – A new subrun begins when the largest data stream reaches the size limit (currently set at 1 GB) in a given period of time (currently set as 1 hour). If no data stream reaches the size limit during the period of time, a new subrun will start automatically. When 64 subruns are accumulated during one run, a new run will automatically start.

- **Event** – An event is a piece of data recording the activity of the detector within a certain time window. The size of time window varies depends on the trigger which records this event. A fully qualified event includes all of the triggering information, timing information and data blocks corresponding to the trigger window of interest.

- **Trigger** – This information includes the type of trigger, the source of the trigger, the time at which the trigger was issued and the time window of interest that the trigger corresponds to. This information is used by the global trigger system and buffer nodes to initiate data retrieval and storage at the data logger.

- **Nanoslice** – This is the data read out from a single FEB channel and includes pulse height and timing information. It is sometimes referred to as a "hit" later in the thesis. Only data above a given threshold is read out to the DCM.

- **Microslice** – This is a 50 μs collection of individual FEB nanoslices, with appropriate time stamps for synchronization. This format is used for the extraction of data from the DCM's FPGA data buffer. Triggered events are written to offline stages in integral multiples of microslices.

- **Millislice** – This is a collection of microslices that are packaged together to form a larger data block appropriate for network transmission. Formed in the DCMs, millislices of the same time window are collected together in a buffer node and operated on by the trigger algorithms. The size of the block corresponds to either an Ethernet protocol "jumbo frame" or a 5 ms maximum time interval. This format is primarily used for data transmission between the DCMs and buffer nodes.

- **MilliBlock** – This is a collection of millislices extracted from all the data concentrator modules (DCM) during a 5 ms synchronized time period, which contains the entire detector activity in the 5 ms time window. This format exists on the buffer nodes, inside of the data ring buffer.

- **Data Block** – This is a collection of millislices and microslices that is extracted from the buffer node's ring buffer upon receipt of a trigger. This format becomes the payload of the final event structure that is written to permanent storage.

2.5 Single Cell Hit Calibration

The method of least χ^2 fitting of the 4 samples of a hit to a known response function is used to extract the time of a cell hit. As previously mentioned, the major

purpose of multiple sampling is to get improved timing resolution. This improvement is demonstrated by comparing the input time from the MC truth time to the reconstructed hit time of a simulated cell hit.

We have simulated 10,000 2 GeV single muons starting at (0.25, 2.28, 200) cm,[1] and traveling along the Z axis, with a uniformly distributed time variation of 1 μs. The simulation result is shown in Fig. 2.10. Without fitting, the time resolution for a single cell hit is roughly σ=144 ns, with fitting it is improved to below around 40 ns. The offset from zero of the peak of the fitted time difference distribution is corrected using the photon transportation time in the fiber.

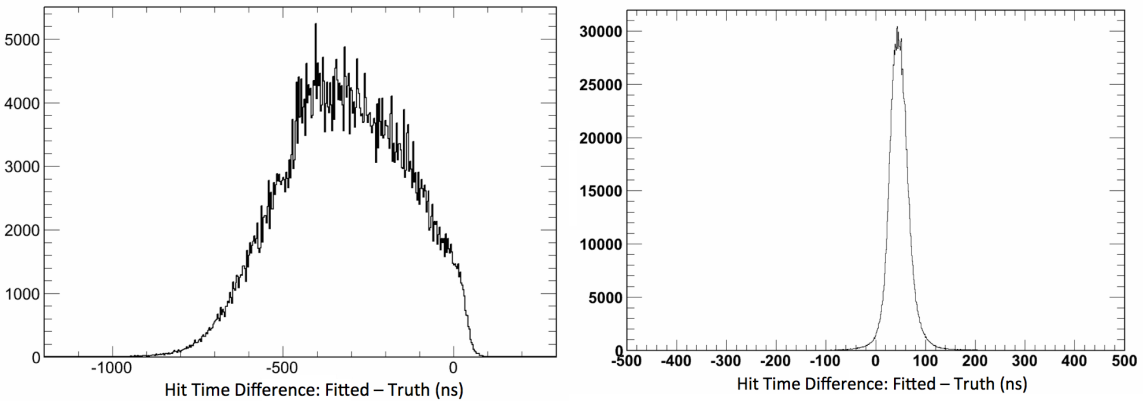

(a) (b)

Figure 2.10: Monte Carlo simulation of (a) the time difference of the input (true) time of the first hit and the raw time determined from the nanoslice time stamp counts, and (b) the same comparison but with a fit to the nanoslice pulse shape.

Fitting the APD waveform to multiple readout samples leads to a more precise pulse height and residual time simultaneously, as demonstrated by the plot in Fig. 2.11 (a). Generally speaking, a larger pulse height, with corresponding smaller relative statistical fluctuation, leads to more precise fitted values, which is demonstrated by

[1] All the muons start from the same position inside cell 192 of plane 30, which is near the geometical center of the far detector, with half of the full fibre length. So in this Monte Carlo test, every muon has an identical trajectory and the same attenuation factor.

the plot in Fig. 2.11 (b).

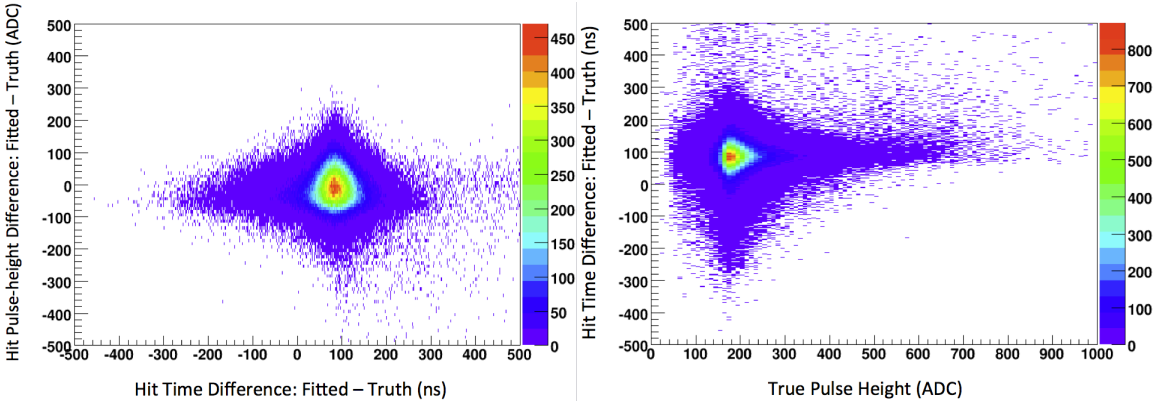

(a) (b)

Figure 2.11: Monte Carlo tests of the single hit calibration: (a) The difference between the fitted and true pulse heights vs. the difference between the fitted and true hit times; (b) The difference between the fitted and true hit times vs. the difference between the fitted and true pulse height (in ADC counts).

If the energy deposit in a cell is too high, the hit becomes "saturated", as shown in Fig. 2.12. A fast monopole would produce cell hits like this, which will be discussed in detail in the next chapter. To successfully fit to a saturated hit would require changing the nanoslice format by increasing the number of samples.[2] This leads to an increase in the event size, which the collaboration chose not to implement due to bandwidth limitations. Though we are not able to calibrate the exact energy deposit for a saturated hit, knowing the lower estimated energy deposit is enough to distinguish monopole signals from background in the NOνA far detector.

For non-saturated hits studies have been made to determine whether increasing the number of samples improves both the time and energy resolution. The improvement is not enough to compensate for increasing the size of data dramatically (see Fig. 2.13).

[2]Note that consecutive samples need not be taken.

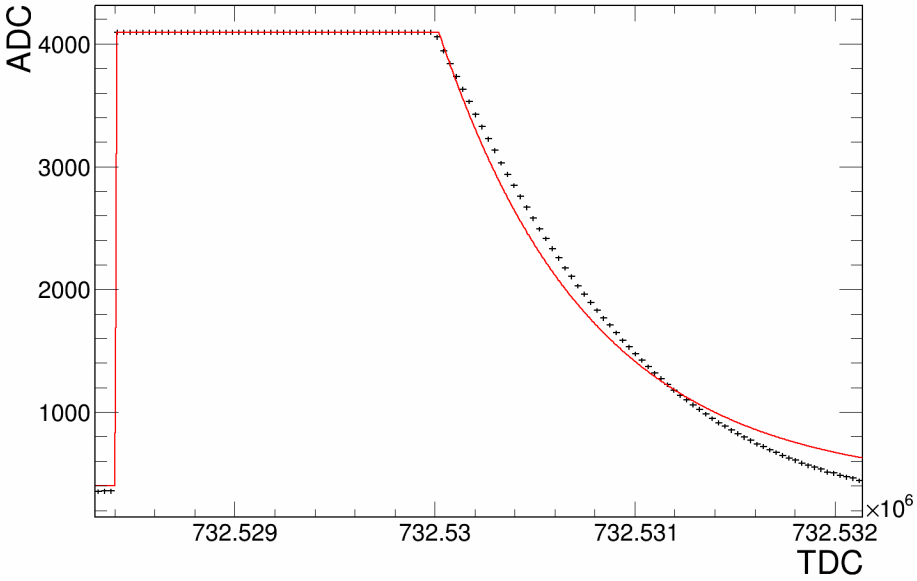

Figure 2.12: A saturated hit found in a DSO scan data in far detector. The fit is performed with 100 samples.

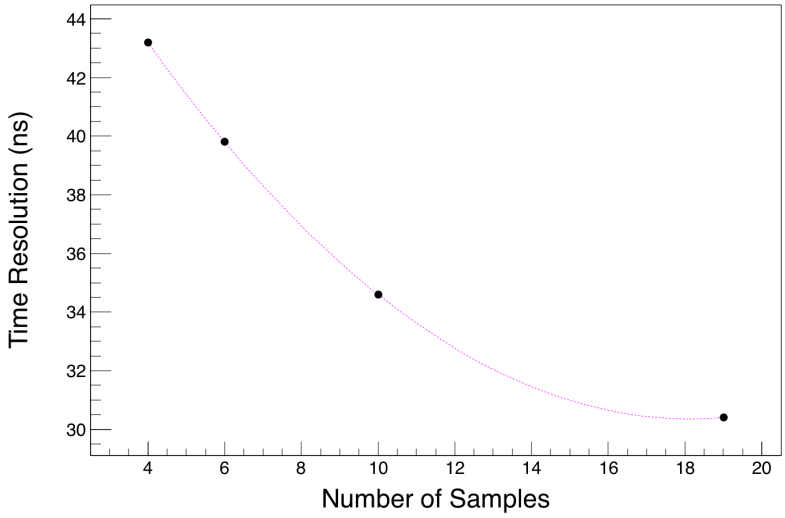

Figure 2.13: The time resolution of single hits of 2 GeV MC muons as a function of the number of samples.

The fitted pulse height, in ADC counts, is proportional to the number of photoelectrons (PE) collected by the readout end. The number of photoelectrons is corrected for fibre attenuation, from the energy deposit position in the cell to the readout end, which is referred to as the W position. The attenuation curve has the form:

$$f = Ae^{-W/L} + B\,, \tag{2.2}$$

where f is the fraction of photoelectrons produced by the APD after light has been transported in the fiber, L is the attenuation length, and the two coefficients (A, B) are fitted using the vast amount of cosmic-ray data for each cell, as shown in Fig. 2.14 (specifically for plane 895, cell 7 in the far detector). The number of photoelectrons is corrected using this fraction f, once the W position is provided by the reconstructed 3D track (which contains hits in both views), and the parameters provided for a specific cell in the database. The attenuation correction is crucial for energy calibration as an uncalibrated raw DCS value may represent a very different energy deposit. Figure 2.15 shows the distribution of the corrected photoelectron number at a given raw DCS value, based on 2 seconds of minimum bias far detector cosmic data. Using the corrected photoelectron number, we find the physics energy in units of MeV or MIP, as shown in Fig. 2.16.

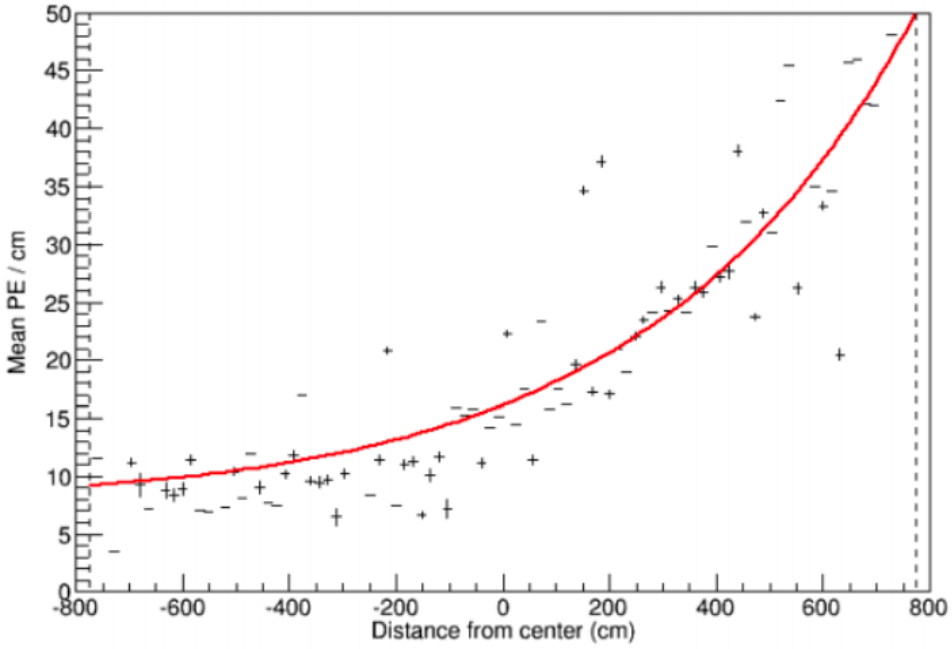

Figure 2.14: Far detector cosmic-ray data for plane 895 (vertical), cell 7. Every entry is given by a hit associated with a reconstructed cosmic-ray track. The fit curve gives the mean photoelectron number at a given W position.

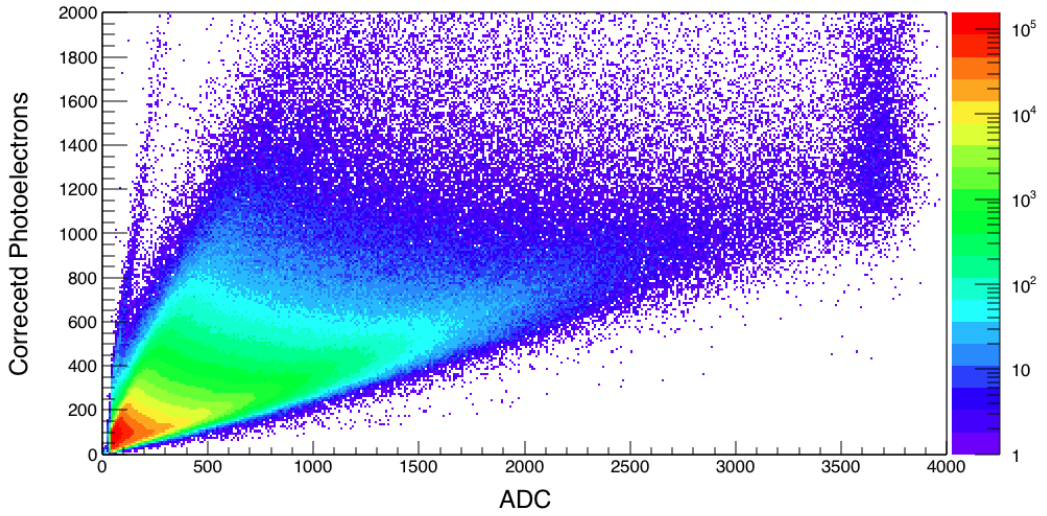

Figure 2.15: The distribution of corrected photoelectrons vs. the raw DCS value in ADC counts for all the far detector cells. Each entry corresponds to a hit associated with a reconstructed cosmic track.

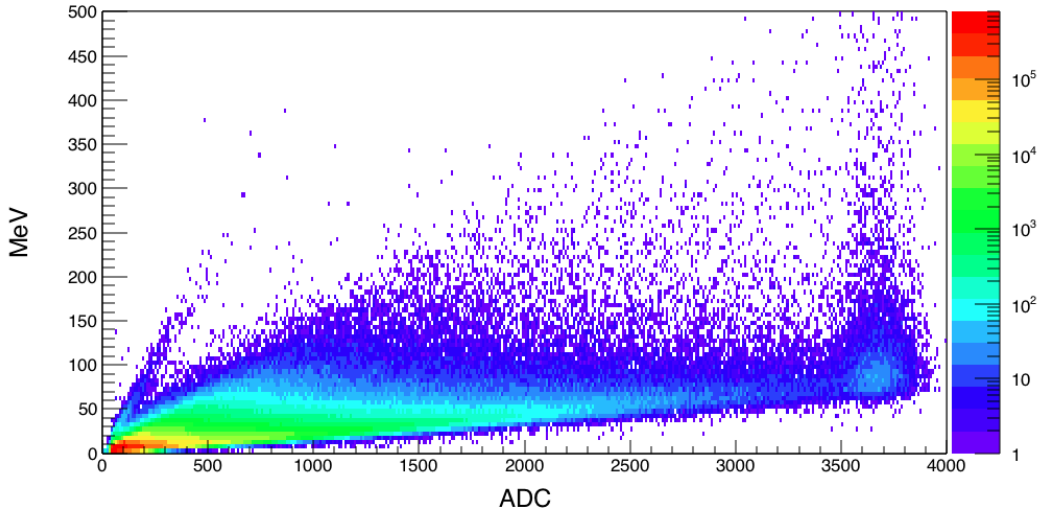

(a)

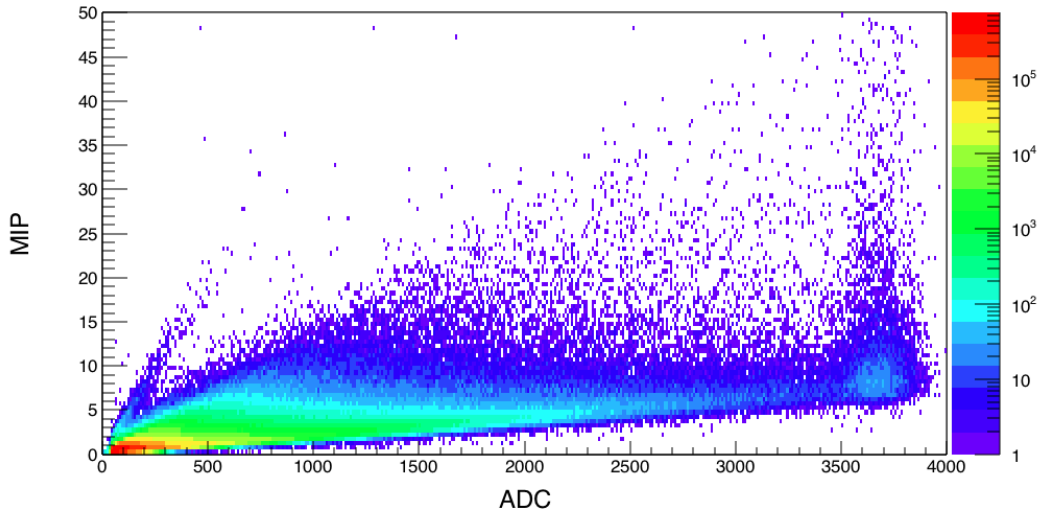

(b)

Figure 2.16: The calibrated energy deposit in a cell vs. DCS value in ADC, in the units of (a) MeV and (b) MIP.

Chapter 3

Simulation of Magnetic Monopoles

The NOνA software is implemented and maintained under the ART framework (Analysis & Reconstruction Toolkit) [37]. ART is a suite of tools, libraries, and applications for processing detector events, all written in C++. The "simulation engine" adopted by NOνA is Geant4, which simulates the propagation of all particles in the detector. The energies deposited by the simulated particles in active material are passed to a parameterized front-end simulation which converts energy deposits into scintillation light, transports the scintillation light to the APD, and simulates the read-out electronics response [38]. In this way, our simulated output is formatted like the raw data. A powerful tool, the event display (see Fig. 3.1) is used to visualize simulated as well as real data.

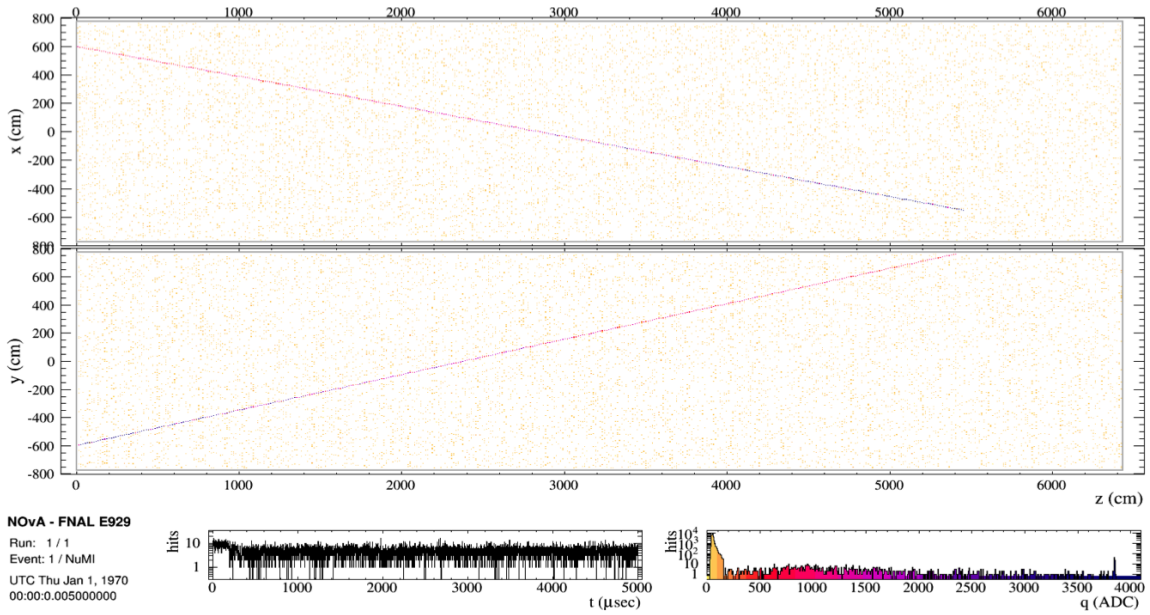

(a)

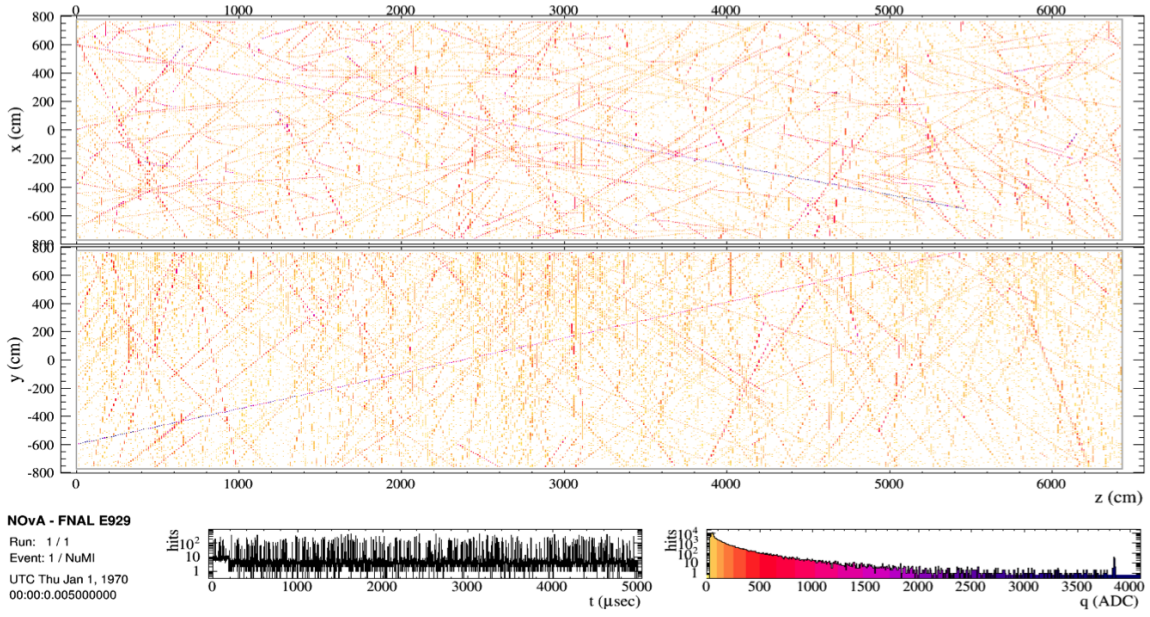

(b)

Figure 3.1: The event display shows the energy and time response of all the channels in both horizontal (y) and vertical (x) planes. Each hit is colored based on its DCS value in units of ADC counts, representing the uncalibrated energy deposit. (a) The event display of a simulated nonrelativistic ($\beta \sim 10^{-2}$) monopole's trajectory in both XZ and YZ views, with noise hits. (b) The same simulated monopole event overlaid with 5 ms of simulated cosmic-ray hits and noise hits.

3.1 Simulation of the Response of the Front-End Board

While the number of photons generated in the exact position of the energy deposit is proportional to the energy deposit, the number of photons surviving after transportation in the fiber is found using an attenuation curve determined from measurements from many spools of wavelength shifting fiber [38]. This is the number of photoelectrons (N_{pe}) captured by the APD.

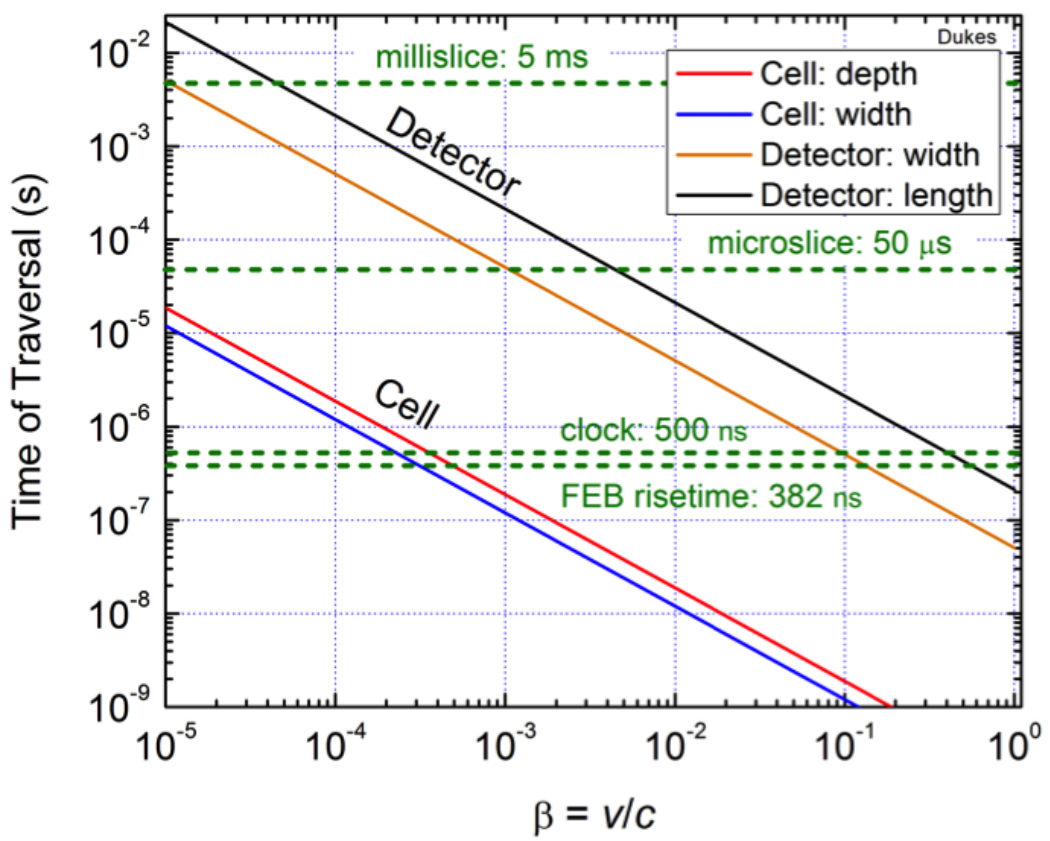

Figure 3.2: The times for monopoles to traverse a cell and the detector as a function of their velocities. The dimensions of cells and the detector are listed in Table 2.1.

We simulate the amplifier response of the front-end board in units of photoelectrons using the approximation of instantaneous energy deposit [38]:

$$f(t) = N_{pe}\frac{F}{F-R}\left(e^{-(t-t_0)/F} - e^{-(t-t_0)/R}\right) + B\,, \tag{3.1}$$

where t_0 is the time that the photoelectron pulse was collected by the APD, the pulse shape fall time $F = 7000$ ns, the rise time $R = 382$ ns, and B is the noise baseline which varies from channel to channel. This equation is identical to Eq. 2.1 we introduced in Chapter 2, by replacing $Norm$ by $N_{pe}\frac{F}{F-R}$.

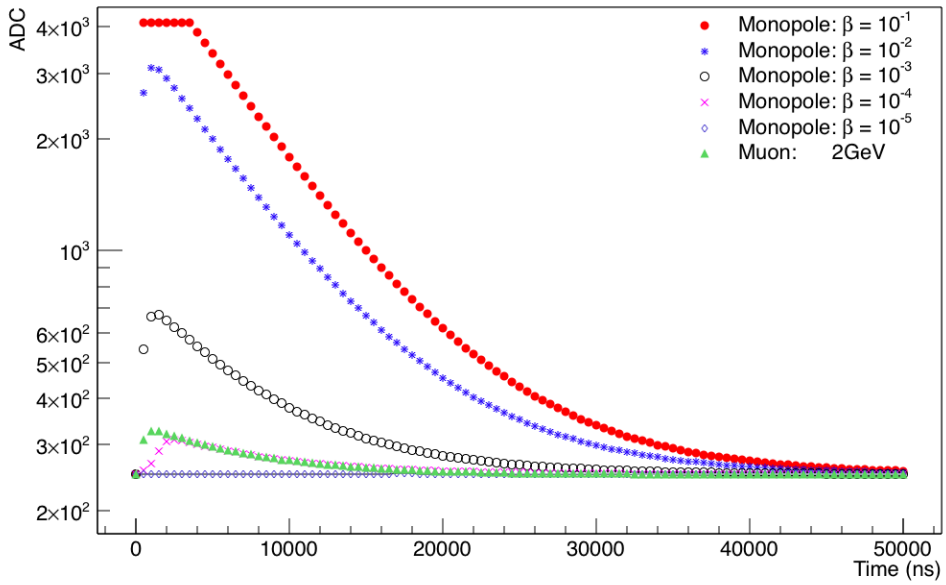

Figure 3.3: The simulated amplifier response for magnetic monopoles with different velocities passing through the same cell along the z axis (path length of 5.64 cm, the depth of each cell). The response of a 2 GeV muon with same trajectory has also been plotted for reference. The distances (W) between the trajectory and the corresponding APDs are half of the cell length.

For charged particles that are significantly slower than the speed of light, particularly slow magnetic monopoles, the pulse shape (ASIC curve) is very different. In particular, the rise time of the amplified pulse is longer, as it may take more than 382 ns for the monopole to traverse the detector, as shown in Fig. 3.2.

Fast ($\beta > 0.1$) magnetic monopoles can easily cause saturated hits, due to the limit of the maximum ADC output of 4095. Figure 3.3 shows the simulated amplifier response of a cell caused by magnetic monopoles with different velocities. The figure

was made by simulating magnetic monopoles passing through the same cell and along the same trajectory (magnetic monopoles that penetrate have sufficient momentum they are hardly deflected along their straight trajectories). And for monopoles with $\beta = 10^{-4}$, it takes 2 μs to traverse the depth of a cell.

To validate the simulation of the front-end board response, the following has been done. The front-end board response for a slow particle, whose time duration inside the cell is not negligible, is modeled as a superposition of the response of many fast particles hitting the same cell in a uniform and continuous time range (assuming the particle's speed does not change inside the cell). That is

$$ADC = N' \int_{t_i}^{t_f} e^{-(t-t_0)/F}\{1 - e^{-(t_0-t)/R)}\}\theta(t-t_0)dt_0 + B\,, \tag{3.2}$$

where the rise time $R = 382$ ns, the fall time $F = 7000$ ns, B is the noise baseline, $\theta(t-t_0)$ is a step function, t_i is the particle entering time and t_f is the time leaving the cell, N' is proportional to the energy loss rate (dE/dt).

By combining both the fast and slow cases, we obtain a universal front-end board response function:

$$ADC = \begin{cases} \mathrm{Min}(N'F(e^{\frac{t_f-t}{F}} - e^{\frac{t_i-t}{F}}) - \frac{N'FR}{F+R}(e^{\frac{(F+R)(t_f-t)}{FR}} \\ -e^{\frac{(F+R)(t_i-t)}{FR}}) + B, 4095)\,, & t > t_f \\ \mathrm{Min}(N'F(1 - e^{\frac{t_i-t}{F}}) \\ -\frac{N'FR}{F+R}(1 - e^{\frac{(F+R)(t_i-t)}{FR}}) + B, 4095)\,. & t < t_f \end{cases} \tag{3.3}$$

Figure 3.4 shows the simulated front-end board response of a single cell hit caused by a slow monopole with a known velocity and trajectory in the simulation and the predicted curve using the analytical form of Eq. 2.1 with the best fit N'. They

perfectly match up with each other.

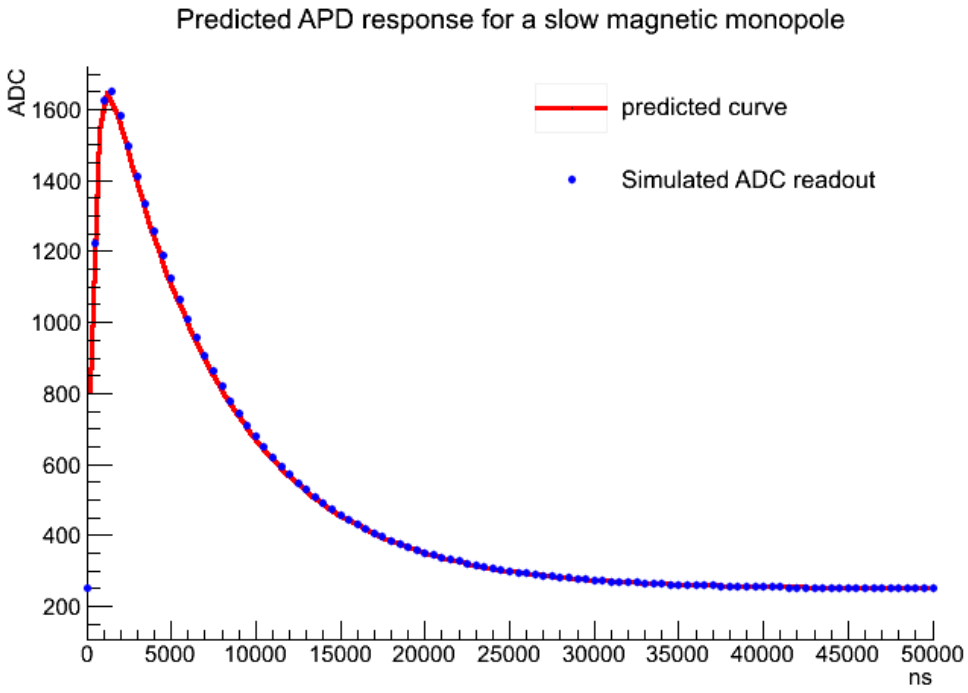

Figure 3.4: Simulation of the response of a slow magnetic monopole, with noise turned off.

The simulated noise is modeled by the sum of two Gaussian Markov chains representing current and voltage noise sources [47]. The current noise component is given by

$$A_I(t + \Delta t) = \frac{\Delta t}{F + \Delta t} G + \frac{F}{F + \Delta t} A_I(t)\,, \tag{3.4}$$

where G is a random number drawn from the unit Gaussian distribution ($\mu = 0$ and $\sigma = 1$), $\Delta t = 500$ ns, which is the time between digitizations, and the fall time $F = 7000$ ns. The voltage noise component is given by

$$A_V(t + \Delta t) = \frac{\Delta t}{R + \Delta t} G + \frac{R}{R + \Delta t} A_V(t)\,, \tag{3.5}$$

where the rise time $R = 382$ ns. The final noise trace is $aA_I + bA_V$ where a and b are determined through a fit to pedestal scan data.

3.2 Isotropic Generator

To determine the acceptance and efficiency of the monopole search, we assume the monopole flux is isotropic. To avoid unnecessary use of computation time in simulating the monopole's propagation outside of the detector's boundary, we start at the surfaces of the detector. The generator randomly assigns a surface ID number to determine on which surface the monopole starts. The probability of each starting surface is proportional to the surface area, as shown in Fig. 3.5.

Once the starting surface has been selected, the exact starting position on the surface is uniformly randomly generated. Then we set up a local coordinate system as shown in Fig. 3.6, with positive z axis perpendicular to the chosen starting surface and pointing into the detector. The direction of the monopole is determined as follows. The local azimuthal angle ϕ' is uniformly distributed in [0,2π], and $\cos\theta'$ (θ' is the local zenith angle) is uniformly distributed in (0,1], so that the generated monopole will enter the detector.

For validation, we plot the angular distribution of all the simulated monopoles in the global coordinate system, where positive x points west, positive y points up, and positive z points north. As shown in Fig. 3.7, we have a uniform distribution of azimuthal angle ϕ and cosine of zenith angle θ.

3.3 Simulation of Monopole's Propagation

We use the package *G4mplIonisationWithDeltaModel*, which was written by A. V. Bagulya, et al. [39], to simulate the monopole's propagation through matter. Since

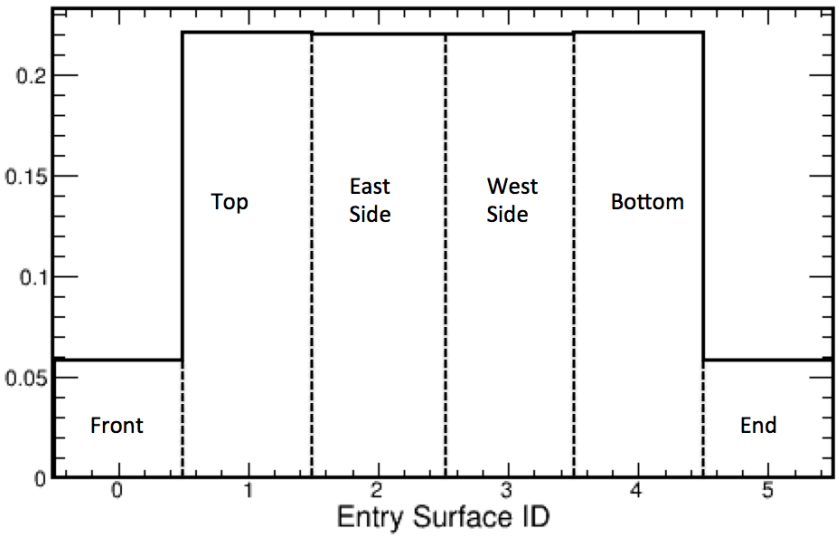

Figure 3.5: The distribution of surface ID numbers where the simulated monopole starts.

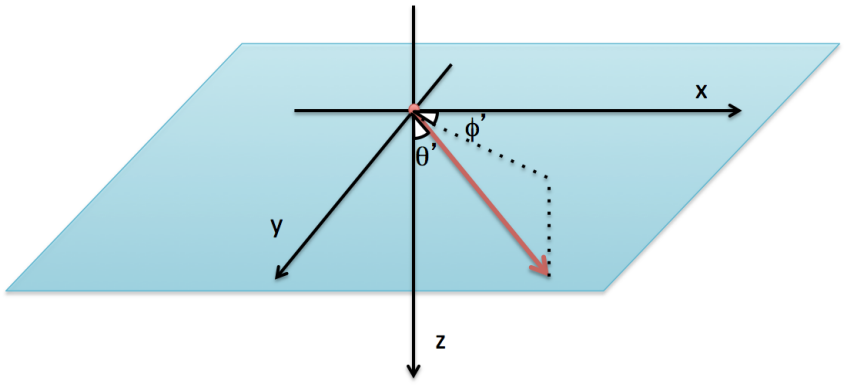

Figure 3.6: The local coordinate system: the z axis is chosen to point perpendicularly into the chosen starting surface in the XY plane.

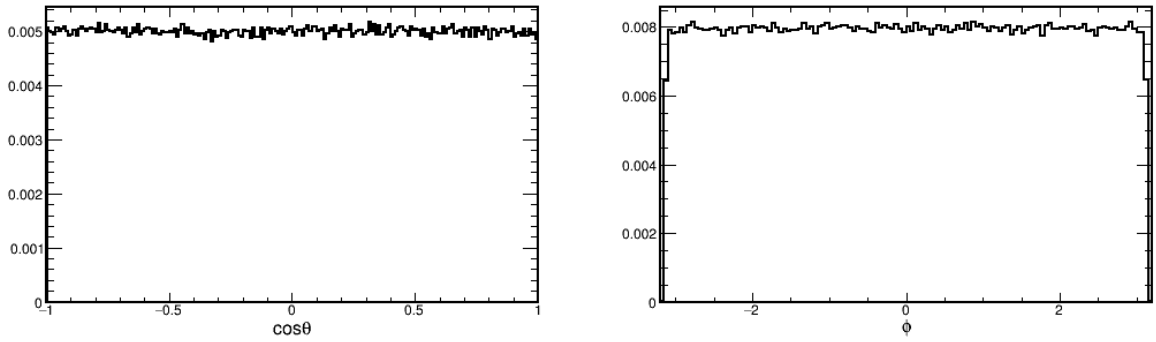

(a) (b)

Figure 3.7: Distribution of the (a) polar and (b) azimuthal angle of the generated monopoles, in the global coordinate system.

there is no applied magnetic field in the NOνA far detector, and the earth's field can be neglected, the ionization and atomic excitation processes are the most important part in simulating the magnetic monopole's propagation. However this package incorrectly calculates the energy loss of slow ($\beta < 0.01$) magnetic monopoles, by using the following improper approximation [39]:

$$\frac{dE}{dx} = 45\rho g\beta \text{ (GeV/cm)}\,, \tag{3.6}$$

where the density ρ is in units of g/cm^3, and g is the number of Dirac magnetic charges. This approximation is only correct when the material is silicon, which is not applicable for the simulation of the NOνA detector. We thus modified the source code and adopted Eq. 1.36.

To validate the modified simulation code, we have calculated the energy loss of slow monopoles in the NOνA scintillator, using Eq. 1.36. The electron density of the scintillator used in NOνA, 2.96×10^{23} cm^{-3}, is calculated from the composition given in Table 2.3. The comparison of the energy loss given by the MC in the Geant4 simulation, before and after the correction is shown in Fig. 3.8.

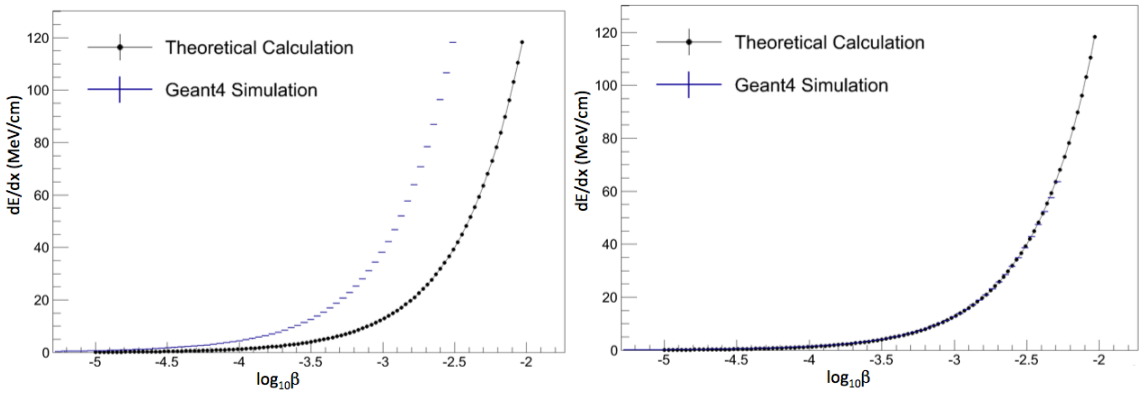

(a) (b)

Figure 3.8: Comparison of the theoretical prediction and simulation of the slow monopole energy loss vs β. We see the discrepancy in the (a) simulated result of Geant 4.9.5 without correction, and (b) the correction to Geant4 discussed in the text.

As discussed in Chapter 1, there are large uncertainties in the predictions of the monopole energy loss in matter. Hence, we perform an optimistic and a conservative estimate of the monopole energy loss, in addition to the standard energy loss adopted in the simulation. As discussed in Chapter 1, the optimistic estimate is set to 103% of the standard estimate, and the conservative estimate is set to 97% of the standard estimate, for monopoles with $\beta \geq 0.1$; while the optimistic estimate is set to 200% of the standard estimate, and the conservative estimate is set to 40% of the standard estimate, for monopoles with $\beta \leq 0.01$. In the intermediate velocity region $\beta \in (0.01, 0.1)$, a polynomial interpolation is adopted for both optimistic and conservative estimates, as is done with the treatment of the standard estimate in the simulation. This is shown in Fig. 3.9.

3.4 Light Yield Simulation

The scintillation light yield does not scale linearly with energy deposit but is quenched for heavily ionizing particles. In the simulation, the empirical formula

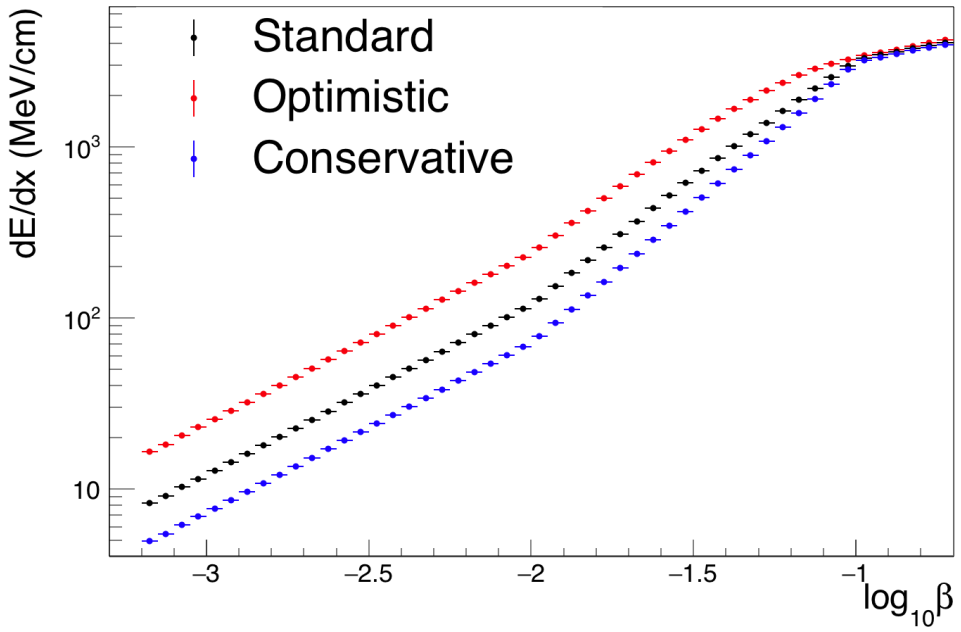

Figure 3.9: The energy loss of slow monopoles as a function of monopole speed. The bars in β represent the velocity bin size.

of Birks' Law [40] is adopted:

$$\frac{E_{vis}}{E_{true}} = \frac{\frac{dE}{dx}}{1 + \rho k_B \frac{dE}{dx}}, \tag{3.7}$$

where, ρ is the density of the scintillator in units of g·cm^{-2}, E_{true} is the energy deposit of the charged particle, and E_{vis} is the visible energy that is proportional to the light yield. Note that for large energy losses, the value E_{vis}/E_{true} is approximately $1/\rho k_B$, and is hence capped at that value.

The default value of k_B used by Geant4 for pseudocumene is 1.22×10^{-4} g·MeV^{-1}·cm^{-2}. This value is about 80 times smaller than the value $k_B = 9.4 \times 10^{-3}$ g·MeV^{-1}·cm^{-2}, given by Ref. [41]. In that reference a semi-empirical calculation of the Birks constant is made and then compared to the experimental data of protons [42] and alpha particles [43] [44] in pseudocumene. The agreement with both measurements is quite

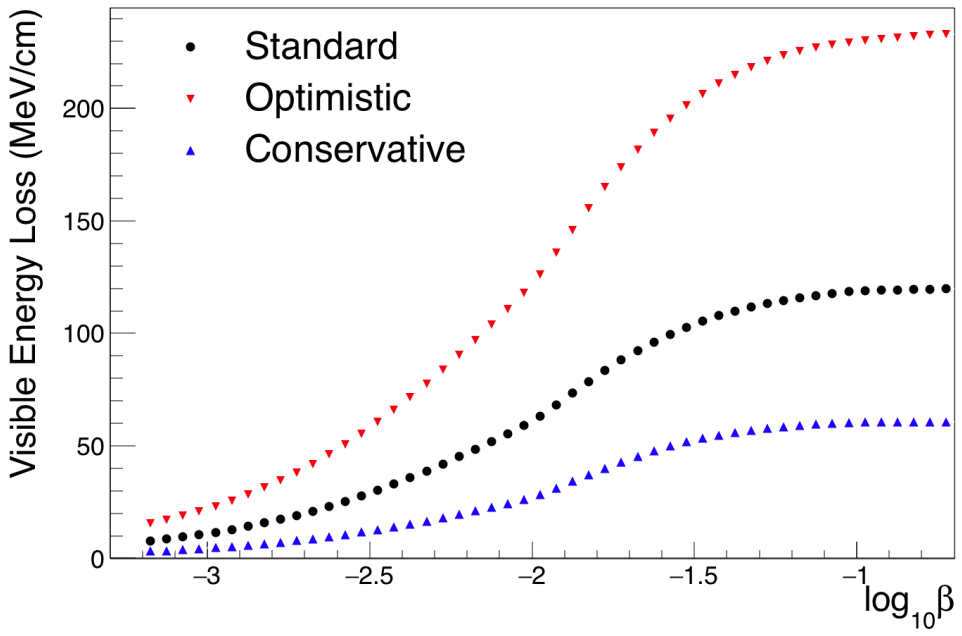

Figure 3.10: The visible energy (the true energy loss corrected by the Birks' law) as a function of monopole speed with the standard, optimistic and conservative estimates, with the uncertainties in both the theoretical model and light yield simulation included. The standard visible energy loss is obtained with the standard estimation of monopole energy loss convoluted with the Birks suppression (using $k_B = 9.4 \times 10^{-3}$ g/MeV·cm^2). The optimistic visible energy loss is obtained with the optimistic estimation of the monopole energy loss convoluted with an optimistic Birks suppression (using $k_B = 4.7 \times 10^{-3}$ g/MeV·cm^2). The conservative visible energy loss is obtained with the conservative estimation of the monopole energy loss convoluted with a conservative Birks suppression (using $k_B = 18.8 \times 10^{-3}$ g/MeV·cm^2).

good (and the result is consistent with other measurements [45]). We use this Birks' constant and set upper (lower) limit by a factor of 2 (1/2). The visible energy loss including the Birks suppression is shown in Fig. 3.10.

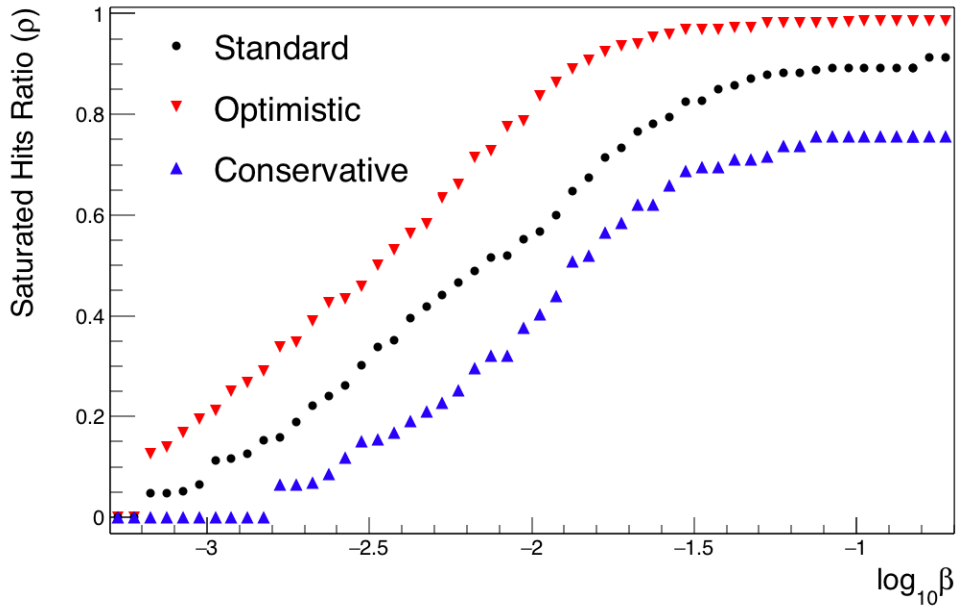

Figure 3.11: The probability that a monopole produces a saturated response in a cell as a function of its velocity, assuming an isotropic flux. The optimistic and conservative curves represent the systematic uncertainties in both the theoretical model and the light-yield simulation.

The probability that a hit gets saturated, referred to as the saturated hits ratio ρ, is one important selection variable used in the final analysis. The saturated hits ratio ρ as a function of monopole speed β is shown in Fig. 3.11. For monopoles with $\beta \lesssim 5 \times 10^{-4}$, the saturated hits ratio is extremely close to 0 and for monopoles with $\beta \gtrsim 0.1$, the saturated hits ratio reaches its maximum value.

3.5 Cosmic Ray Simulation

The background to the monopole search consists of cosmic-ray particles that strike the far detector at a very high rate. Muons are by far the majority, and are the

most penetrating species. NOνA adopted the CRY [46] package for the cosmic-ray simulation, which provides fluxes of different particles (muons, neutrons, protons, electrons, photons, and pions) within a 300 m $\times$ 300 m area at sea level at the latitude of 48.4°, the far detector site location. The list of particles is then passed to Geant4, which propagates particles through the overburden and the detector. As illustrated in Table 3.1, $\mu^{\pm}$, $e^{\pm}$ and γ comprise the majority of the cosmic particles and their secondaries.

Table 3.1: The rate of cosmic-ray particles entering NOνA far detector.

Particle	Rate (kHz)
$\mu^{\pm}$	144.7 ± 0.5
$e^{\pm}$	0.2 ± 0.08
γ	0.3 ± 0.01
n	4.0 ± 0.07
p	0.4 ± 0.02

3.6 The Monte Carlo Signal Data Set

The mass of simulated monopole is set very high, so that its velocity change is negligible along its path length inside the detector. We have simulated 3,400,000 isotropic monopoles with a fixed mass of $M = 10^{16}$ GeV/c^2, and uniformly random variation of 9.99×10^{15} GeV/c in momentum. This gives a uniform distribution of the monopole speed within the range $\beta \sim (10^{-4}, 0.2)$.[1] This simulated data set is used to evaluate the trigger and monopole identification efficiencies, which is discussed in the following chapters.

[1]For technical reasons it is extremely time consuming to simulate monopoles with $\beta > 0.2$ for low values of the Birks suppression. However, it is not necessary to go beyond $\beta = 0.2$ since the detector response is the same above $\beta = 0.2$.

Chapter 4

The Fast Monopole Trigger

The NOνA far detector produces about 1 GB of data per second, far more than can be sent to Fermilab to permanent storage. Moreover, the amount of data produced per year is far more than can be stored. Hence, only a fraction of the data can be recorded for offline analysis.

In order to record candidate magnetic monopole events with high efficiency we have implemented a software-based trigger. The trigger must be fast, have high efficiency, and here a large rejection factor for the over 100,000 cosmic rays that course through the detector every second. In this chapter, we first introduce the data-driven trigger (DDT) system, discussing the requirements for the fast monopole trigger. Then we describe in detail the algorithms of the monopole trigger, and its performance in efficiency, trigger rate and execution time. See Appendix A for information of the slow monopole trigger, whose data were not used in the analysis.

4.1 Introduction to the Data-Driven Trigger System

The data produced by every detector cell is buffered for real time analysis by the data-driven trigger (DDT) system. The decision to record or discard data can thus be

based on complex event topologies. A schematic overview of the NOνA DAQ system with the integrated data-driven trigger is shown in Fig. 4.1. Data from the front-end boards (FEB) are sent to the data concentrator modules (DCM). Each DCM collects a piece (typically 2,098 cells) of milliblock data (5 ms of data) and sends it via a fast switch to a buffer node for temporary storage. Each buffer node contains a 5 ms slice of the data produced by the entire far detector.

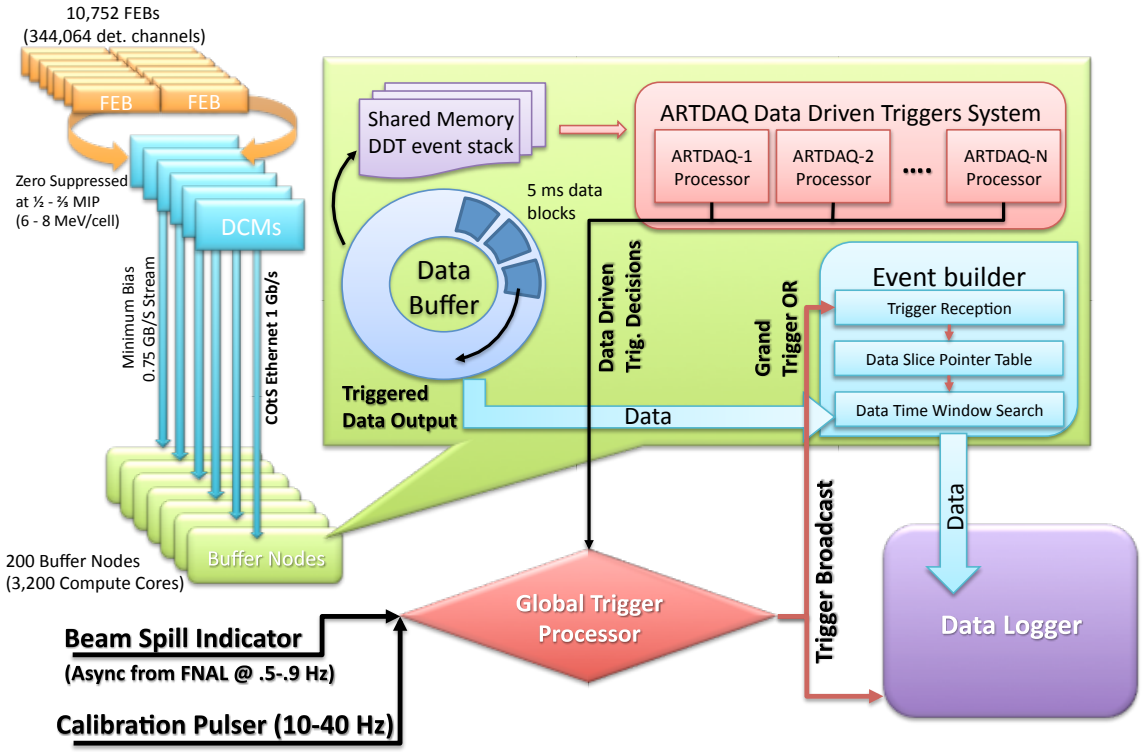

Figure 4.1: The NOνA DAQ readout showing the DDT (data-driven trigger) system. Note that not all of the 200 buffer nodes were installed at the time covered by this analysis. Rather, we had 47 buffer nodes on average.

The DDT runs in parallel on every buffer node and receives the data through a shared memory segment. This shared memory segment acts as a queue for the milliblocks as they arrive to the DAQ. The queue depth can be changed to contain any number of milliblocks desired. When the queue is full, the oldest milliblock is overwritten. In order to avoid dropping milliblocks before the trigger algorithms have

a chance to operate on them, we run in parallel the different trigger algorithms of the DDT, all of whom read from the same shared memory segment. There is not enough time[1] to fully reconstruct all of the events in the far detector within the buffer storage time, so we have been compelled to design fast data handling and analysis methods.

There are currently eight triggers implemented in the DDT framework including two monopole triggers: one focusing on fast, highly ionizing monopoles, and the other on subliminal monopoles and other slowly ($\beta \lesssim 0.01$) moving exotic charged particles. A positive trigger decision issues a time window within the 5 ms-long milliblock data. This is illustrated in Fig. 4.2: the length of the data read out is the smallest time window containing the event in units of 50 μs. Data-driven triggers with different algorithms are likely to issue different time windows when operating on the same milliblock of data stored in a buffer node; thus the data triggered by different algorithms or configurations is sent to separate data streams.

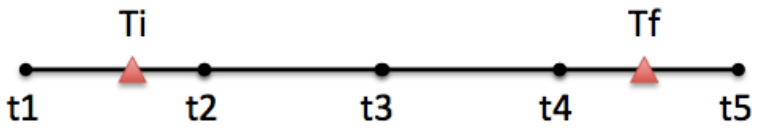

Figure 4.2: An illustration of the data recorded by a data-driven trigger with an issued trigger window of $[T_i,T_f]$. The shortest time window allowed to be read out is $t_{i+1} - t_i = 50\,\mu$s, hence the data read out in this case includes a time window of $[t_1,t_5]$.

With 47 buffer nodes[2], each with 16 to 32 cores and each running 13 processes, all the trigger decisions and their corresponding service modules are required to be finished within 3 seconds or the data is lost. This mandates fast and efficient trigger

[1] We have only roughly 3 seconds to make all the trigger decisions for each milliblock with 47 buffer nodes.

[2] This is the average number of buffer nodes enrolled in DAQ during the data taking period for this analysis.

modules, as well as organizing the entire trigger system in an optimized way.[3] Note that the main neutrino trigger is also run in the DDT framework. However, rather than using reconstruction algorithms operating on the data, it receives a time signal from the accelerator at Fermilab telling it when the neutrinos were produced, and after adding the appropriate time-of-flight delay, determines the correct time window to be sent to permanent storage. Note too that a pulser trigger is used which simply records a 550 μs-long time period called minimum-bias data, which is used for calibration and data quality check.

4.2 The Fast Monopole Trigger Algorithm

The primary goal of the fast monopole trigger is to record a potential signal event while rejecting many background cosmic-ray events to keep the transferred data rate below the bandwidth budget.

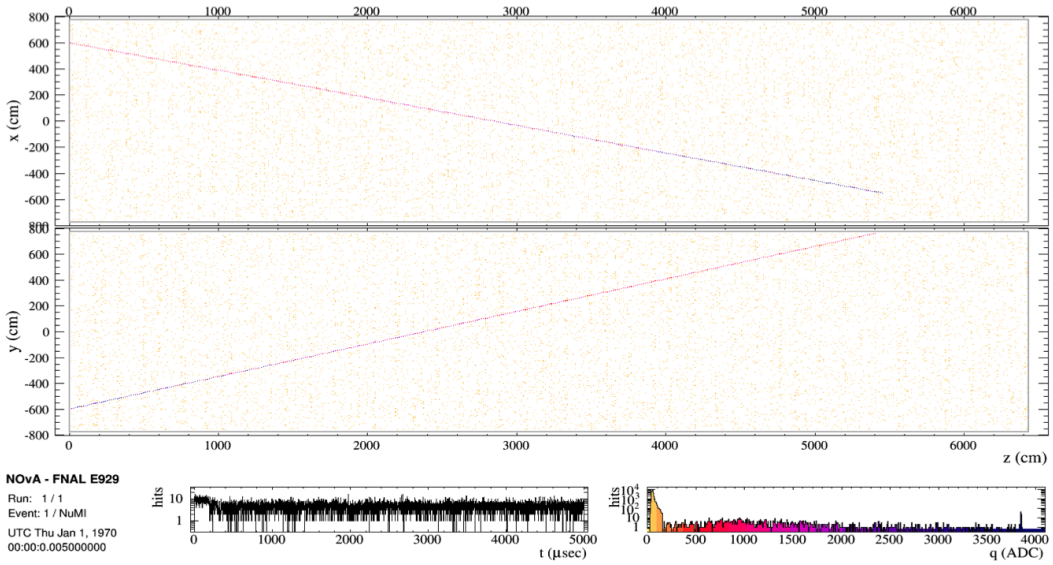

Figure 4.3: The event display of a simulated monopole with $\beta = 0.01$ and mass 10^{16} GeV penetrating the detector.

[3]Some service modules, such as that which sorts the input hits by their time order, are required by most of the triggers. These service modules are not run repeatedly for the same input milliblock data.

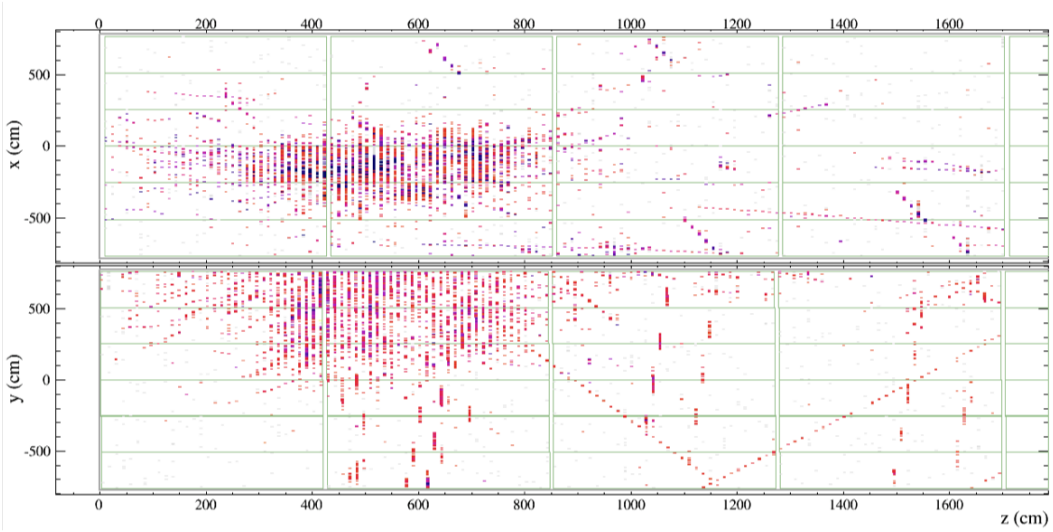

Figure 4.4: The event display of a high-energy cosmic ray event with showers, recorded by the high-energy trigger.

The signature of a fast monopole is a straight track that is heavily ionizing with some saturated hits, indicated by the simulation shown in Fig. 4.3. The major background is high-energy charged particles from cosmic rays or their secondaries, like the high-energy event in Fig. 4.4. Before a trigger decision can be made, the process of clustering data that are all associated with a same event is needed, so that the trigger decision is made based on a subgroup of hits within a certain restricted time window in the entire 5 ms milliblock data. This clustering is called slicing and is explained in the next section.

4.2.1 Slicing Algorithms for the Fast Monopole Trigger

In NOνA, a spatially and temporally correlated group of hits is called a slice. In DDT framework, we use the sliding-window algorithm to cluster hits which are causally and spatially correlated, which is achieved by two slicing modules: TimeSlice and SpaceSlice. The products of these two modules are groups of hits, referred to as space-time slices.

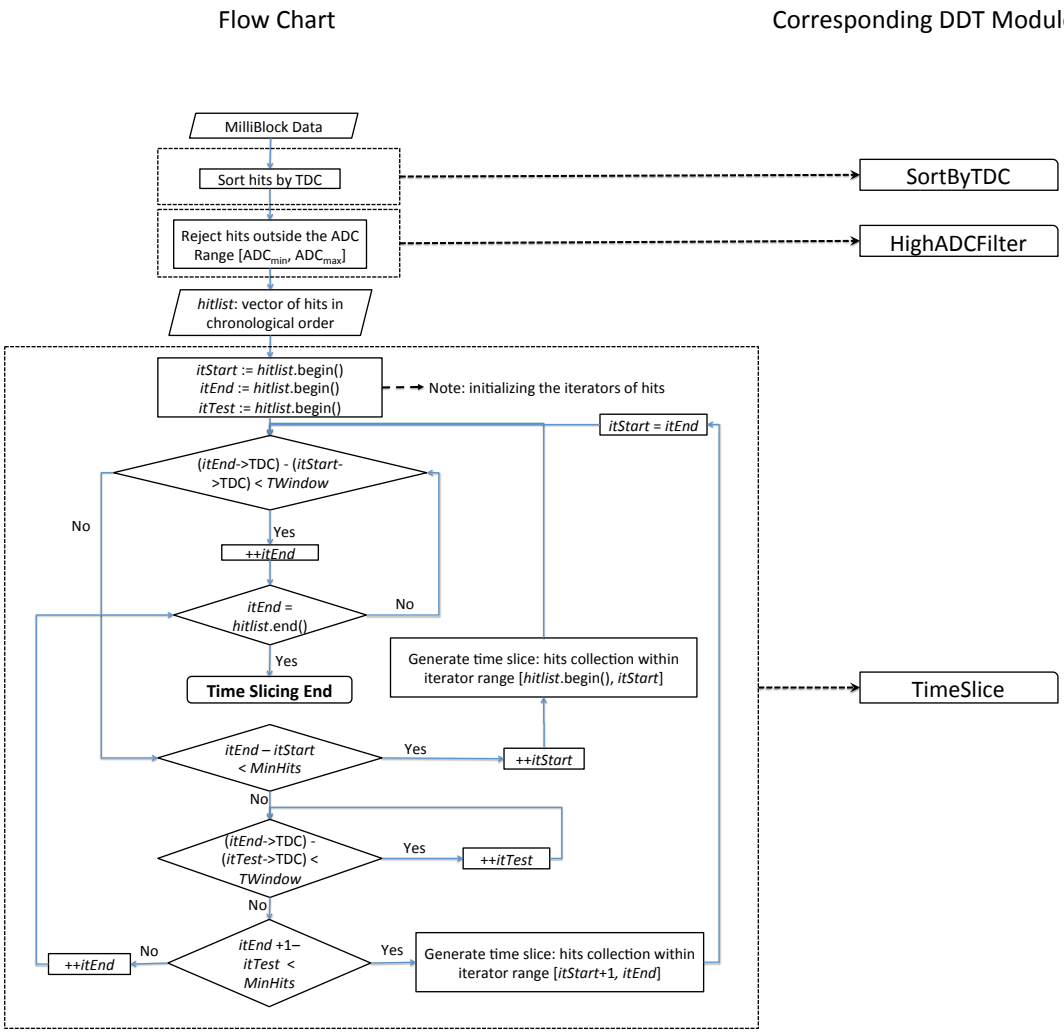

Figure 4.5: The flow chart of the algorithm that separate hits into different groups based on their time information. The ADC_{min} is set to 500 and ADC_{max} is 4095 (the maximum ADC value). The names of the corresponding DDT modules are listed on the right. SortByTDC is a module that sorts all the hits by their time. HighADCFilter filters out all the hits which are outside the ADC range. TimeSlice loops through all the remaining hits that are time ordered and groups them into different slices.

The fast monopole trigger algorithm acts on each space-time slice. A space-time slice reconstructed with the fast monopole trigger specific configuration is a collection of hits, each with DCS values not less than 500 ADC (approximately 1 to 8 MIPs). It is required that within any time window of 3125 ns (200 TDC) inside the slice, there be at least 10 hits without any single gap longer than 3 planes. These values have been tuned using the minimum-bias cosmic data and the standard Monte Carlo signal data set. The larger the time window is, the larger the possibility that the slice can include all the hits caused by a potential monopole track. However, if the time window is too large, too many hits are associated with the slice, which produces a large and useless slice containing too many background hits.

The TimeSlice algorithm and its service modules is shown as a flow chart in Fig. 4.5. Since sorting the hits by time is needed by every trigger algorithm at an early stage, and filtering hits based on their DCS values is not, we do sorting first, although reversing the order would speed up the fast monopole trigger. Note that the TimeSlice is done before SpaceSlice. If a time slice contains at least 10 hits, it is further sliced into smaller[4] clusters of hits based on their spacial distribution by the module SpaceSlice. Otherwise, that time slice is ignored. The algorithm is quite similar to TimeSlice, as shown by the flow chart of Fig. 4.6.

The parameters of TimeSlice and SpaceSlice have been tuned for triggering on monopoles with $\beta \gtrsim 0.01$. The failure rate of slicing the monopole hits will significantly increase for slower monopoles as it is limited by the size of the sliding time window, and the minimum ADC threshold.[5]

[4] If all the hits in the TimeSlice are also spatially correlated, then all the hits in the TimeSlice would be clustered into one SpaceSlice.

[5] As long as a slice contains enough monopole hits to allow the fast monopole trigger issue a trigger window with a fully contained monopole event, the slicing process is considered to be a success.

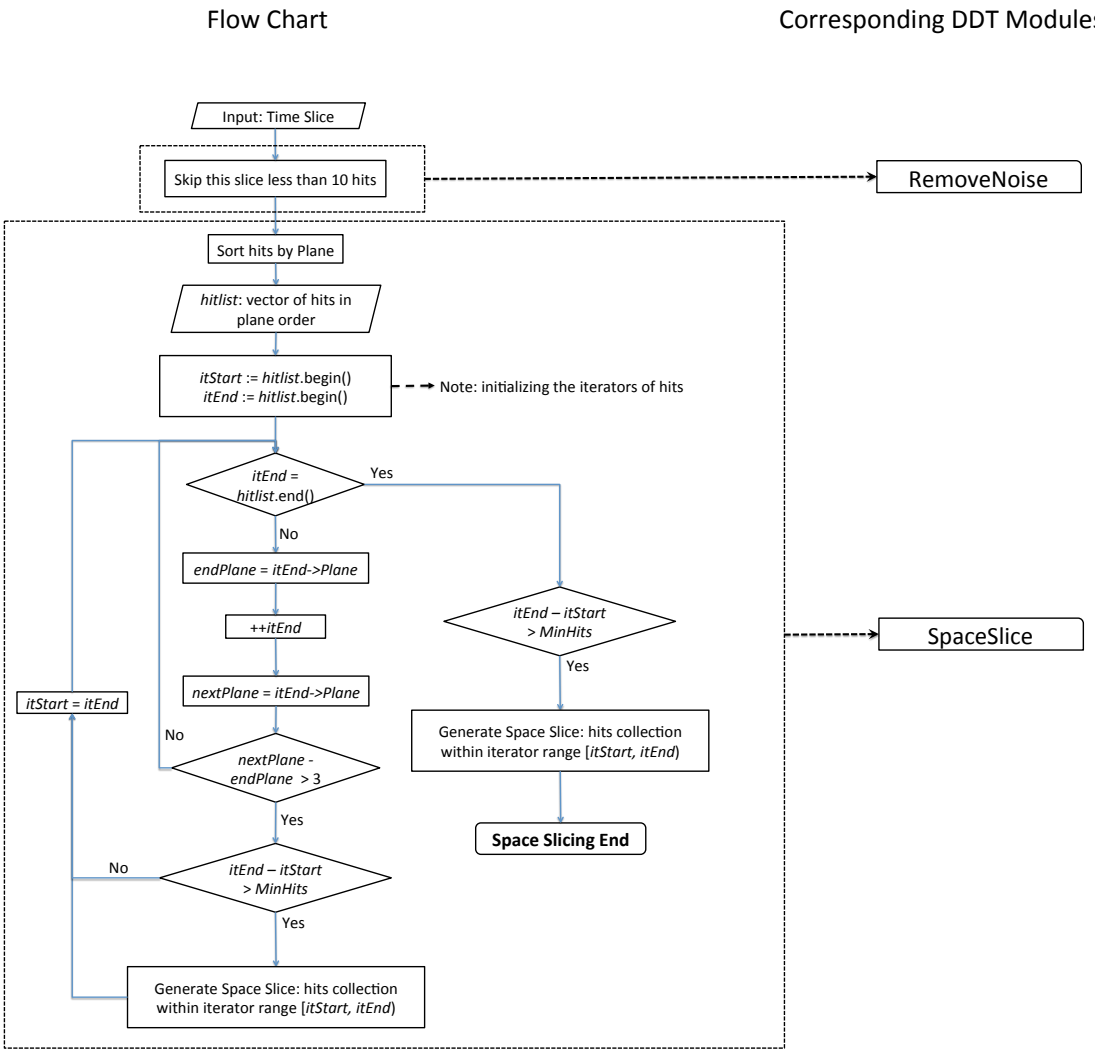

Figure 4.6: The flow chart of the algorithm that divides hits into groups based on their spatial separation. We use the notation "a:=b" to denote an operation in which we set the value of a variable a to be equal to the value b.

4.2.2 Monte Carlo Tests of Space-time Slicing Performance and Efficiency

To evaluate the slicing performance for the fast monopole trigger, we use the following two metrics:

- **Purity**: the number of hits in the slice caused by the target monopole divided by the total number of hits included in the slice,
- **Inclusiveness**: the number of hits in the slice caused by the target monopole divided by the total number of hits caused by the target monopole.

A perfectly reconstructed slice would include all the hits caused by a specific monopole event and simultaneously filter out all the background hits, i.e., would have purity and inclusiveness both equal to one. However, this task becomes more and more difficult as the velocity of monopole gets smaller, as any two adjacent monopole hits are further separated in time, and cosmic-ray background events increase. Simply increasing the size of the time window would eventually end up clustering all the hits into one huge slice.

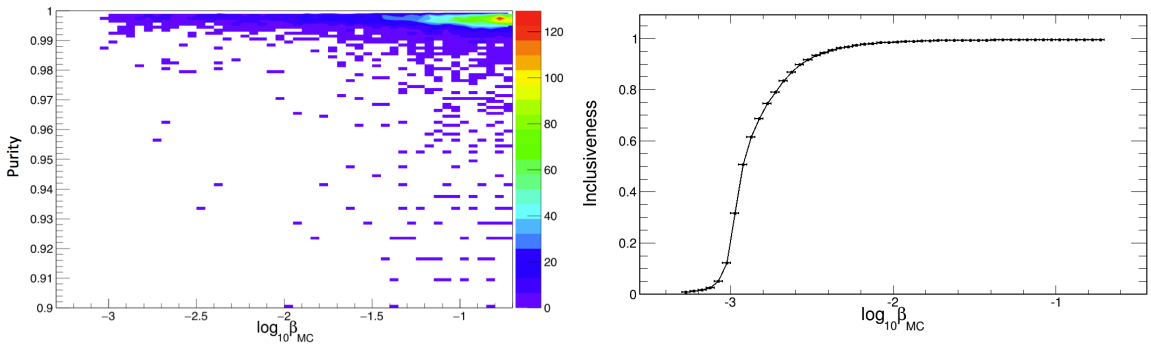

(a) (b)

Figure 4.7: Performance of the monopole trigger on simulated monopole events with added electronic noise: (a) the purity and (b) the inclusiveness of the slicer configured for the fast monopole trigger as a function of the monopole velocity.

An evaluation of the slicing performance has been made using large sets of isotropic monopoles (with β uniformly distributed from 1×10^{-4} to 0.2) with simulated electronic noise.[6] The high ADC threshold removes most of the noise hits. A high purity monopole sample remains, shown in Fig. 4.7(a). The inclusiveness decreases with slower monopoles, as their hits are further separated in time. The overall slicing efficiency as a function of monopole speed is shown in Fig. 4.8.

A successfully reconstructed fast monopole slice is the basis of a successful fast monopole trigger decision. A small fraction (3.37%) of fast ($\beta > 0.01$) monopole events fail the slice reconstruction mainly due to lack of hits, as illustrated in Fig. 4.9(a). Monopoles going almost vertically have a greater chance to go through the gaps between two adjacent planes, or to hit only a few vertical cells, thus leaving too few cell hits for reconstruction, as indicated by the peak in Fig. 4.10. For significantly slower ($\beta < 0.01$) monopoles, the energy deposited in each cell may not be enough to produce a hit, or for a produced hit to pass the ADC cut. The smaller energy deposited in the detector cells becomes the dominant cause for these monopoles to fail the slice reconstruction, as shown in Fig. 4.9(b).

The slicing algorithm has been tested with 400 milliblocks (5 ms length each) of minimum-bias far detector data as well. Figure 4.11 shows the distribution of the number of overlapping planes in both space and time of hits from both views which are clustered into one space-time slice, and Fig. 4.12 shows the same distribution for the MC signal data set. Figure 4.13 show the number of high-energy hits (those with DCS values larger than 3100 ADC) and the average DCS value of the hits in each reconstructed space-time slice, and Fig. 4.14 shows the same distribution for

[6]Hits of faster monopoles have less variation in time and higher DCS values in general; thus monopoles with higher velocity ($\beta > 0.2$) will generally have a better chance of being grouped into one slice and deposit more energy in the detector, which leads to a greater chance to be triggered by the fast monopole trigger.

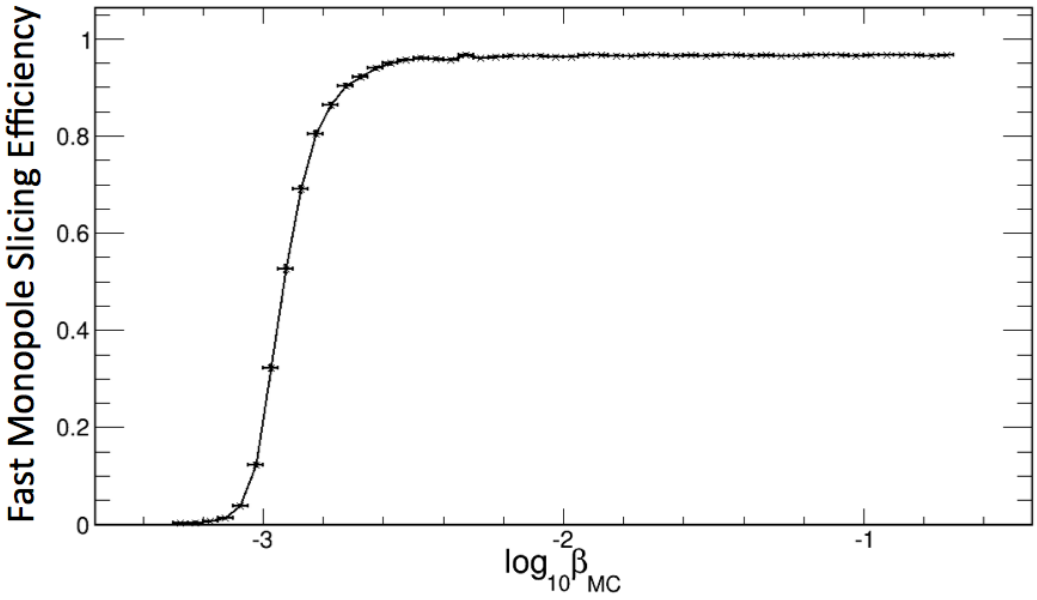

Figure 4.8: The efficiency of slicing for the fast monopole trigger as a function of the monopole velocity.

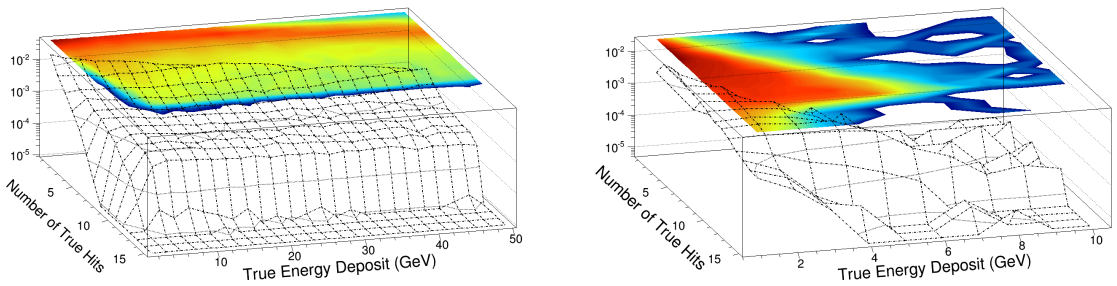

(a) (b)

Figure 4.9: Total energy and number of hits for monopole events that fail (a) the fast ($\beta > 0.01$) and (b) slow ($10^{-4} < \beta < 0.01$) monopole slicing. The plots have been normalized to one. The same slicer was used in both cases.

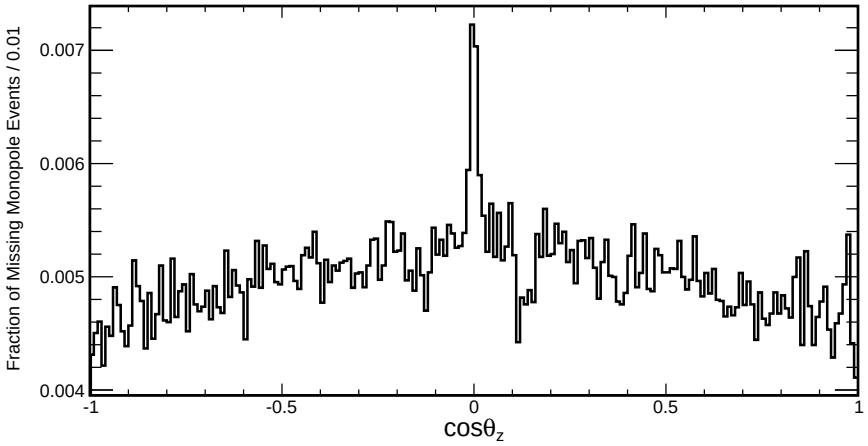

Figure 4.10: The polar angular distribution of fast ($\beta > 0.01$) monopoles which failed the reconstruction of a fast monopole trigger slice. We adopt the global coordinate system where the Z axis is directed north.

the signal MC data set. We discuss the trigger cuts on those quantities in the next section.

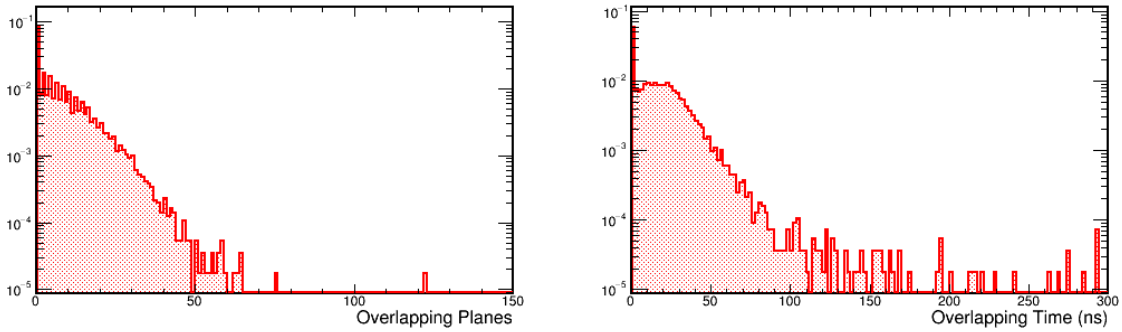

(a) (b)

Figure 4.11: The fraction of overlapping (a) planes and (b) time of hits in both views in one space-time slice reconstructed with 2 s of minimum-bias data.

4.2.3 Fast Monopole Trigger Cuts

At the trigger level we do not do three-dimensional tracking due to time constrains so the absolute energy calibration with the attenuation correction is absent throughout the trigger decision making process. Based on the information of all the hits

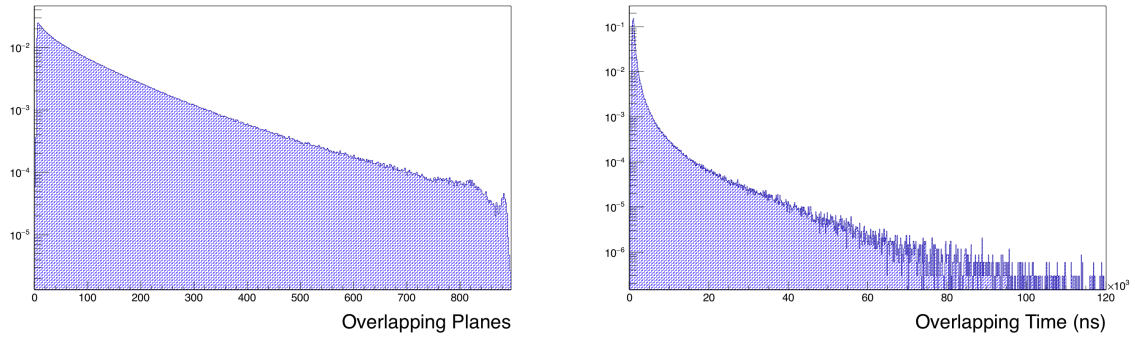

(a) (b)

Figure 4.12: The fraction of overlapping (a) planes and (b) time of hits in both views in one space-time slice reconstructed using the standard Monte Carlo signal data set.

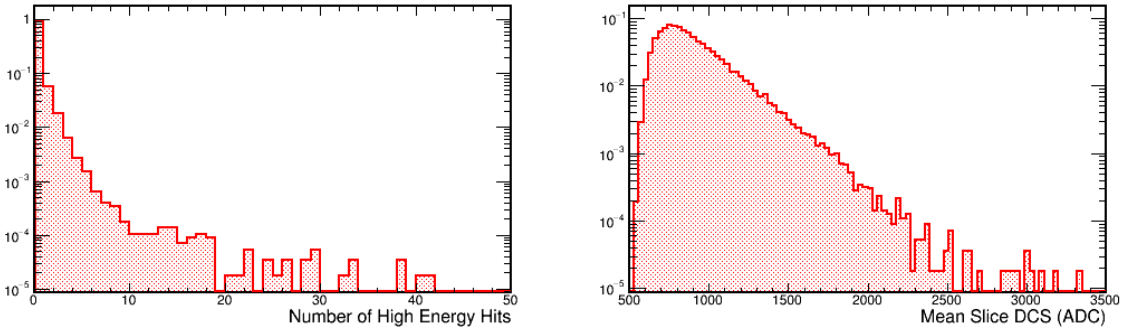

(a) (b)

Figure 4.13: The distribution of (a) number of high-energy hits and (b) mean DCS value of one space-time slice reconstructed with 2 s of minimum-bias data.

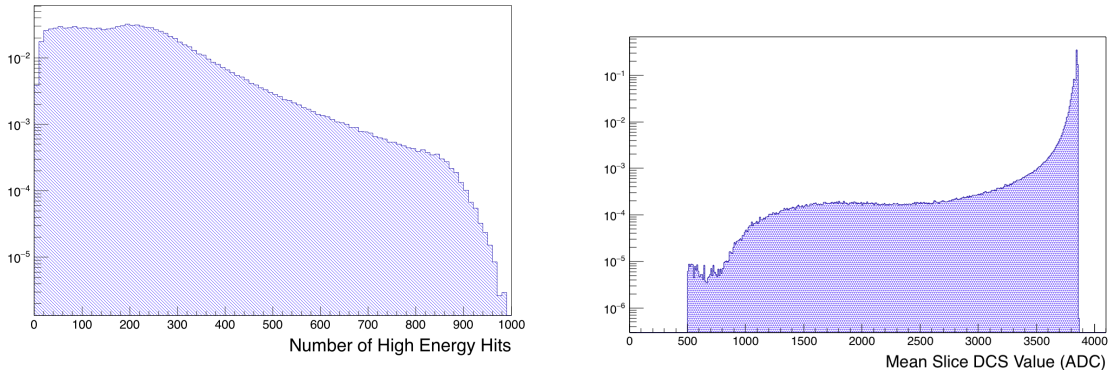

(a) (b)

Figure 4.14: The distribution of the (a) number of high-energy hits and (b) mean DCS value of one space-time slice reconstructed using the standard Monte Carlo signal data set.

in a space-time slice, the fast monopole trigger will decide whether a slice contains a possible fast monopole track. If so, it issues a trigger window, which is the time range of the slice plus a time buffer of 50 TDC counts (781.25 ns) on each end. This decision is based on a series of trigger requirements (cuts) which are described below. Their values are given in Table 4.1.

- **Cut 1: Minimum-Hits Requirement** – We need to reconstruct a track in three dimensions in the offline; thus we require enough hits in both X and Y views to do so. The offline track-fitting algorithm requires at least 3 hits to reconstruct the projection of the track in each view, hence, this is what is required at the trigger level.

- **Cut 2: Penetration Test** – Magnetic monopoles are extremely unlikely to be stopped within the detector; thus we require at least two different hits in the slice to be close to two different surfaces of the detector. Note that this is only a necessary but not a sufficient requirement. A slice containing a cosmic track coming from a corner of the detector but not deeply penetrating through the detector is very likely to pass this test. Two parameters: $\Delta plane$ and $\Delta cell$, determine whether a hit is close to a surface. Plane 0 is first and Plane 895 (the largest plane number) is at the ends of the far detector. A cell whose number is close to 0 or 383 is near the sides of the detector. The parameters $\Delta plane$ and $\Delta cell$ represent the distance of a hit from the boundary of the detector in number of planes and cells respectively.

- **Cut 3: Space-Matching Test** – A minimum number of overlapping planes (P_{ol}) is required to correlate tracks in different views in order to produce a 3D track. The number of overlapping planes is determined by:

$$P_{ol} = \min(P_{xmax}, P_{ymax}) - \max(P_{xmin}, P_{ymin}) \,, \tag{4.1}$$

where $P_{x(y)max(min)}$ corresponds to the maximum (minimum) plane number of the X(Y) view hits in the slice.

- **Cut 4: Time-Matching Test** – We require some hits that overlap in time (T_{ol}) from different views to check the causal correlation of hits in different views. This parameter is determined by :

$$T_{ol} = \min(T_{xmax}, T_{ymax}) - \max(T_{xmin}, T_{ymin}) \,, \tag{4.2}$$

  where $T_{x(y)max(min)}$ corresponds to the maximum (minimum) time of the X(Y) view hits in the slice.

- **Cut 5: High-energy Hits Cut** – Fast monopoles are so heavily ionizing that they usually deposit much energy in a cell. A minimum number of hits with a DCS value larger than 3100 ADC (N_{high}) is required.

- **Cut 6: Mean Energy Cut** – Not only do we require a minimum number of hits with a high ADC value but also a high average ADC value. The average DCS value ($E_{<ADC>}$) of all hits in a slice is the final cut made in the trigger decision.

An additional merit of the second cut, the Penetration Test is to filter out the large fraction of non-physics slices caused by hot APDs. The Space-Matching and Time-Matching cuts further help in filtering out non-physics slices caused by hot APDs close to the detector boundary (and thus passing the Penetration Test). These three cuts help keep the fast monopole trigger rate low and stable particularly when the detector is in an abnormal state with a lot of hot channels. The High-energy Hits Cut has the highest rejection rate for minimum-bias data, while the Mean Energy Cut also plays a key role in filtering out many high-energy cosmic events with electron or hadronic showers, like the event shown in Fig. 4.3(b). Though such events can have

plenty of high-energy hits, allowing them to pass the High-energy Hits cut, they are cut out by the Mean Energy Cut due to the many hits with low ADC values caused by the secondaries. This cut keeps the average rate of the fast monopole trigger below 25 Hz while preserving the trigger efficiency.[7]

The seven cut parameters for the fast monopole trigger are listed in Table 4.1. Their values have been tuned using both simulation (simulated isotropic monopoles with β uniformly distributed within the range (0.01,0.2)) and real minimum-bias data, to achieve an efficiency as high as possible while keeping the trigger rate stable and under 25 Hz.

Table 4.1: The list of parameters cut on for the fast monopole trigger.

Parameter	Name	Minimum Value	Maximum Value	Trigger Value
1	$Hits_{min}$	1	–	3
2	$\Delta Plane_{min}$	2	895	15
3	$\Delta Cell_{min}$	2	383	35
4	P_{olmin}	1	894	3
5	T_{olmin}	0	5 ms	0
6	N_{high}	1	975	6
7	$E_{<ADC>min}$	500	4095	1200

The performance of each trigger cut is summarized in Table 4.2, where the implicit Cut 0 represents the requirement that a fast monopole slice is reconstructed, and where the standard energy loss and light yield simulation is applied. The rejection fraction of MC monopole events and the rejection rate of minimum-bias events listed in Table 4.2, is based on each cut alone all using slicing. The remaining efficiency in Table 4.2 represents the fraction of MC events that remain after the corresponding previous cuts. The final remaining efficiency of 81.03% is the overall fast monopole trigger efficiency on the Monte Carlo signal data set.

[7] A simple pattern recognition algorithm distinguishing showers from tracks can do the same (or better) than the mean energy cut, and several algorithms were written and tested, but found to take too much execution time and CPU resources.

Table 4.2: Summary of the fast monopole trigger cuts performance.

Cut	Remaining Efficiency (MC)	Rejection Fraction (MC)	Trigger Rate (Data)	Rejection Fraction (Data)
0	96.63%	3.37×10^{-2}	42128 Hz	–
1	94.01%	2.71×10^{-2}	6269 Hz	0.851
2	92.88%	2.71×10^{-2}	2200 Hz	0.922
3	90.47%	2.59×10^{-2}	2032 Hz	0.845
4	90.47%	9.33×10^{-5}	1960 Hz	0.836
5	85.26%	8.67×10^{-2}	20 Hz	0.996
6	81.03%	11.3×10^{-2}	19 Hz	0.903

4.2.4 Fast Monopole Trigger Efficiency and Performance

The cosmic-ray Monte Carlo CRY used by NOνA, does not simulate the very high-energy cosmic particles seen in the data, and indeed the fast monopole trigger never triggers on simulated cosmic-ray events. Simulated noise hits overlaid with simulated monopole events does not agree with the DCS spectrum of minimum-bias data in far detector shown in Fig. 4.15. Thus, we developed the following mechanism to evaluate the mean DCS value of a reconstructed slice based on the DCS spectrum of minimum-bias data.

Background hits (including both electronic noise hits and cosmic-ray hits) do not decrease the acceptance for monopoles, aside from Cut 7 (Mean Energy Cut). Underestimation of the background hits with DCS values between 500 ADC and the mean DCS value of true monopole hits may reduce the average DCS value of the slice by reducing the purity of the slice. Hence we reevaluated the mean DCS value of each space-time slice using the DCS spectrum of real data to estimate the effect of backgrounds on the trigger acceptance.

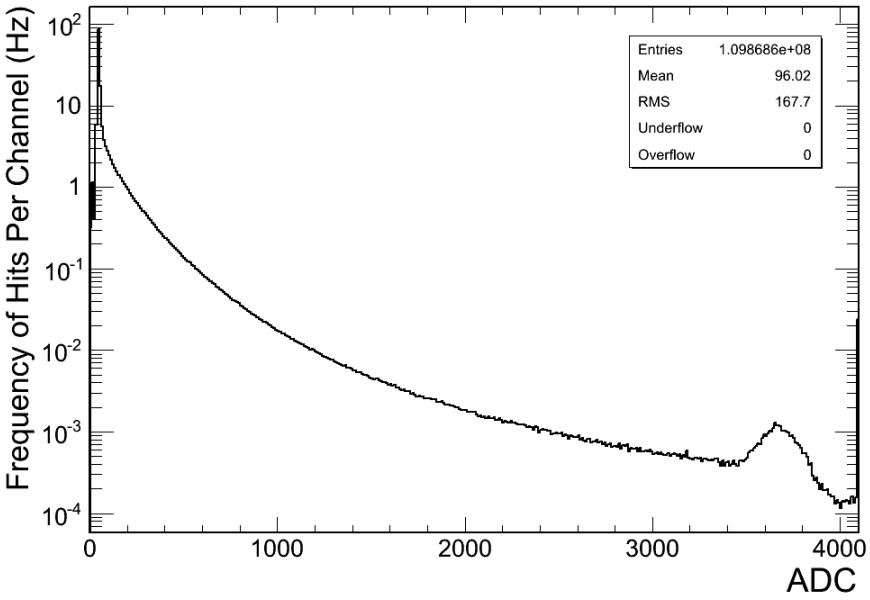

Figure 4.15: The DCS spectrum of all the hits in all channels in minimum-bias far detector data.

For a space-time slice with ΔP planes and a time window of ΔT, the expected number of background hits per slice with DCS value between q and $q + dq$ is:

$$f(q)dq\Delta VT_{ext}\,, \tag{4.3}$$

where $f(q)$ is the frequency density of hits per cell with DCS values between q and $q + dq$, provided by the DCS spectrum of minimum-bias data, shown in Fig. 4.15. The fiducial volume ΔV covered by the slice is expressed as $384(\Delta P + 6)$, given that each plane contains 384 cells and ΔP is the extend of the slice in planes. The extended time window is $T_{ext} = (\Delta T + 6250$ ns), where ΔT is the time window of the slice. A spatial range (3 planes) and the time gap (3125 ns) have been added to both ends. After a slice is reconstructed, we evaluate the mean DCS value of the slice by calculating the influence of the background hits which are not simulated in our MC signal data set, using the DCS spectrum from real data.

The efficiency estimation[8] of the fast monopole trigger on monopoles with one Dirac magnetic charge (g_D) is shown in Fig. 4.16. For monopoles with higher speeds ($\beta > 0.2$), the trigger efficiencies are assumed not to increase, but remain at their plateaued values.

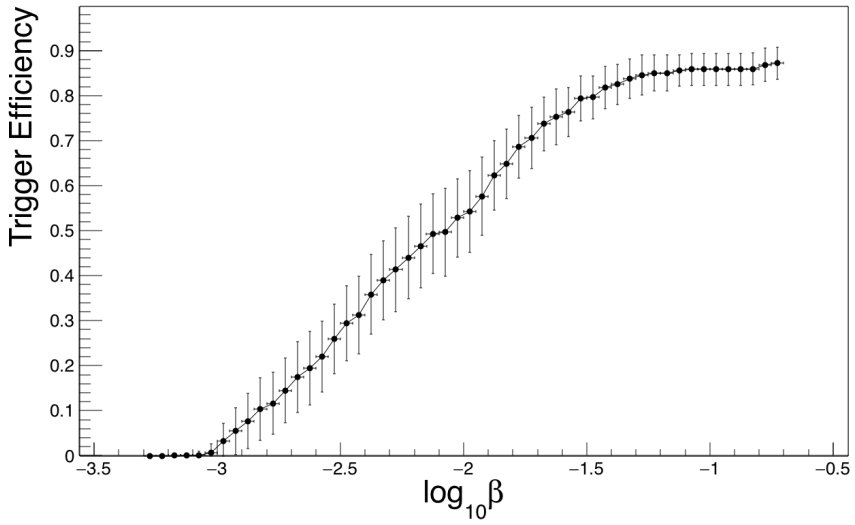

Figure 4.16: The Monte Carlo estimate of the efficiency of the fast monopole trigger as a function of the monopole velocity with one Dirac magnetic charge (g_D). The bars in efficiency include systematic and statistical uncertainties, and the bars in β represent the velocity bin size.

To prevent the fast monopole trigger rate from getting too high when the detector is behaving poorly with lots of hot channels or dead FEBs, we have implemented a trigger rate cap of 30 Hz for the fast monopole trigger. The usual trigger rate of fast monopoles is around 16 Hz, as illustrated in Fig. 4.17.

[8]To estimate the uncertainty in the trigger efficiency we first calculate it using the standard, optimistic, and conservative energy loss curves given in Fig. 3.9, each using the best value (9.4×10^{-3} g/MeV·cm^2) of the Birks' constant to give the visible energy. We then calculate the trigger efficiency using the standard energy loss curve, first using the high (18.8×10^{-3} g/MeV·cm^2) and then the low (4.7×10^{-3} g/MeV·cm^2) values of the Birks' constant. We then add the variations in efficiency quadratically to produce the uncertainties shown in Fig. 4.16.

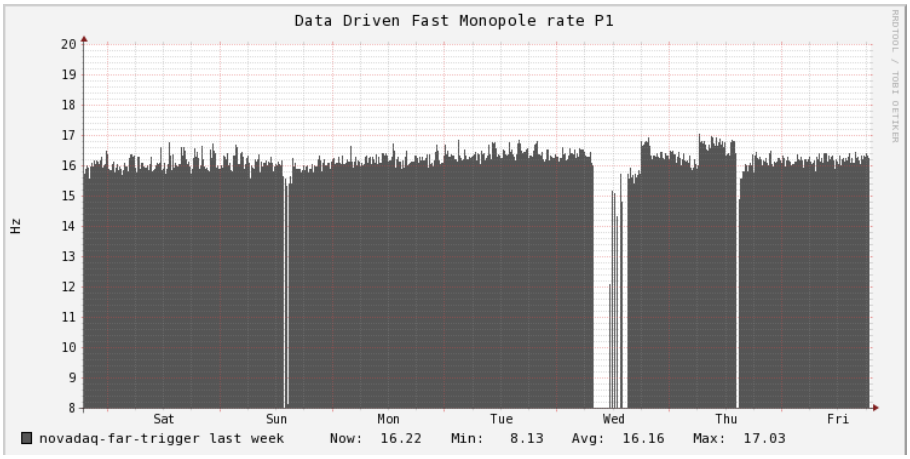

Figure 4.17: The fast monopole trigger rate during a typical week.

Chapter 5

Offline Reconstruction of Fast Monopole Tracks

The raw data recorded by the fast monopole trigger contains all the information of every cell hit within the issued trigger time window. To determine if it contains a monopole track we need to pick out all the hits associated with a potential monopole track first. Then we obtain the velocity, the calibrated energy deposit, etc. All the event reconstruction tasks we need to do but don't have time at the trigger level are done in the offline analysis.

The first step in the offline reconstruction of monopole events is reconstructing each single cell hit, which has been described in detail in Chapter 2. Then we reproduce the procedure of the slicing algorithm as used in the fast monopole trigger, to find collections of hits which are correlated in both time and space. The reconstruction of monopole tracks described below is based on each reconstructed space-time slice.

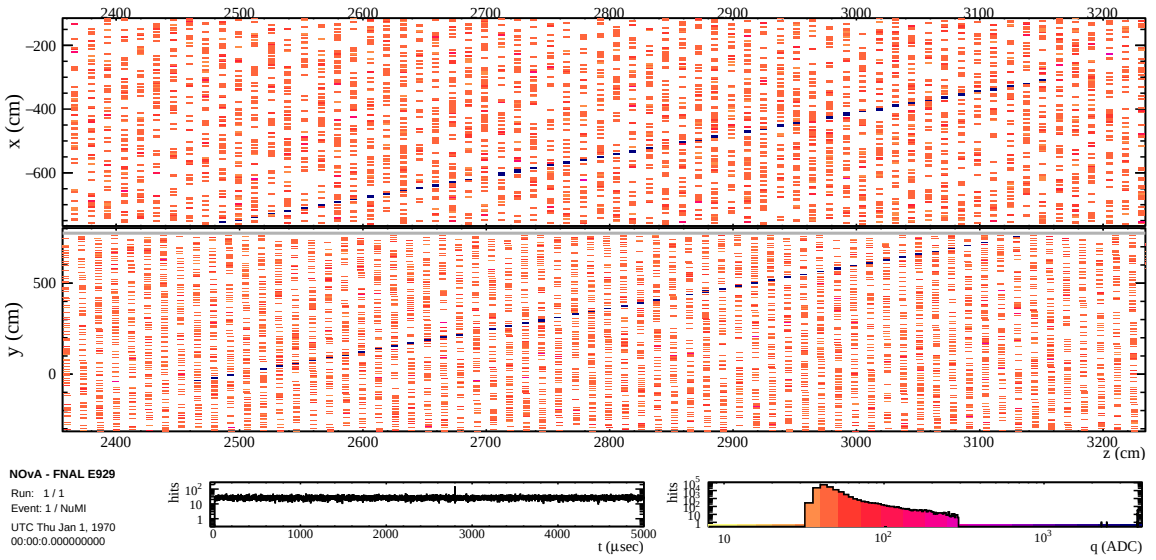

(a)

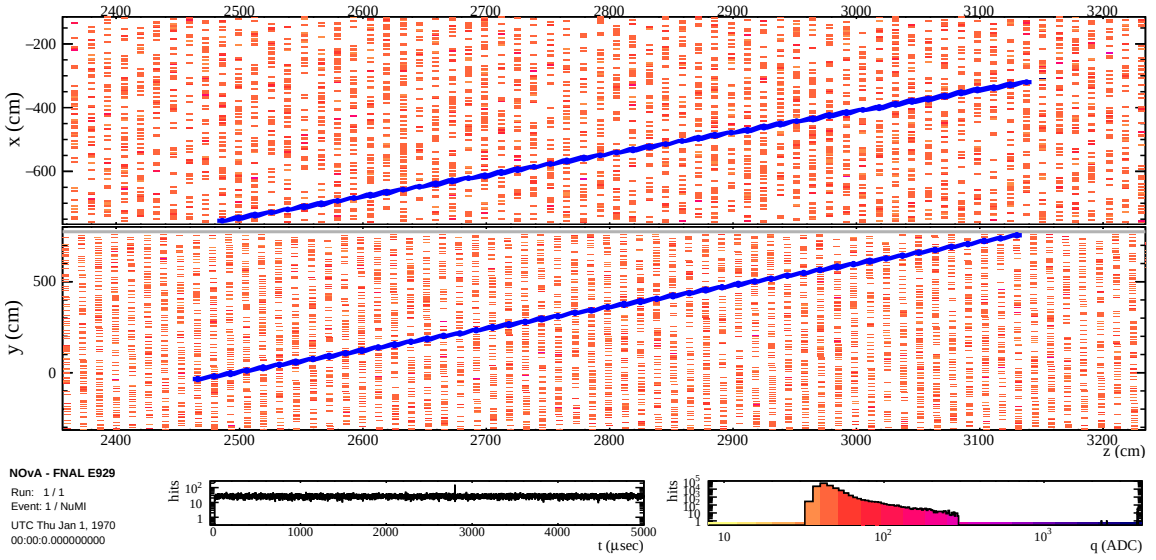

(b)

Figure 5.1: Illustration of how the offline monopole track reconstruction finds hits associated with a simulated monopole. A simulated monopole ($\beta = 0.1$) track overlaid with simulated noise hits is shown in (a). All the hits associated with the reconstructed track are highlighted in blue as shown in (b).

5.1 Monopole Track Trajectory Reconstruction

We require at least 3 hits (the minimum requirement to perform a linear fit) in the slice in both the X and Y views, otherwise the tracking process is terminated and we

move to the next available slice. A linear fit to the X view or Y view trajectory is performed using all the hits in the space-time slice in each view separately. Each fit produces what we call a two-dimensional (2D) track. In the fit each hit is weighted by its DCS value. After the initial fit we remove hits in the slice which are further than 14 cm (the grid diagonal distance in one view[1]) away from the fitted line of the 2D track in each view. In addition to this requirement, we also require that the attached hits be within $4\sigma_T$ (standard deviation of the hit times in the slice) of the average time of the slice. This cut is very useful in getting rid of electronic noise hits in the data, discussed in detail in the next chapter.

Once the hits attached to the 2D tracks are determined, we perform space-matching and time-matching tests (similar to that the used in the fast monopole trigger discussed in Chapter 4) to determine whether the two reconstructed 2D tracks are correlated in both time and space. If so, we then perform a linear interpolation to get the W position (the longitudinal position of a hit in a cell) of each hit using the fitted information of the corresponding 2D track in the other view. For example, the fitted 2D track in the X view provides the x coordinates for a given z position, in particular the x position of the hits in the corresponding Y view cells. For each cell hit associated with the tracks, there is a reconstructed 3D trajectory point (with coordinate (x_i, y_i, z_i, t_i)). Figure 5.1 illustrates how this picks out the hits associated with a simulated monopole ($\beta = 0.1$) event among overlaid noise hits. How this track reconstruction algorithm works on cosmic muon tracks in the data is illustrated in Fig. 5.2.

[1]The distance between two adjacent cells in a plane is $\delta C = 3.9$ cm, and the distance between two adjacent planes in the same view is $\delta P = 13.2$ cm. The grid diagonal distance is defined as $\sqrt{(\delta C^2 + \delta P^2)}$.

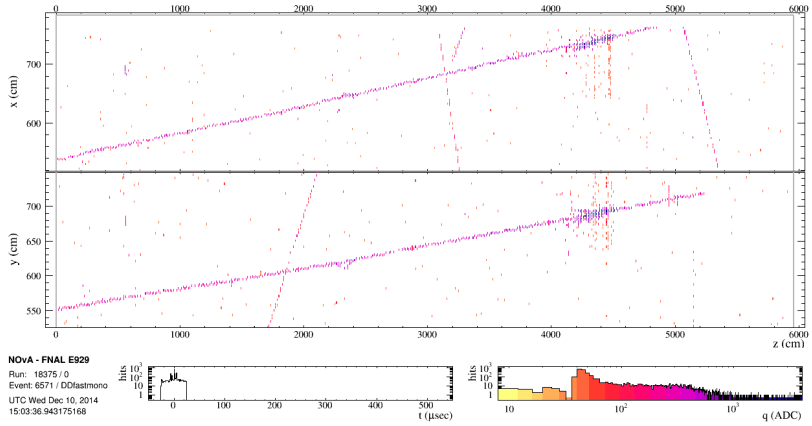

(a)

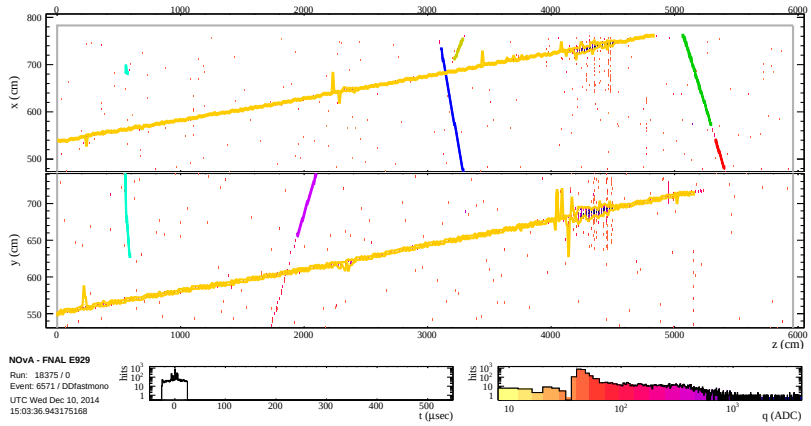

(b)

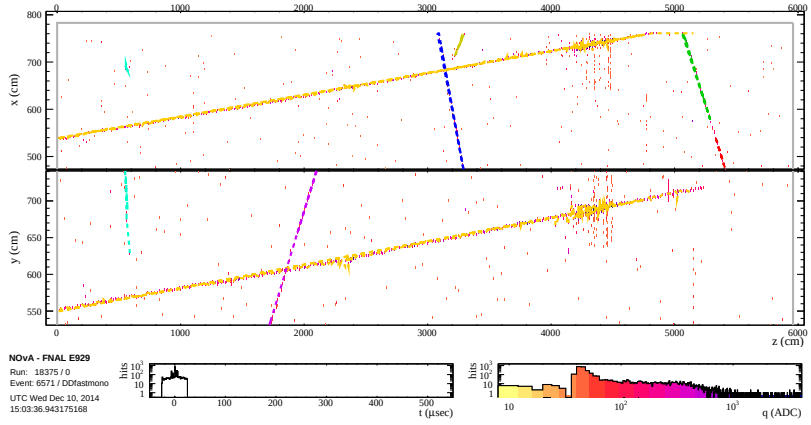

(c)

Figure 5.2: Illustration of how the offline monopole track reconstruction algorithm reconstructs a cosmic track with a high-energy deposit: The raw data of a long cosmic track event is shown in (a). The hits correlated with the slice are grouped together are shown in yellow in (b). The points corresponding to each hit associated with the track are shown in yellow in (c). Note that we have zoomed in to better show the hits associated with the slice and tracks; not all of the X and Y cells are shown.

Each trajectory point provides crucial information for further calibration of its associated hit, including the distance of the hit to the readout end (W position) which allows the corrected photoelectron number to be determined (and hence calibrated energy) and the hit residual time. In the following section, we explain how we reconstruct the velocity of the 3D track, based on the information of the 3D trajectory points.

5.2 Monopole Velocity Reconstruction

The velocity reconstruction determines the magnitude and the direction of the monopole velocity. Given a group of 3D track points with space and time information, we first sort them by their z coordinates. The coordinates (x_i, y_i, z_i, t_i) denote the space and time information of the ith cell hit along the track, and (x_0, y_0, z_0, t_0) is the space-time information of the cell hit with the lowest z value. The distance between the two is $l_i = ((x_i - x_0)^2 + (y_i - y_0)^2 + (z_i - z_0)^2)^{\frac{1}{2}}$. Then we define:

$$\chi_T^2 = \overline{(t_i - T_0 - l_i/v)^2}\,, \tag{5.1}$$

where v is the velocity and T_0 is the hit time of the first cell. Minimizing χ_T^2 gives the best fit velocity magnitude v and hit time T_0, which can be calculated analytically:

$$v = \left((\sum_i l_i)^2 - N\sum_i l_i^2\right) / \left(\sum_i t_i \sum_i l_i - N\sum_i l_i t_i\right), \tag{5.2a}$$

$$T_0 = \overline{t_i} - \overline{l_i}/v\,, \tag{5.2b}$$

where N is the total number of 3D track points involved in the fit, and $|v|$ is constrained to lie within the range [0.003,30] cm/ns ($\beta \in [10^{-4}, 1]$). Figure 5.3 shows an example of reconstructing the velocity of a typical Monte Carlo monopole track ($\beta = 0.045$) based on its track information. The direction of the velocity is indi-

cated by the sign of v, i.e., a negative v indicates the track is going in the negative z direction, and vice-versa for positive v values.

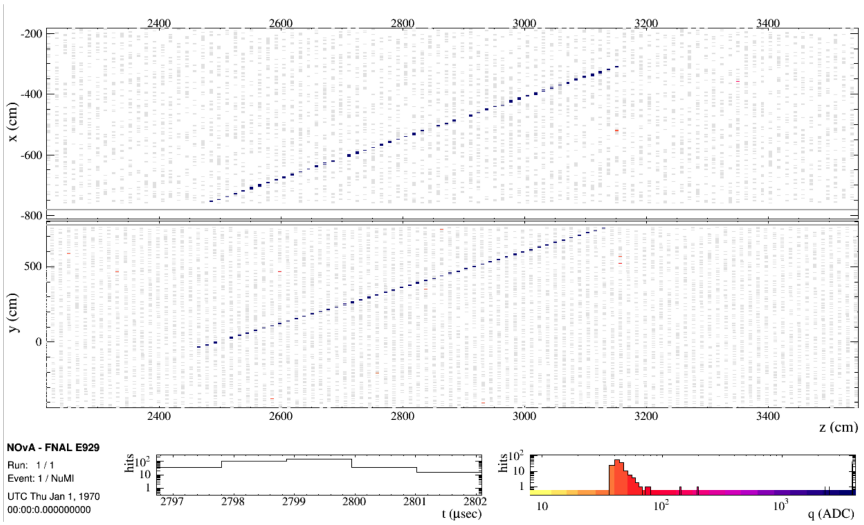

(a)

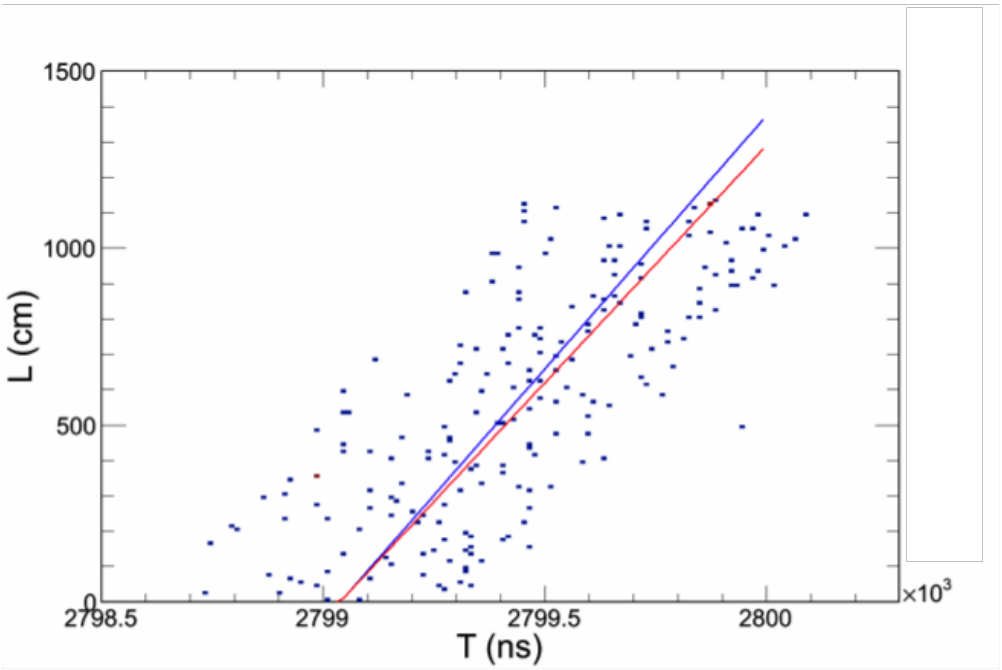

(b)

Figure 5.3: Example of reconstructing a Monte Carlo monopole velocity. (a) The event display of the reconstructed Monte Carlo monopole ($\beta = 0.045$) track. Hits not associated with the reconstructed track have been dimmed. (b) A scatterplot of the distance vs. time of the reconstructed track points shown in (a). The slope of the red line corresponds to the true velocity of 1.34 cm/ns, and the slope of the blue line corresponds to the best fit velocity of 1.43 cm/ns.

The spatial resolution of a trajectory point is determined by the size of a cell. The uncertainty in the hit time is provided by the official calibration module based on the fit to the cell hit time response (discussed in Chapter 2). The statistical uncertainty of the fitted velocity is determined by the following procedure: the velocity is fitted for 100 times; each time every track point is randomly varied using the parameters given by Table 5.1. Each time we obtain a different best-fit velocity. The standard error of the 100 best-fit values is used as the statistical uncertainty of the reconstructed velocity.

Table 5.1: Uncertainties in the reconstructed trajectory points.

Coordinate	Variation Type	Variation Value	Description
X	Uniform	1.8 cm	Cell half-width
Y	Uniform	1.8 cm	Cell half-width
Z	Uniform	2.82 cm	Cell half-length
T	Gaussian	Obtained from hit response fit	Time resolution of the hit

As discussed in Chapter 2, if a hit is saturated, the residual time and pulse-height fit fails due to lack of effective sampling points. Hence, there are two types of hits that need to be considered for each track: saturated hits, where the ADC is pinned to its maximum value, and non-saturated hits. In the former case both time and energy information is not well determined. In particular, saturated hits tend to have earlier times.[2] This is illustrated in Fig. 5.4, which gives the difference between the mean time of saturated hits and non-saturated hits for those tracks that have hits of both types. The data come from reconstructed tracks recorded by the fast monopole trigger in a total live time of 185.9 hours (the data set used for background studies which will be discussed in the following chapter).

[2]When a front-end response curve fails the fit due to saturation, the earliest sample point that caused the trigger is read out.

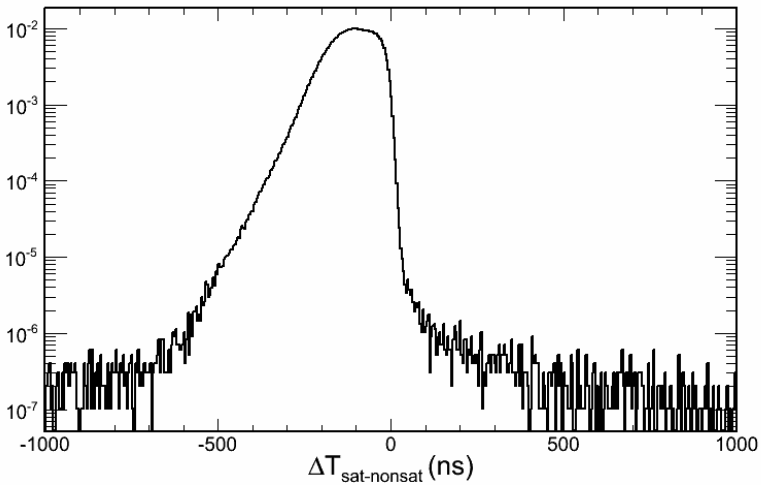

Figure 5.4: The difference ($\Delta T_{sat-nonsat}$) between average time of all saturated hits and non-saturated hits associated with the same reconstructed tracks of data recorded by the fast monopole trigger.

To avoid a systematic uncertainty introduced by this offset, we separate saturated hits and non-saturated hits associated with a same track into two groups. The velocity reconstruction is done separately for both groups as long as either group has at least 3 hits. If one group has less than 3 hits, the reconstructed velocity is obtained from the other group. The velocity fitted from saturated hits tends to have worse resolution for obvious reasons. We compare the reconstructed velocity with the true velocity of simulated monopoles in Fig. 5.5, and see a wider distribution of velocity ratios (reconstructed over the entire Monte Carlo data set) when the velocity is reconstructed by saturated hits.

If a reconstructed track contains more than two saturated hits and more than two non-saturated hits, we have two different reconstructed values of velocity. The final velocity is chosen to be the one with a smaller χ^2_T (and this is usually that reconstructed with non-saturated hits). The corresponding χ^2_T and statistical velocity uncertainty σ_v are recorded for further offline analysis.

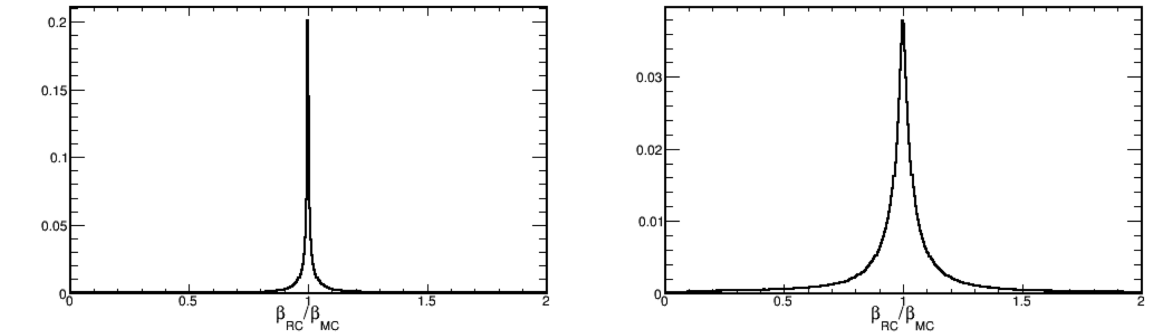

(a) (b)

Figure 5.5: Ratio of the reconstructed to the generated velocities of Monte Carlo monopoles with at least 3 saturated and 3 non saturated hits, where the velocities are reconstructed using (a) non-saturated and (b) saturated hits.

5.3 Reconstruction Validation

We have tested the track and velocity reconstruction algorithms using simulated isotropic monopoles with a velocity range of $\beta \in (10^{-4}, 0.2)$. The reconstructed quantities are compared with the MC truth information for validation. as shown in Fig. 5.6(a). For faster tracks the direction determination is worse as the transit time is shorter and more hits are saturated, as shown in Fig. 5.6(b), and the uncertainty in the angle between the reconstructed direction and the true direction becomes larger.

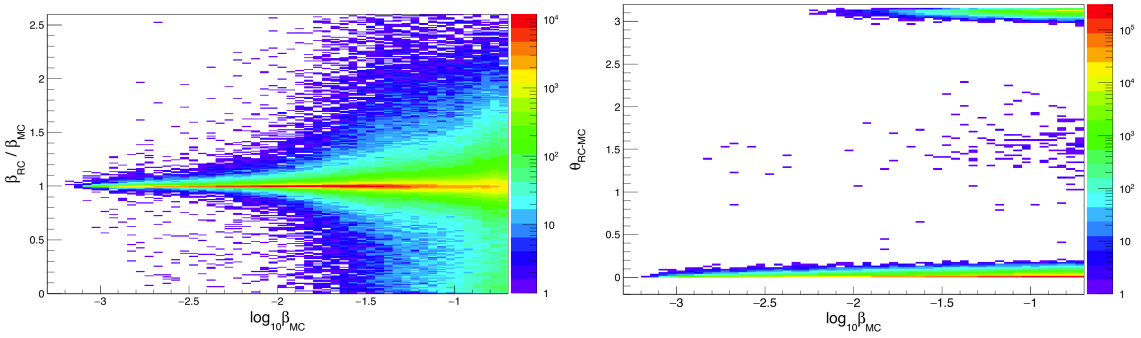

(a) (b)

Figure 5.6: Monte Carlo test of the monopole track velocity reconstruction. (a) The ratio of the reconstructed velocity magnitude over the true velocity, as a function of the monopole true speed. (b) The angle between the true direction and the reconstructed direction of monopole tracks, as a function of the monopole true speed.

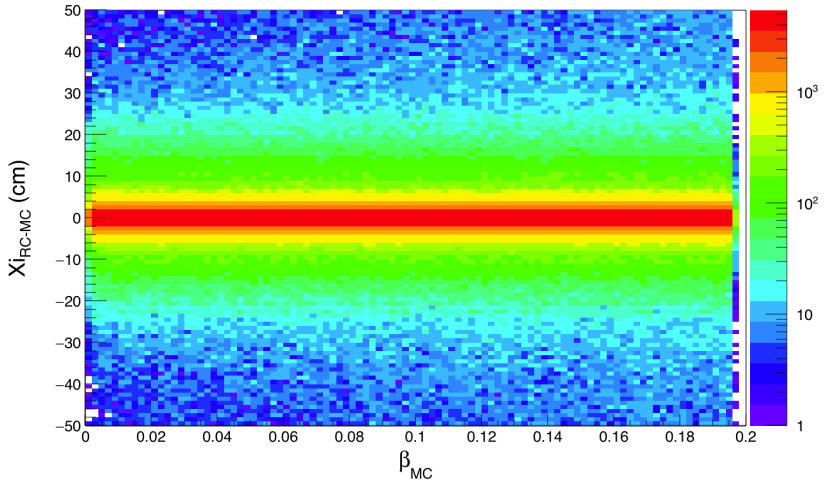

(a)

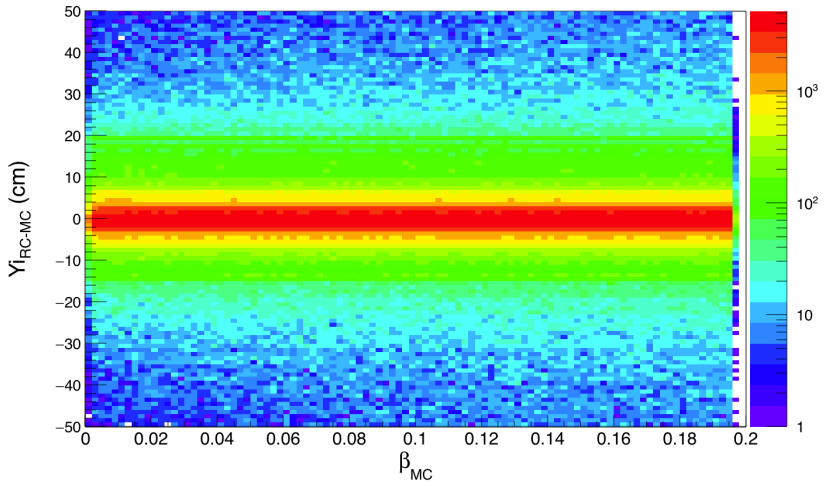

(b)

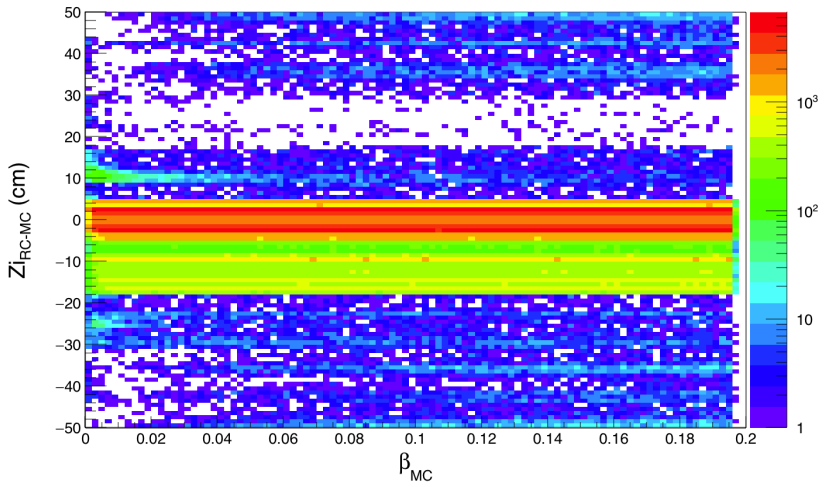

(c)

Figure 5.7: Monte Carlo test of the monopole track entry position reconstruction. The distance between the x, y, z components of the reconstructed and true entry position of the simulated monopole, is given respectively in (a), (b), and (c).

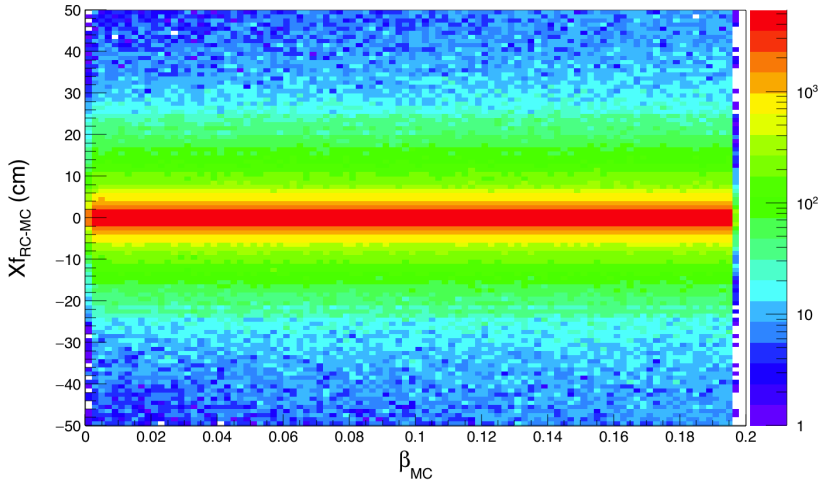

(a)

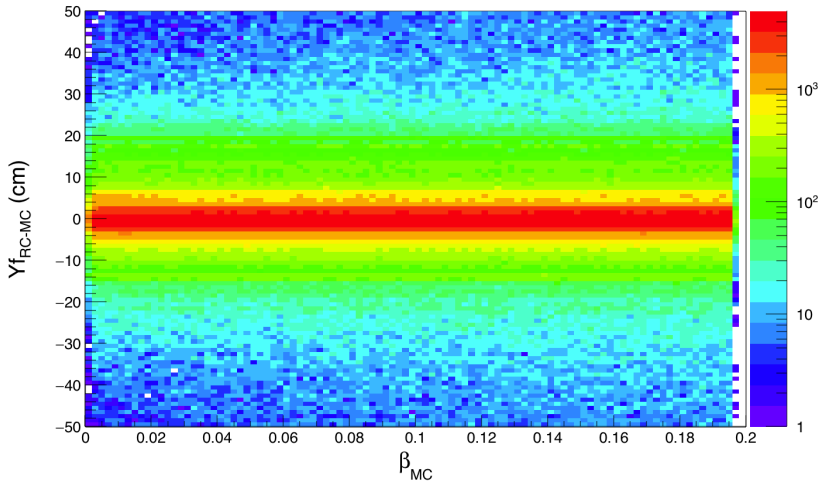

(b)

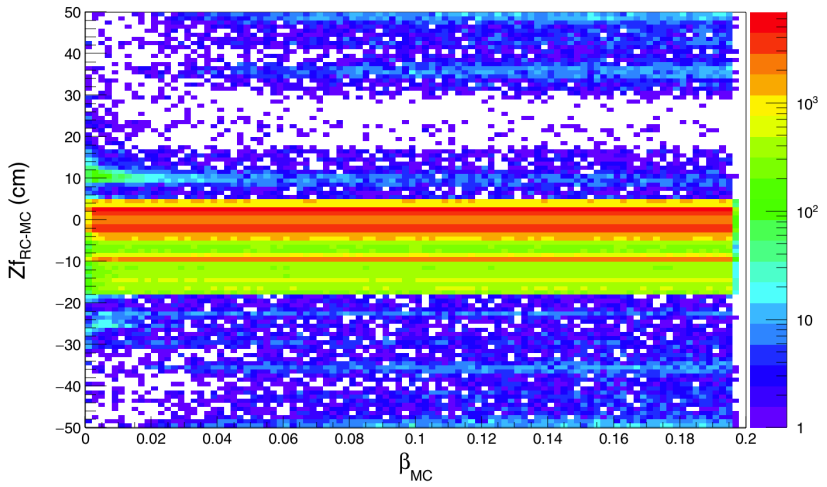

(c)

Figure 5.8: Monte Carlo test of the monopole track exit position reconstruction. The distance between the x, y, z components of the reconstructed and true exit position of the simulated monopole, is given respectively in (a), (b), and (c).

The reconstructed entry point and exit point, compared to the true positions, is shown in Figs. 5.7 and 5.8. They show little dependence on the monopole velocity and are consistent with the spatial resolution of the NOνA far detector. The offset in the Z position is mainly due to the fact that often a monopole event enters or leaves the detector it partially clips a cell, not leaving enough energy to trigger a hit.

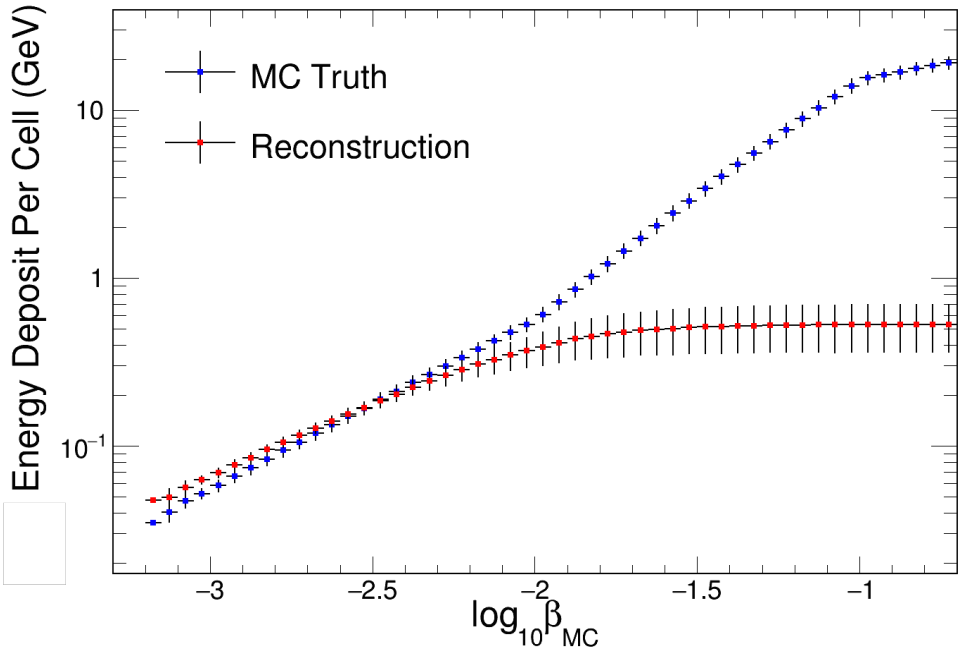

Figure 5.9: The comparison between the reconstructed and true energy deposited by a monopole in the detector as a function of the monopole true velocity. The horizontal bars represent the bin size of the velocities. The vertical bars represent the standard deviation of energy deposit per cell.

The determination of the deposited energy of a monopole inside the detector is simply the sum of the energies in each cell hit of the monopole track. Given the limited number of samples (4) recorded for each hit, we cannot determine the true energy for a saturated hit, so the reconstructed energy for a saturated hit is a lower limit. As the monopole velocities increase, the saturated hits ratio increases, and the true energy deposit becomes much larger than the reconstructed energy. This

behavior is shown in the Fig. 5.9.[3]

[3]Note that as the energy deposit increases, the Birks suppression gets more obvious, which adds to the discrepancy between the reconstructed energy deposit and the true value.

Chapter 6

Offline Data Analysis

The installation of the instrumentation in the far detector was completed at the end of 2014. We selected the far detector data recorded by the fast monopole trigger from December 4[1] to December 12 in 2014 to be the data set used to tune and test the monopole identification criteria and to investigate backgrounds. This unblinded data set has a total live time of 185.9 hours, and is called the background data set. The monopole identification criteria were determined by the Monte Carlo signal data set discussed in Chapter 3 (simulated monopoles with a uniformly random velocity $\beta \in (10^{-4}, 0.2)$). Finally, the identification criteria were then applied to a three-month data set collected by the fast monopole trigger from December 12th, 2014 to March 16th, 2015, using strict blind analysis rules.

6.1 Data Selection and Live Time Calculation

Minimum-bias cosmic data are used to calibrate the far detector and to identify bad subruns. A standard set of data quality criteria [48] are used to validate the data collected. The data collected by the fast monopole trigger and used for this analysis

[1]This was the date when the data-driven triggers were implemented with a configuration identical to the current data readout mode discussed in Chapter 2, and when we started taking data with the fully instrumented detector.

uses only those subruns that pass the data quality criteria.

Here is the list of criteria used for the data selection:

- **Minimum Stats** – If the duration of the minimum-bias data taken by the pulser trigger in a subrun is less than 1 second, the subrun is not considered.
- **Median MIP Hit Rate per Cell** – A minimum-ionizing particle (MIP) hit, typically from a muon, has a DCS value within the ADC range [175,3200]. We require a good subrun [48] to have the median MIP hit rate per cell to be within the range (13 Hz, 23 Hz). The cut is chosen based on Fig. 6.1.

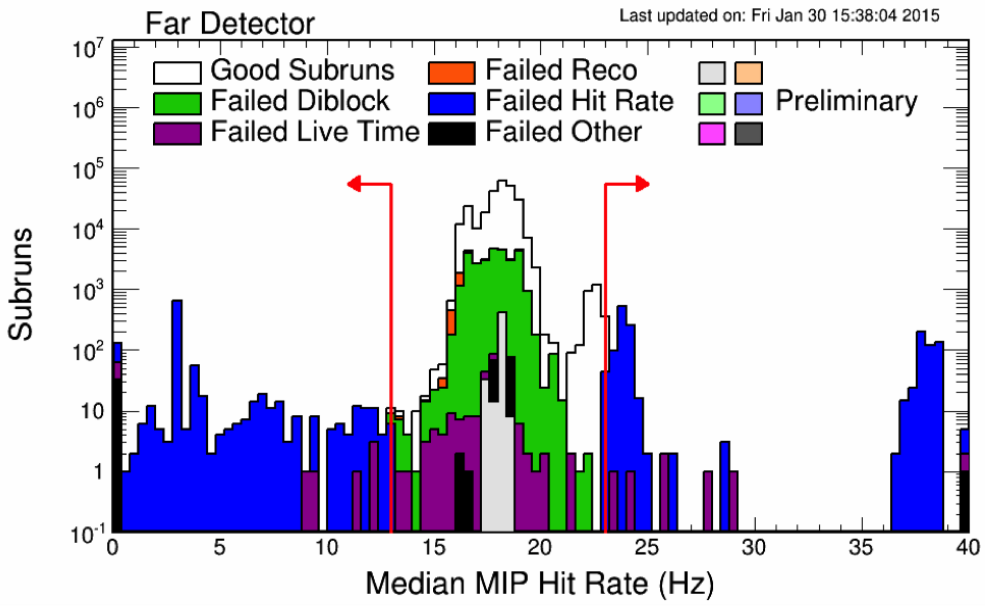

Figure 6.1: Typical distribution of the median MIP hit rate per cell per subrun. Subruns in the region where the red arrows point to fail the data quality cuts.

- **Slices per Subrun** – We require the number of slices per 10^4 channels in a subrun to be within the range (1.2,3.2), as illustrated in Fig. 6.2.
- **2D Only Track Fraction** – There are some 2D tracks that cannot be further reconstructed to 3D tracks due to lack of information in the other view. We require the fraction of these 2D tracks less than 15%, as illustrated in Fig. 6.3.

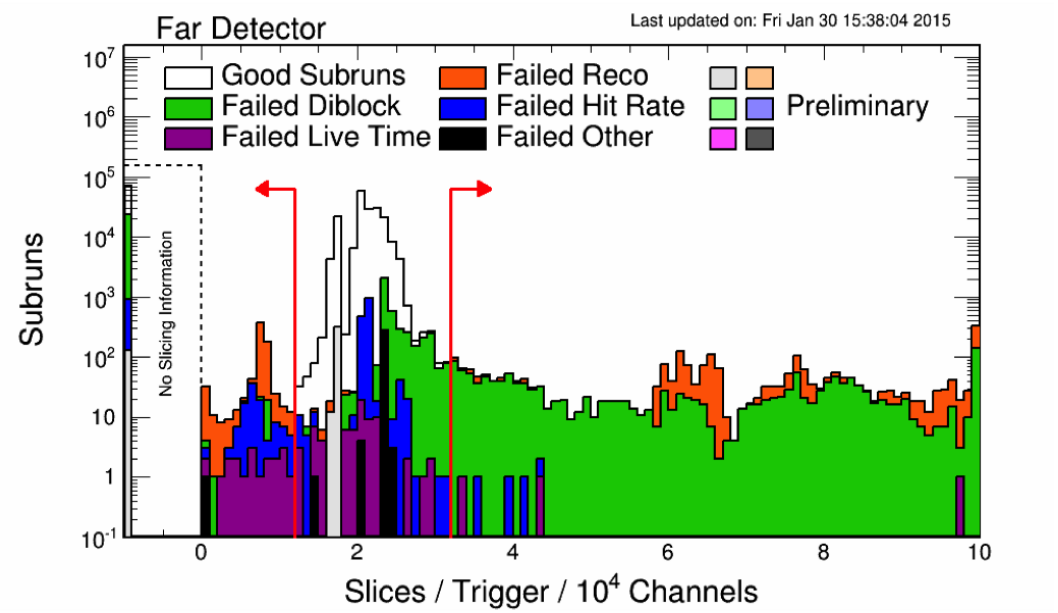

Figure 6.2: Typical distribution of the slices per subrun. Subruns in the region where the red arrows point to fail the data quality cuts. Trigger here stands for the pulser trigger which collects minimum-bias data.

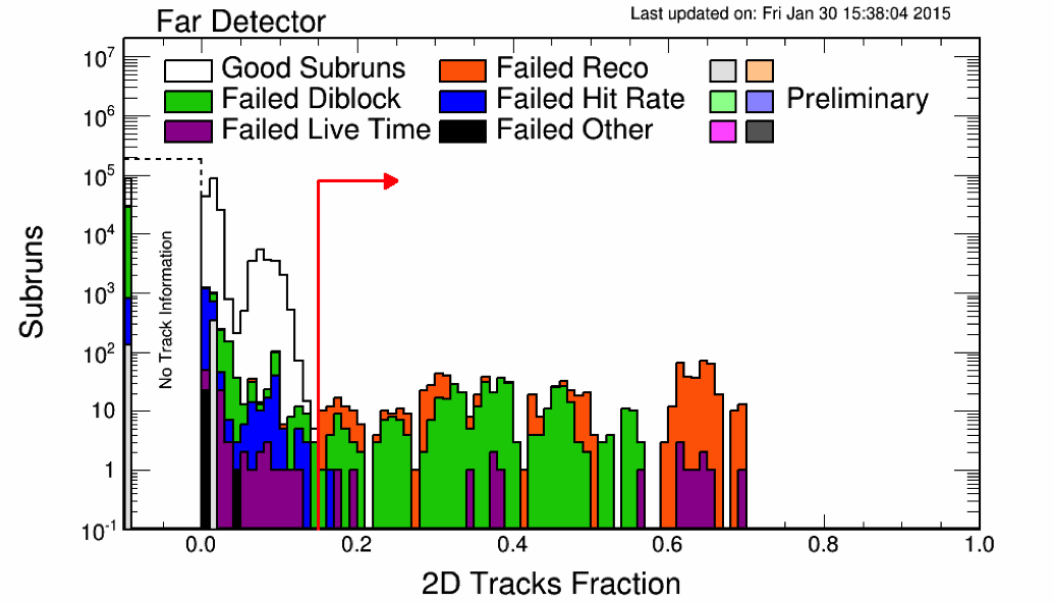

Figure 6.3: Typical distribution of the 2D only track fraction per subrun. Subruns in the region where the red arrow points to fail the data quality cuts.

In addition to these data quality cuts, we also require that the data were taken by a fully instrumented far detector, defined as having more than 99.8% active channels. This cut removes 1.1% of the subruns which have passed the data quality cuts. As shown in Fig. 6.4, the subruns that pass the data quality cuts and taken by a fully instrumented detector have a very constrained fraction of active channels within [99.85%,99.95%].

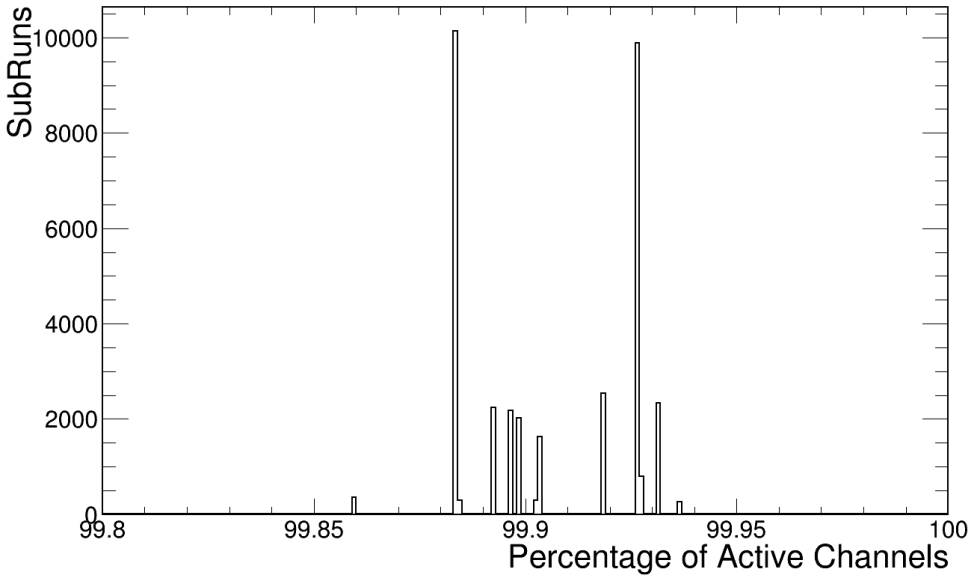

Figure 6.4: The fraction of active channels for those subruns that passed the data quality cuts and have more than 99.8% active channels.

If the total time of every trigger decision is beyond the allowed DAQ time on a milliblock, the entire milliblock is dropped. Each buffer node records the number of milliblocks processed and dropped. By counting the fraction of dropped milliblocks among the milliblocks read out, we can calculate the trigger live time. During the data taking period, we had a varying number of buffer nodes (40-50) in the DAQ, and different configurations for various triggers, both of which influenced the execution time of all the trigger decisions and hence the live time. The recorded live time fraction in one of the buffer node is shown in Fig. 6.5. The overall live time fraction is

calculated by counting the fraction of dropped milliblocks in each buffer node during the data taking period. The total live time fraction was 76% during the data taking period. With more and faster buffer nodes (farm-70 in Fig. 6.5 is one of faster nodes) being added to in the DAQ, the fraction of dropped milliblocks will be greatly reduced in the future.

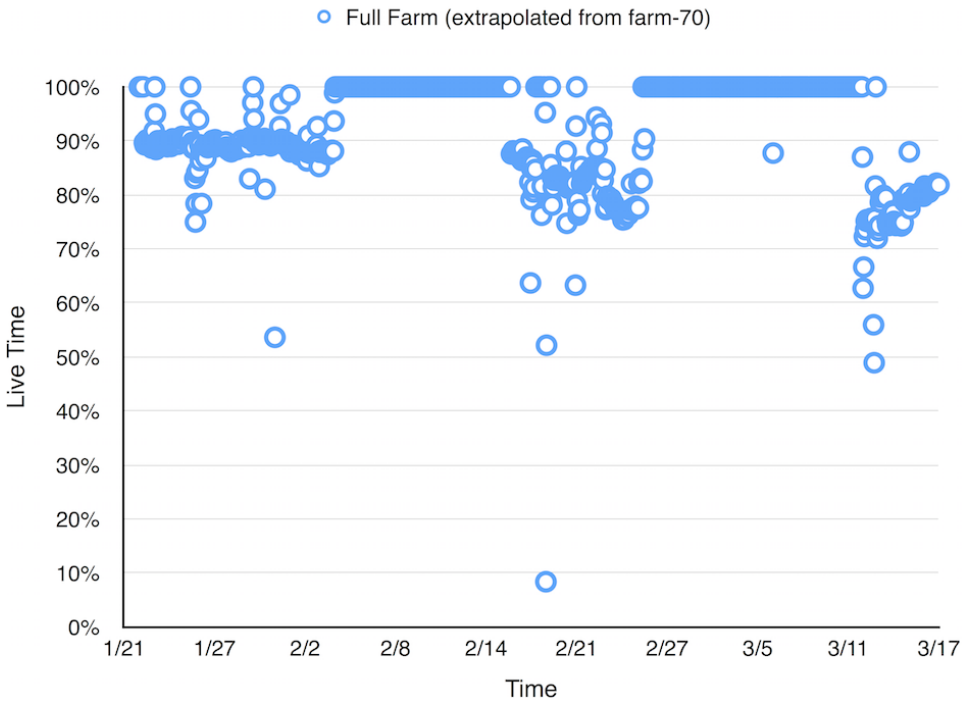

Figure 6.5: The live-time fraction from January 21 to March 16. The data is taken from one of the fastest buffer nodes (farm-70), which was implemented on January 21st, 2015.

The live time of the unblinded data set is 185.9 hours, and the three-month blinded data set has a total live time of 1628.2 hours. The fast monopole trigger rate for the blinded and unblinded data sets has been calculated, corrected for the live-time, over all the buffer nodes, as shown in Fig. 6.6. It has a mean value of 21.2 Hz.

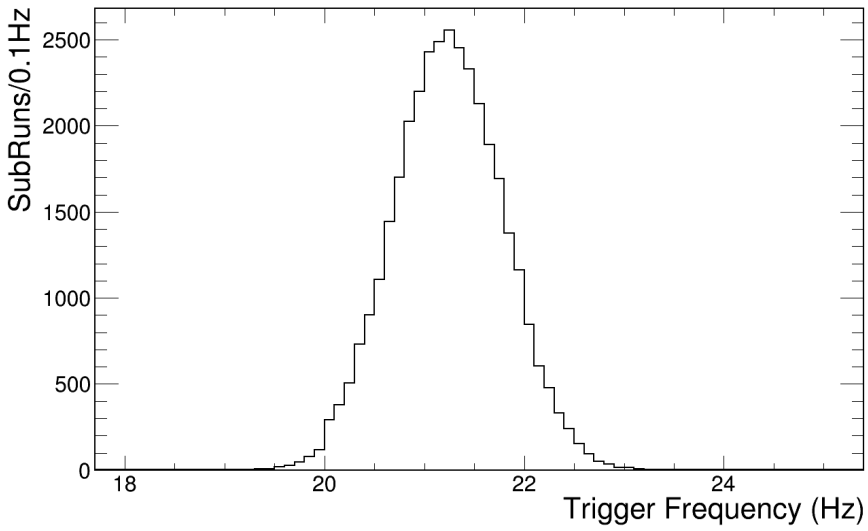

Figure 6.6: The fast monopole trigger rate with live time correction.

6.2 Preselection Cuts

Most of the background tracks and fake reconstructed tracks can be rejected with simple cuts. These are applied before further analysis. The series of cuts are described below. In the plots below by signal we mean the monopole MC data set and the background we mean the unblinded data set. The MC data set includes monopoles with uniform velocity distribution $\beta \in (10^{-4}, 0.2)$. During the data taking period, some (around 0.64%) channels are triggered at a extremely high rate ($\log_{10}$(HitRate)>3.5) or unusually low rate ($\log_{10}$(HitRate)<0.5). These channels are tagged as bad channels that are masked off in the offline analysis. Note that the channels masked off may vary slightly for different runs. In the MC we have applied the bad channel mask which is properly weighted for the data taking period.

6.2.1 Cut 1: Saturated Hits Number

Reconstructed tracks without a single saturated hit are rejected. The probability of a monopole hit being saturated as a function of the monopole's speed is shown in

Fig. 3.11.

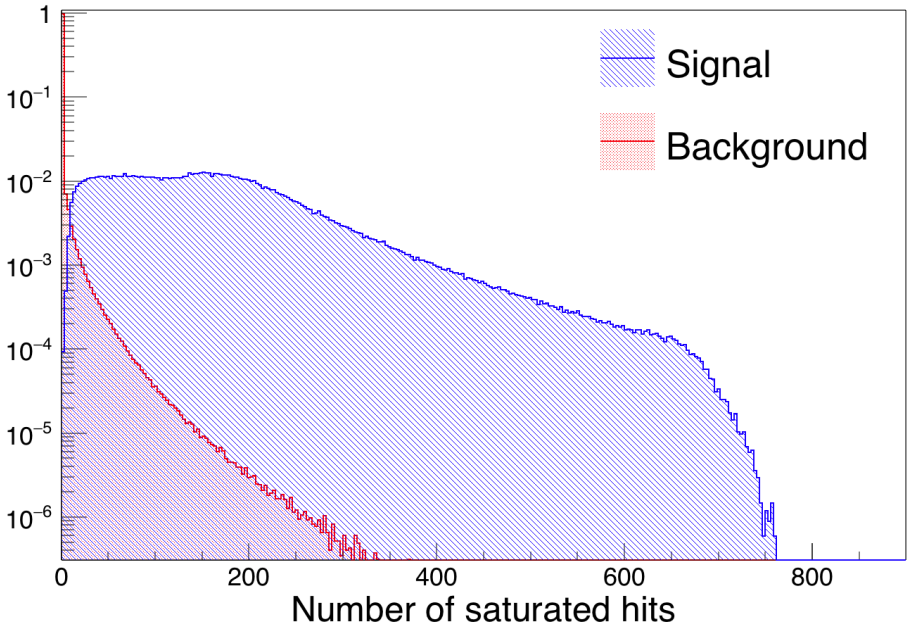

Figure 6.7: The number of saturated hits for signal (blue) and background (red) events, before any preselection cuts. Preselection cut 1 requires at least one saturated hit in the track.

6.2.2 Cut 2: Track Fatness

To get rid of the largest background, high-energy cosmic showers, we use a metric, "track fatness", to distinguish tracks from showers. When reconstructing 2D tracks in the X and Y views, we calculate the DOCA (distance of closest approach) of every hit attached to the best fit track. We define:

$$F_{L0} = \sum_i \mathrm{DOCA}^2/\mathrm{N_s}\,, \tag{6.1}$$

where $\mathrm{N_s}$ is the number of signal hits attached to the track.

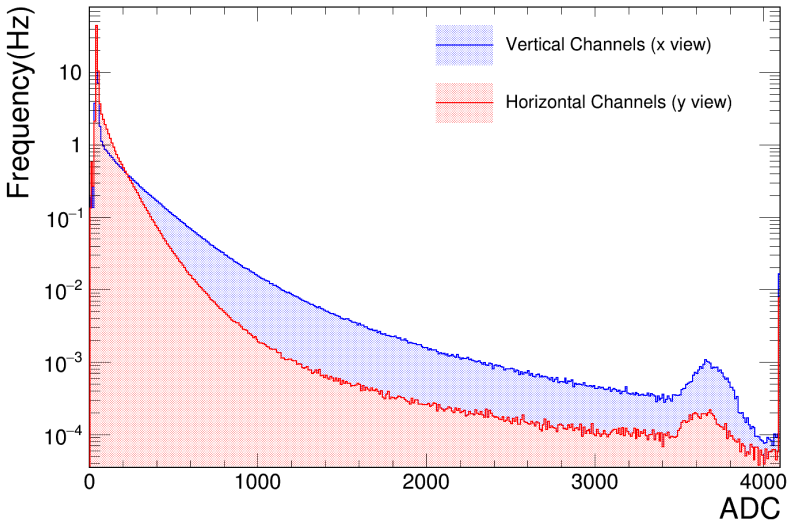

Figure 6.8: The DCS spectrum of X view (blue) and Y view (red) events of a 2-second minimum-bias data set. The peaks at high ADC values correspond to saturated hits. The data used here passed the data quality cuts.

The number of additional noise and background hits attached to a monopole track is estimated using:

$$\mathrm{N_b} = f \cdot dT \cdot dV/V\,, \tag{6.2}$$

where f corresponds to the frequency of those hits in either the X view or Y view with DCS values larger than 500 ADC, dT is the track time window, V is the entire far detector volume, and dV is the fiducial volume of the reconstructed track given by:

$$dV = \pi L r^2\,, \tag{6.3}$$

where L is the reconstructed track length and $r = 14$ cm (the maximum DOCA cut used to attach hits to a 2D track). Assuming the $\mathrm{N_b}$ noise and background hits are uniformly distributed, their average DOCA^2 value is:

$$\int_0^r \frac{2\pi x}{\pi r^2} x^2 dx = r^2/2\,. \tag{6.4}$$

The corrected fatness of the track, including the contribution of noise and background hits is:

$$F_L = \frac{Ns \cdot F_{L0} + \mathrm{N_b} \cdot r^2/2}{\mathrm{N_s} + \mathrm{N_b}}\,, \tag{6.5}$$

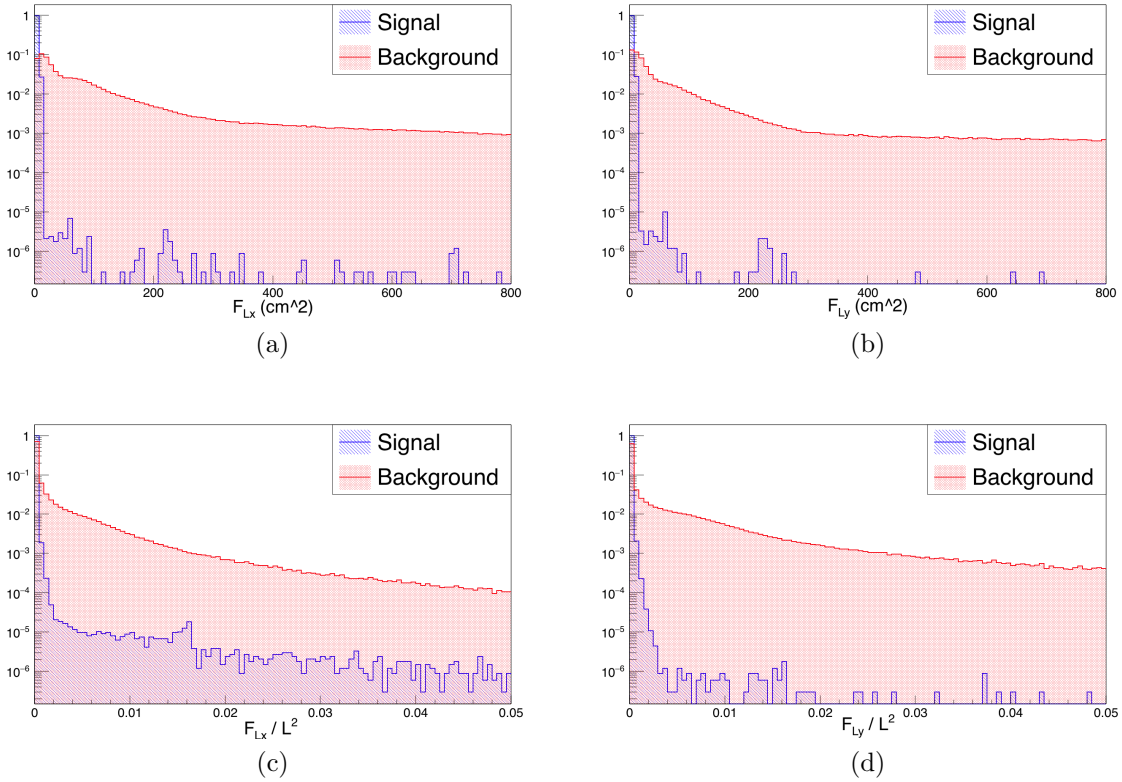

Figure 6.9: The distribution (after preselection cut 1) of track fatness F_L in the (a) X view and the (b) Y view, as well as the distribution of fractional track fatness F_L/L^2 (where L is the reconstructed track length) in the (c) X view and the (d) Y view. The track fatness cuts reject track with $F_L > 15$ cm^2 or $F_L/L^2 > 0.001$ in either the X or Y views.

For a conservative estimate (over estimating the fatness of signal tracks), the value f is determined using the DCS spectrum of X view and Y view hits from minimum-bias data that passed the data quality criteria, shown in Fig. 6.8. We obtain $f_x = 6.74\times10^5$ Hz, and $f_y = 1.31\times10^5$ Hz. Note that the total number of X view hits and the number of Y view hits are about equal. However vertical (X view) channels tend to have larger energy deposit than horizontal (Y view) channels due to the angular distribution of

cosmic rays and the fact that there is more activity near the top of the detector. This is reflected in the corrected fatness distribution of signal tracks shown in Fig. 6.9, as we see more "fatter" tracks in the X view than in the Y view.[2] We place a fatness cut F_L on both views based on its absolute value and relative value F_L/L^2 to reject tracks with $F_L > 15$ cm^2 or $F_L > 0.001$, where L corresponds to the reconstructed track length.

6.2.3 Cut 3: Velocity Validation

As mentioned in Chapter 5, the sign of the final reconstructed velocity indicates the direction of the track: a positive velocity value corresponds to a positive z direction, and vice-versa for a negative velocity. We calculate the distance between the reconstructed entry (exit) hit position to the earliest (latest) hit position in the reconstructed track. The distance should be within the propagated uncertainty upper limit in spatial resolution:

$$|\sigma_v|(T_{max} - T_{min}) + \sigma_t|v| + 14 \text{ cm}\,, \tag{6.6}$$

where σ_v is the statistical reconstructed velocity uncertainty, T_{max} (T_{min}) is the latest (earliest) hit time of the track, σ_t is the standard deviation of the times of all the hits attached to the track, and 14 cm is the maximum DOCA cut used to attach hits to a track. If a reconstructed track fails this cut, it indicates the uncertainty of the reconstructed velocity has been underestimated, or this track contains some hits with badly measured times and σ_t is underestimated.

The final reconstructed velocity is either based on the group of saturated hits or the non-saturated hits in the track, with a corresponding value of $\sqrt{\chi^2_T}$ of the chosen

[2]We are working on overlaying real minimum-bias data with the MC monopoles, so this conservative evaluation will no longer be needed for future analysis.

group of hits. We compare the value of $\sqrt{\chi^2_T}$ with the standard deviation of the times of the chosen group of hits. A larger value of $\sqrt{\chi^2_T}/\sigma_T$ indicates the velocity reconstruction is not valid. We choose the upper limit of $\sqrt{\chi^2_T}/\sigma_T$ to be

$$\sqrt{\chi^2_T}/\sigma_T < 0.4\,. \tag{6.7}$$

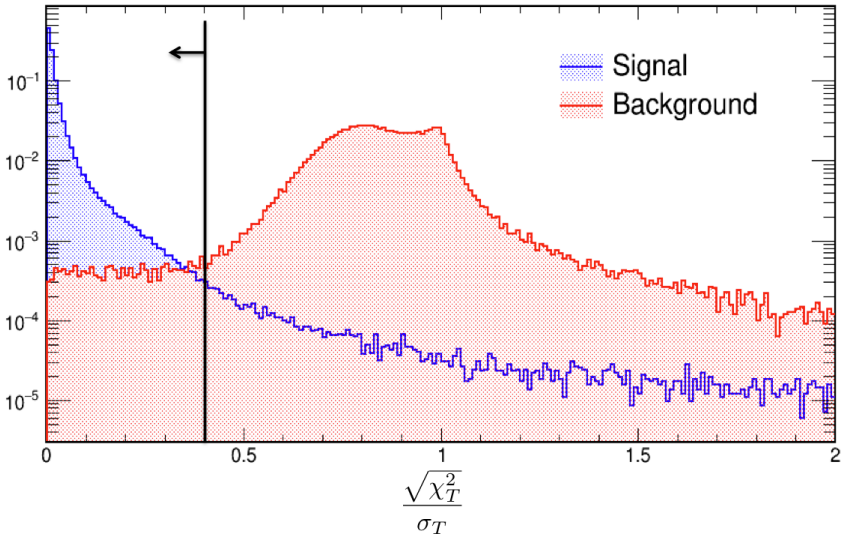

Figure 6.10: The $\sqrt{\chi^2_T}/\sigma_T$ distribution of signal (blue) and background (red) reconstructed tracks, after preselection cuts 1 and 2. The velocity validation cuts require the value of $\sqrt{\chi^2_T}/\sigma_T$ to be less than 0.4 (black arrow).

We also require the statistical reconstructed velocity uncertainty to be less than 10% of the magnitude of the reconstructed velocity. Figure 6.11 shows that background events tend to have a larger statistical uncertainty in the reconstructed velocity.

If a track contains more than two saturated hits and more than two non-saturated hits, we have two values of the reconstructed velocity, one based on saturated hits (β_{sat}) and the other based on non-saturated hits (β_{nonsat}). We introduce a consistency check by requiring the ratio $\beta_{sat}/\beta_{nonsat}$ be between 0.4 and 2.5. This cut gets rid of many background events due to their inconsistent reconstructed velocities, as shown

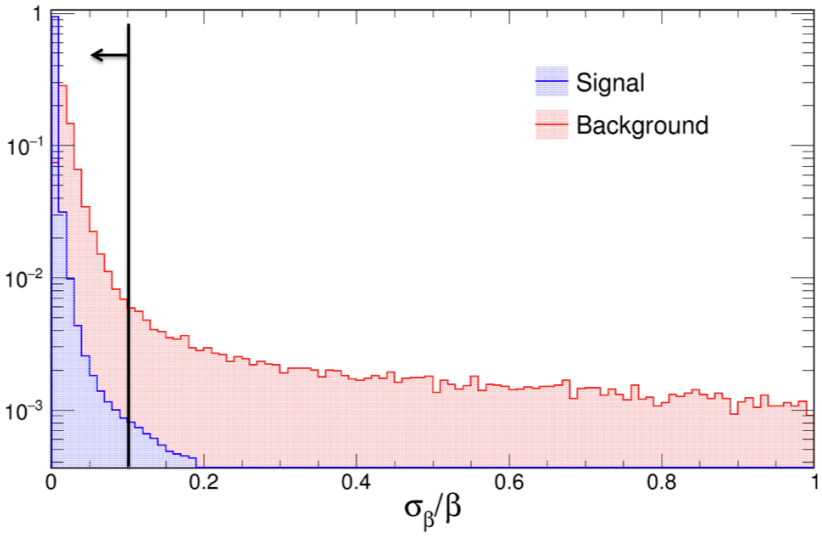

Figure 6.11: The statistical relative velocity uncertainty distribution of signal (blue) and background (red) events, after preselection cuts 1 and 2. The velocity validation cuts require the relative velocity uncertainty σ_β/β to be less than 0.1 (black arrow).

in Fig. 6.12.

In Chapter 5, we mentioned that the fitted velocity magnitude is constrained within the range [10^{-4},1]. If the velocity obtained via Eq. 5.2 is larger than 1 or smaller than -1, it is set to 1 or -1 respectively. Most of the cosmic-ray tracks in the real data are traveling at the speed of light, which is why there are two peaks in the velocity ratio of the background data set in Fig 6.12. We cannot resolve the directionality for most of these relativistic tracks, which is why the peaks are at about the same height.

As we mentioned in Chapter 2 and show in Fig. 5.5, saturated hits have a larger uncertainty in the hit time. The background tracks are mainly high-energy muons and their saturated hits are usually close together, where the bremsstrahlung radiation takes place. Hence, the fit velocity based on the saturated hits for such events is likely to be underestimated. This explains why there is a peak at zero in the spectrum of the background data set in Fig. 6.12. For MC monopole events, the saturated hits are

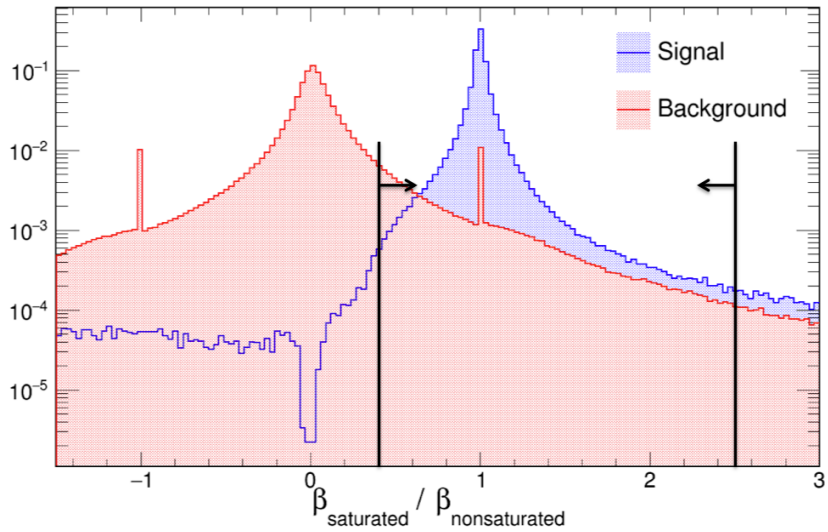

Figure 6.12: The $\beta_{sat}/\beta_{nonsat}$ distribution of signal (blue) and background (red) events after after preselection cuts 1 and 2. The consistency check of the velocity validation cuts requires the value of $\beta_{sat}/\beta_{nonsat}$ to be within (0.4,2.5) (black arrows).

uniformly distributed along the track, thus well separated in space and time which leads to a more precise fit velocity. This is why we see a dip in the signal spectrum in Fig. 6.12.

After the track fatness cuts the majority of remaining background tracks are high-energy muons with $\beta = 1$, as shown in Fig. 6.13. We cut out all tracks with $\beta > 0.8$, since the detector cannot distinguish well a high-energy muon from a relativistic monopole.

6.2.4 Cut 4: Bremsstrahlung Rejection

As we have just mentioned, the energy deposit of a high-energy cosmic muon (one of the major background sources) is concentrated where the bremsstrahlung radiation takes place, as shown in Fig. 6.14.

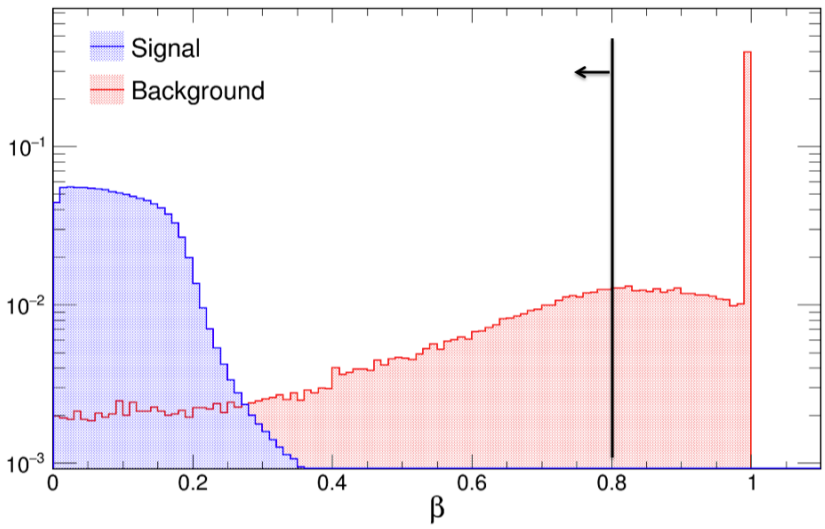

Figure 6.13: The reconstructed β distribution of signal (blue) and background (red) events after preselection cuts 1 and 2. The tracks with velocity larger than $0.8c$ are rejected (black arrow).

The total power dissipated in bremsstrahlung radiation of a magnetic monopole with speed β and deceleration $\dot{\beta}$ is given by:[3]

$$P = \frac{2g^2}{3c}\gamma^6[\dot{\beta}^2 - (\vec{\beta} \times \dot{\vec{\beta}})^2], \tag{6.8}$$

where g is the magnetic charge of the monopole and $\gamma = (1-\beta^2)^{-\frac{1}{2}}$. Due to the large mass of the monopole, the deceleration is negligible ($\dot{\beta} \sim 0$), and there is effectively no bremsstrahlung radiation in our simulation of monopoles. Hence, the energy deposit of monopoles is generally quite uniform along its trajectory.

To distinguish monopole tracks from high-energy cosmic muons that produce bremsstrahlung radiation, we define δ to be the distance between the geometric center and the energy-weighted center position of a track, divided by the reconstructed track length. For a track with a completely uniform energy deposit, δ is 0. Figure 6.15

[3]This is an analogy to the Lienard result (1898), with the electric charge e replaced by the magnetic charge g. The derivation is given in Jackson's *Classical Electrodynamics*.

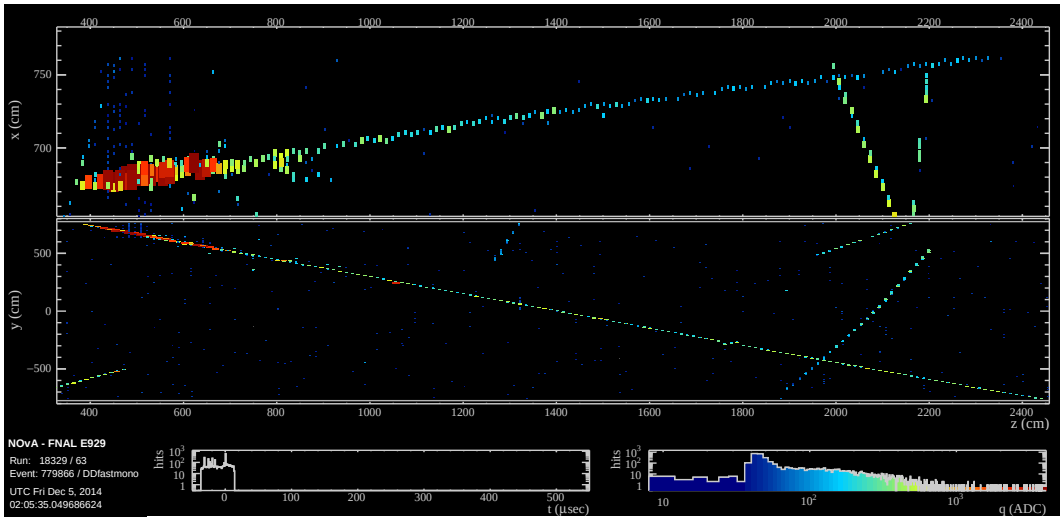

Figure 6.14: The event display of a high-energy muon with bremsstrahlung radiation. The hit size is proportional to the energy deposit. The event display is zoomed in on the region which contains the muon track, and note that the X view range (top) is smaller than the Y view range (bottom).

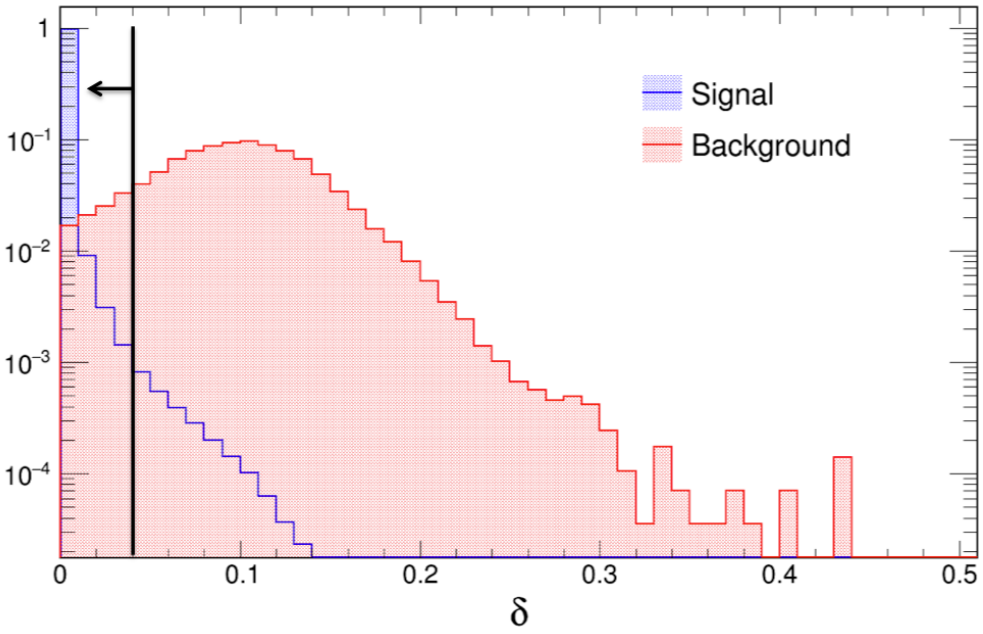

Figure 6.15: The reconstructed δ of signal (blue) and background (red) events after preselection cuts 1 through 3. The bremsstrahlung rejection cut requires the value of δ to be smaller than 0.04 (black arrow).

shows δ for both signal and background events after preselection cuts 1 through 3. We observe a bump at $\delta = 0.1$, and set a upper limit for $\delta = 0.04$. The cosmic muon shown in Fig. 6.14 is a typical cosmic track that passes all the preselection cuts but the bremsstrahlung rejection cut. This track is 14.7 meters long and penetrates the detector. The energy weighted center is 2.16 meters away from the geometric center of the track, which gives a δ value of 0.147.

6.2.5 Cut 5: Maximum Gap Cuts

Another class of background tracks is composed of those with hits from different cosmic rays that are miss-reconstructed as a single non-relativistic track, and that pass the velocity cut. We have introduced a metric to remove such tracks by measuring the gap between the segments of the reconstructed track, in terms of the number of missing planes. Ideally, a track caused by a single particle has no missing planes. And there are few channels that are dead or have been masked off. If a track contains a gap more than 5 planes or 13% of the total number of planes crossed, it is rejected by this cut.

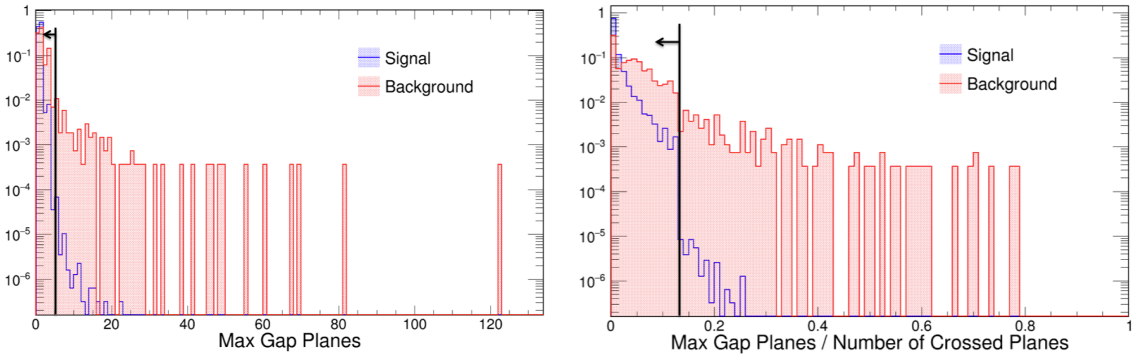

(a) (b)

Figure 6.16: The distribution of the maximum gap in the number of missing planes (a) and gap ratio (b), for signal (blue) and background (red) events after preselection cuts 1 through 4. The maximum gap cut require the maximum gap to be less than 6 planes, and the gap ratio to be no more than 13%.

6.2.6 Cut 6: Time Window for Non-relativistic Tracks

Non-relativistic reconstructed tracks should have a relatively long time between the earliest and the latest hits (time window). An additional cut only applied to $\beta < 0.3$ events, requires the time window of the track to be larger than 500 ns, which is the time between two adjacent samples of a hit. Figure 6.17 shows that a large number of background tracks with $\beta < 0.3$ have fairly small time windows. Such tracks usually have only a few number of hits, which leads to a fitted velocity with a large uncertainty. Thus we require at least 10 hits in each view with an overlapping plane number no less than 10, which ensures the reconstructed velocity is well determined. The relativistic ($\beta \geq 0.3$) reconstructed tracks that pass preselection cuts 1 through 5 skip this cut.

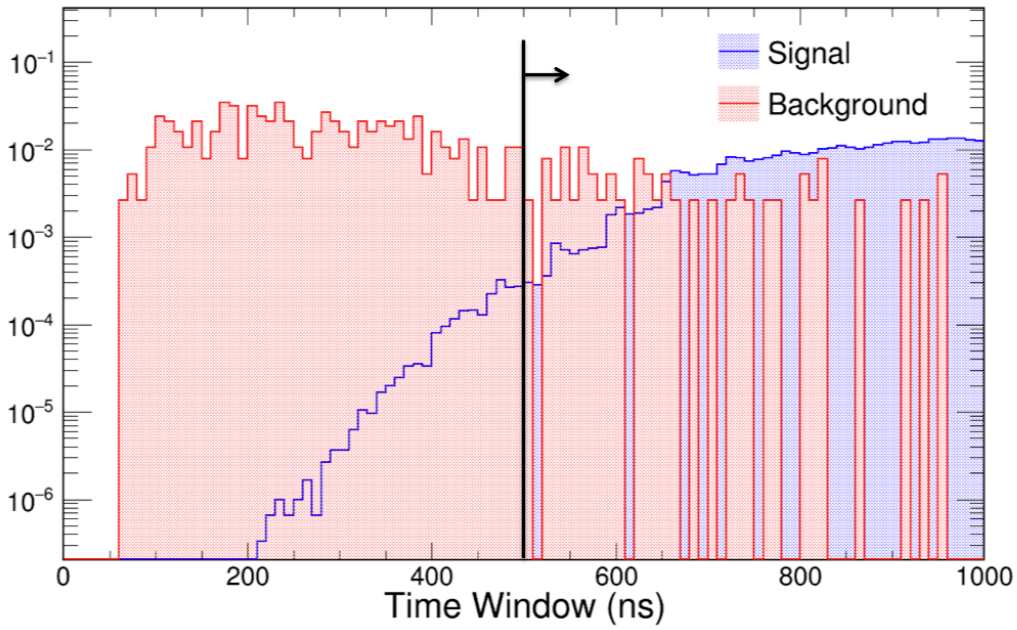

Figure 6.17: The non-relativistic ($\beta < 0.3$) track time window size of signal (blue) and background (red) events after preselection cuts 1 through 5. The cut requires the time window to be larger than 500 ns (black arrow).

6.2.7 Cut 7: Penetration

A penetration cut is applied to the fast monopole trigger, and the same cut is applied again with the reconstructed entry and exit positions. This is the last preselection cut. We reject tracks with either the entry or exit positions more than 0.5 m away from the detector surface, or whose entry and exit positions are within 0.5 m of the same surface.

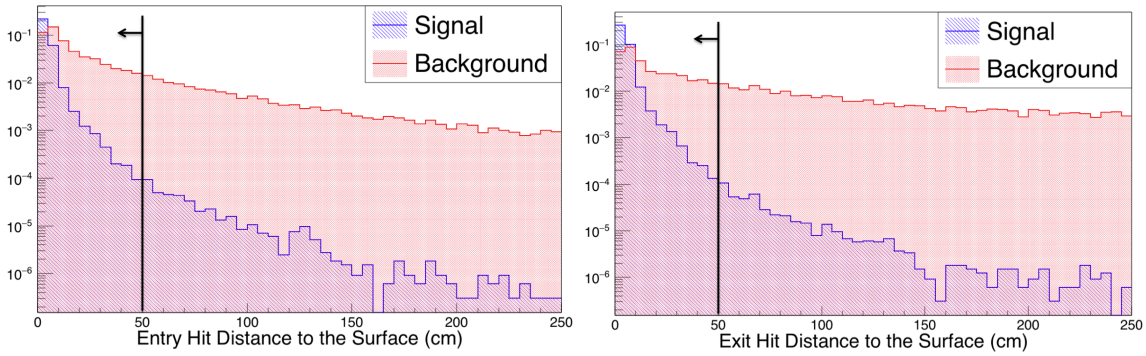

(a) (b)

Figure 6.18: The distance between (a) the entry and (b) the exit positions in the track to the detector surface, before preselection cuts 1 through 6. The penetration cut requires both entry and exit position be within 50 cm from the detector surface (black arrow).

6.2.8 Summary of Preselection Cuts

The performance of the preselection cuts is summarized in Table 6.1. More than 93% of signal events (simulated monopoles with uniform $\beta \in (10^{-4}, 0.2)$ which pass the fast monopole trigger) pass the preselection cuts. There are 959 tracks in the background data set passing the preselection cuts, out of 3.49×10^7 reconstructed tracks in the background data set. A total of 3.05×10^6 out of 3.27×10^6 reconstructed simulated monopole tracks (those monopole tracks that pass the fast monopole trigger and are successfully reconstructed) in the signal data set pass all the preselection cuts. Note that before the preselection cuts, 6.3% MC monopoles fail to be reconstructed

due to low velocity or lack of hits.

Table 6.1: Summary of the preselection cuts performance, assuming the standard estimate of energy loss and light yield.

Preselection Cut	Signal-Remaining-Efficiency	Signal-Rejection-Fraction	Background-Rejection-Fraction
1	99.98%	1.6×10^{-4}	94.1%
2	99.84%	14.4×10^{-4}	94.4%
3	93.77%	33.0×10^{-3}	74.0%
4	93.52%	26.1×10^{-4}	89.8%
5	93.52%	5.6×10^{-5}	7.0%
6	93.34%	19.2×10^{-4}	10.3%
7	93.15%	20.2×10^{-4}	58.3%

The rejection rate for both signal and background data set are evaluated for each cut individually. The preselection cuts are performed in the order as listed in Table 6.1, and the signal remaining efficiencies are calculated after each cut.

6.3 Function Discriminant Analysis

The strategy of monopole identification is to search for either heavily ionizing or convincingly non-relativistic reconstructed penetrating tracks. Hence the saturated hits ratio ρ and the reconstructed velocity β have been chosen to be the input variables for the final selection of the monopole signals. Figure 6.19 shows the distribution of ρ and β for both signal (simulated monopoles with standard light yield) and background data sets. We have compared various multivariate classification methods provided by the toolkit TMVA [49] used in high-energy physics. The best classification method would allow 0 background events to appear in the signal region (in the other words, the false positive rate would be rigorously zero), while preserving a high signal identification efficiency.

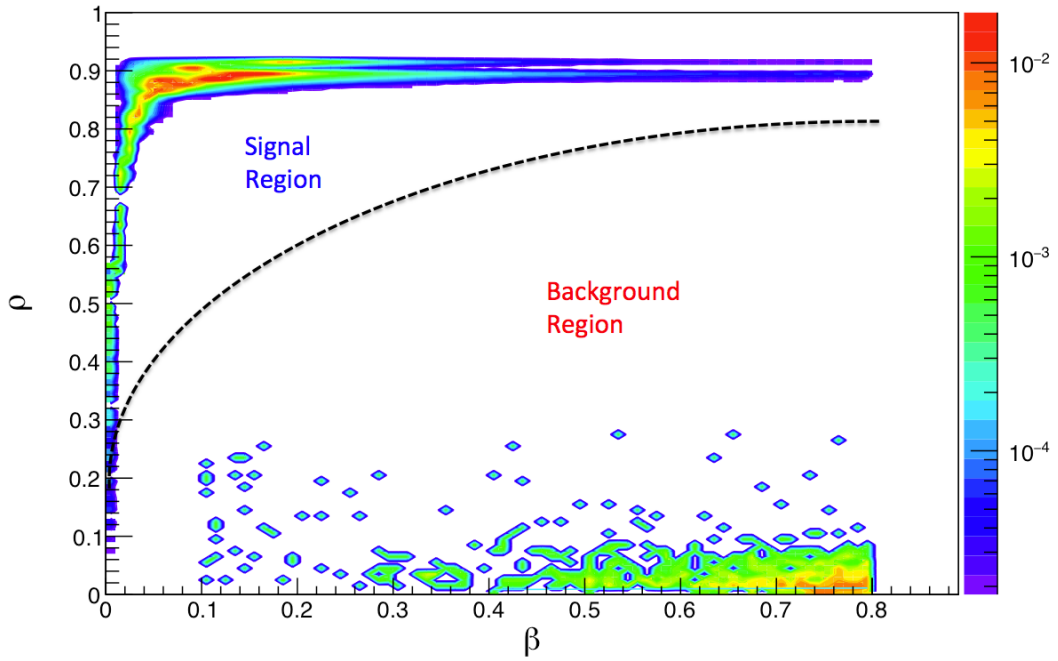

Figure 6.19: The distribution of ρ and β of the Monte Carlo monopole events with standard light yield (signal data set) and cosmic data events (background training data set) that pass the preselection cuts. Each data set is unit normalized. Most signal events appear in the left top region of the plot, while most background events appear in the right bottom region of the plot. The black dashed line illustrates a possible classification method; the method described in the text produces a more optimal choice.

A simple and good performing method, the function discriminant analysis (FDA), has been adopted. A score function of β and ρ, is defined as:

$$FDA(\beta, \rho) = C_1(0.8 - \beta)^2 + C_2\rho^2\,, \tag{6.9}$$

where the coefficients C_1 and C_2 are determined by maximizing the separation between background and signal, through maximizing the following function:

$$\langle S^2 \rangle = \frac{1}{2} \iint \frac{(pdf_S - pdf_B)^2}{pdf_S + pdf_B} d\rho d\beta\,, \tag{6.10}$$

where pdf_S and pdf_B are the signal and background probability density functions, which depend on the variables ρ and β. The probability density functions are calculated based on the distributions of FDA scores, hence the separation $\langle S^2 \rangle$ depends on C_1 and C_2. The reconstructed tracks passing the preselection cuts must have a reconstructed velocity below $0.8c$, so the first term in Eq. 6.9 is in the form $C_1(0.8-\beta)^2$. The optimized coefficients are $C_1 = 0.200$ and $C_2 = 0.872$, and the FDA score distributions of signal and background events for the training data set are shown in Fig. 6.20, under the assumption that there were no actual monopoles.

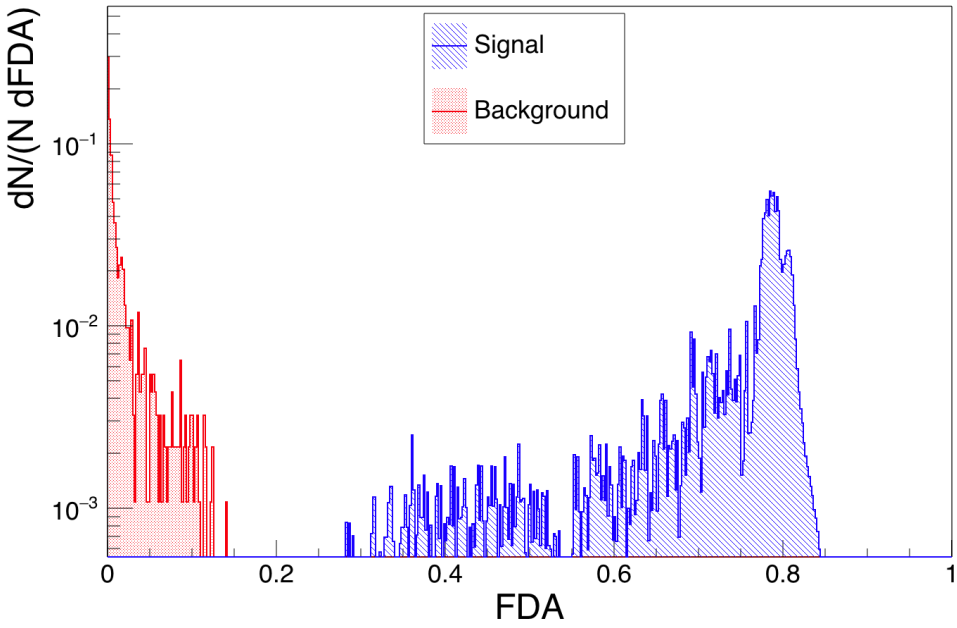

Figure 6.20: The FDA scores (with unit normalization) of signal (blue) and background (red) events after all preselection cuts. The background events tend to have low ρ values, and the maximum background score is 0.13, which is the FDA score when both ρ and β are very small.[4]

The correlation between the two training variables β and ρ, is shown in Fig. 6.27. The correlation in the signal data set is understood: monopoles with larger velocity

[4]The coefficients C_1 and C_2 are calculated with the background training data set and the Monte Carlo data set with default Geant4 light yield. In this plot, we show the distribution of FDA score of Monte Carlo data set with standard light yield. Thus the signal distribution has shifted from 1.

(β) tend to be more heavily ionizing with a larger saturated hits ratio (ρ), whereas in the background data set, these two variables are almost independent.

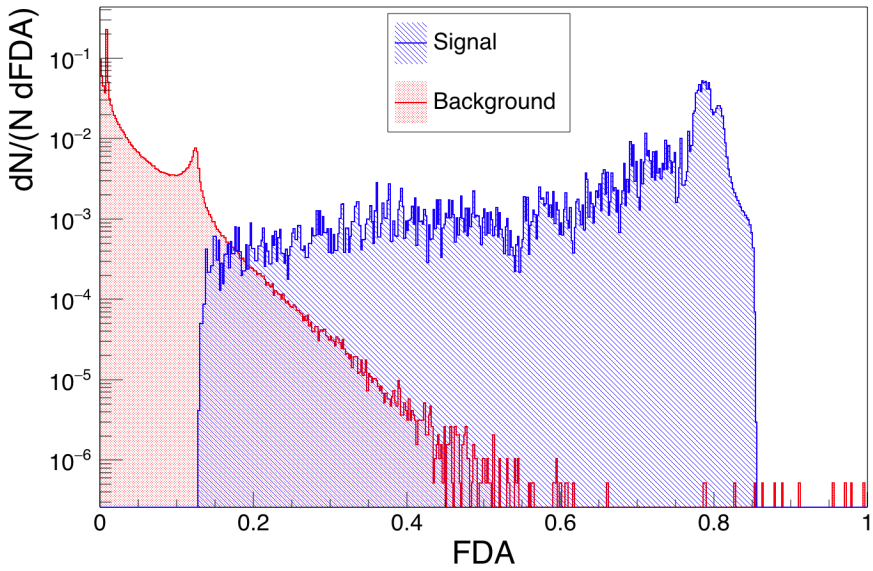

Figure 6.21: The FDA scores (with unit normalization) of signal (blue) and background (red) events, after preselection cut 1 (saturated hits number cut).

The coefficients C_1 and C_2 are normalized so that $0.64C_1 + C_2 = 1$. This restricts the FDA score to be within the range (0,1), so it can be treated as a probability density function. We use it to predict the upper sideband of the background, which will be discussed in detail in the next section.

The effect of each preselection cut on the FDA is shown in Figs. 6.21 through 6.26 The overlap between signal and background becomes progressively less (the separation gets larger), with each additional cut, and eventually they are well separated, as seen in Fig. 6.20.

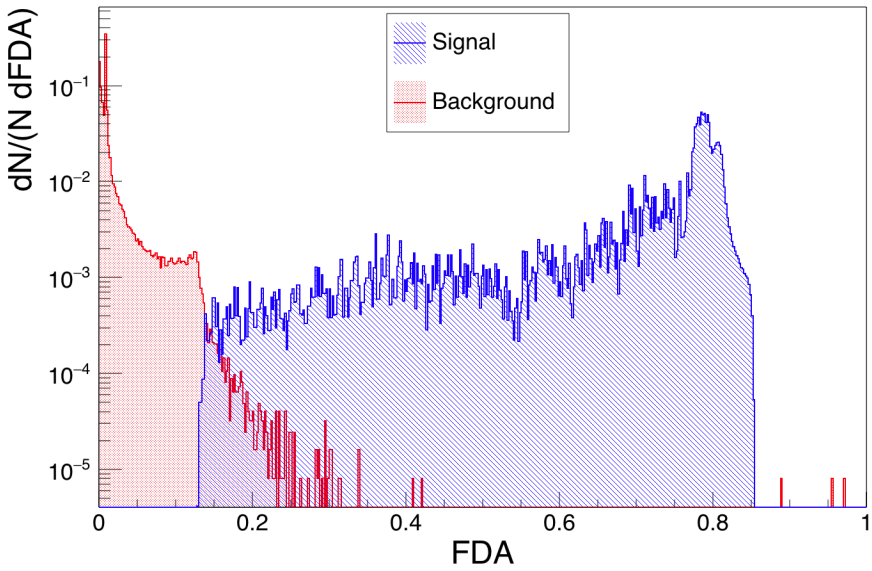

Figure 6.22: The FDA scores (with unit normalization) of signal (blue) and background (red) events, after preselection cut 1 and cut 2 (track fatness cut).

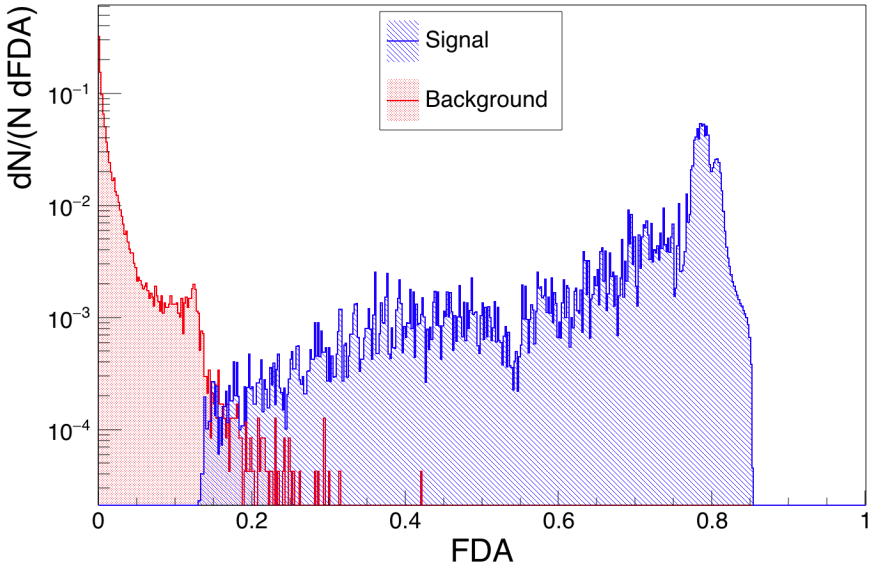

Figure 6.23: The FDA scores (with unit normalization) of signal (blue) and background (red) events, after preselection cut 1 through cut 3 (velocity validation cut).

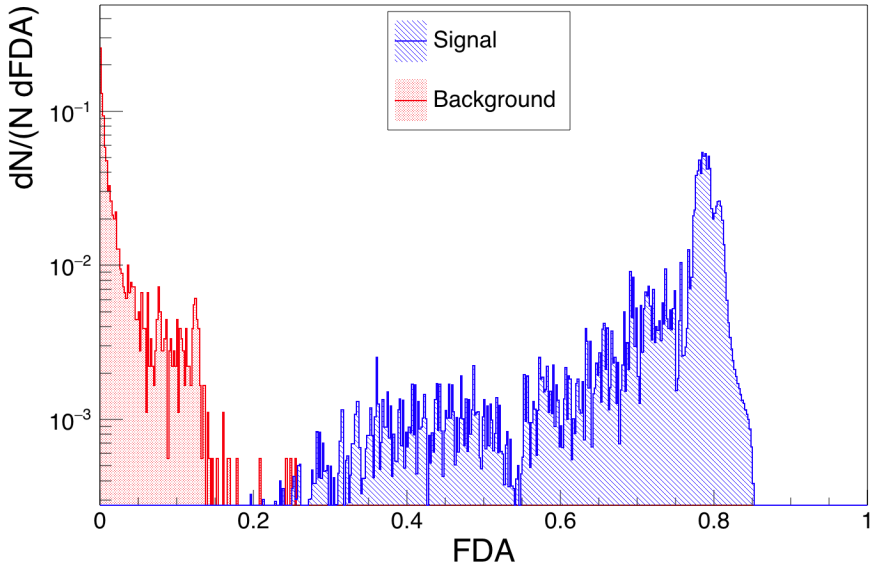

Figure 6.24: The FDA scores (with unit normalization) of signal (blue) and background (red) events, after preselection cut 1 through cut 4 (bremsstrahlung rejection cut).

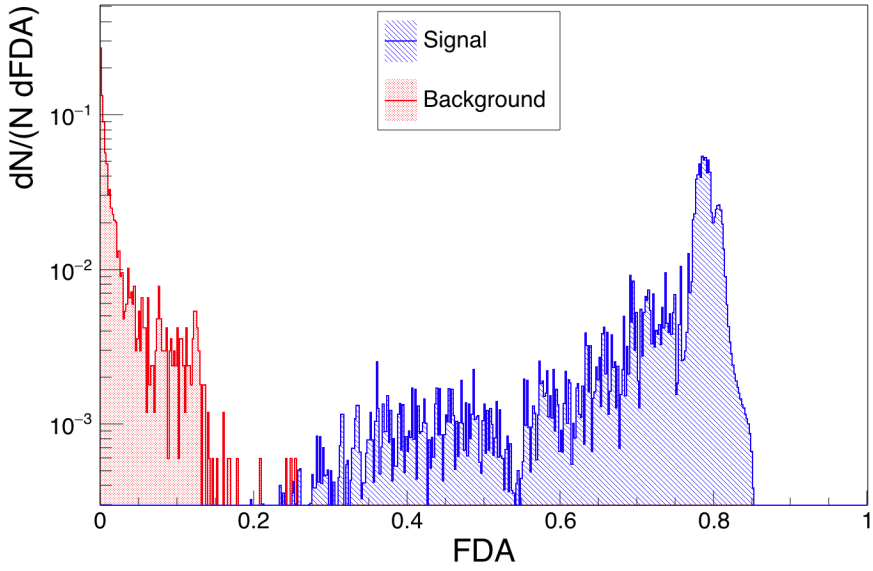

Figure 6.25: The FDA scores (with unit normalization) of signal (blue) and background (red) events, after preselection cut 1 through cut 5 (maximum gap cut).

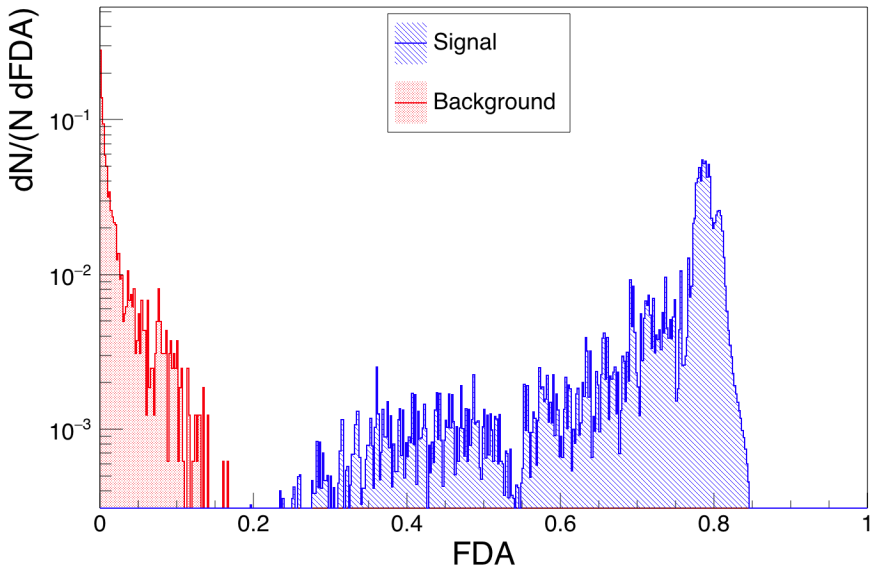

Figure 6.26: The FDA scores (with unit normalization) of signal (blue) and background (red) events, after preselection cut 1 through cut 6 (time window cut). In this plot, there is one track in the background training data set with a particularly high score of 0.17. This is a high-energy cosmic muon with bremsstrahlung. It is rejected by the last preselection cut (penetration cut).

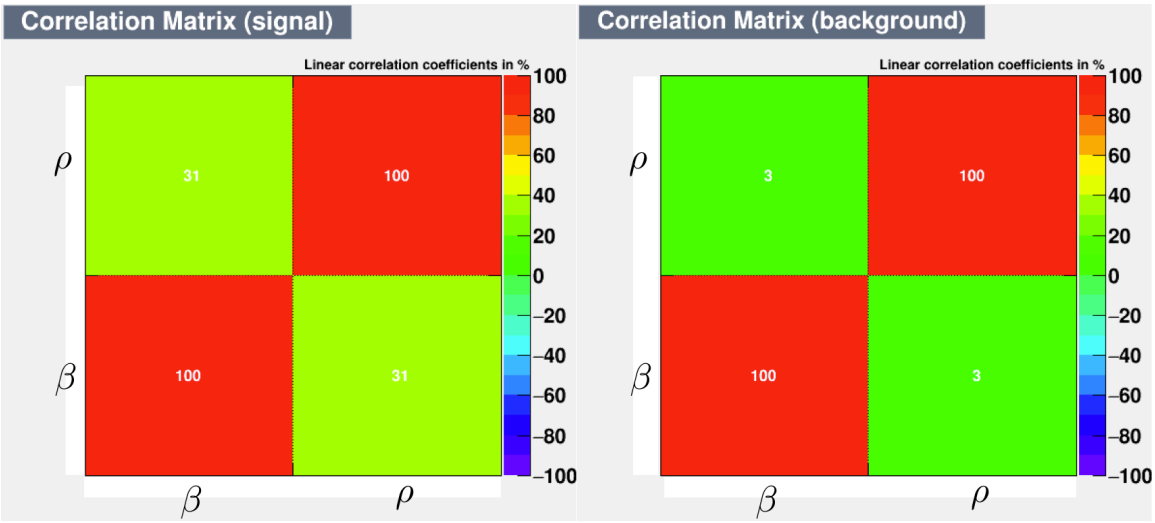

(a) (b)

Figure 6.27: The correlation matrices of the two training variables, β and ρ in (a) the signal data set and (b) the background data set.

6.4 Background Prediction and Detection Efficiency

To predict the upper sideband of the background for high FDA values, we perform an exponential fit in the region (0.006,0.4) of the FDA background distribution:

$$F(\beta, \rho) = e^{-p_0 - p_1 \cdot \mathrm{FDA}} . \tag{6.11}$$

The best fit result is $p_0 = 3.05 \pm 0.19$ and $p_1 = 45 \pm 19$. Such a prediction based on so little live time is fraught with uncertainty, so we carried out a conservative background sideband prediction using: $p_0' = 2.85$ and $p_1' = 26$. The best fit background prediction, the 1 σ upper band of the fit, as well as the conservative prediction, is shown in Fig. 6.28.

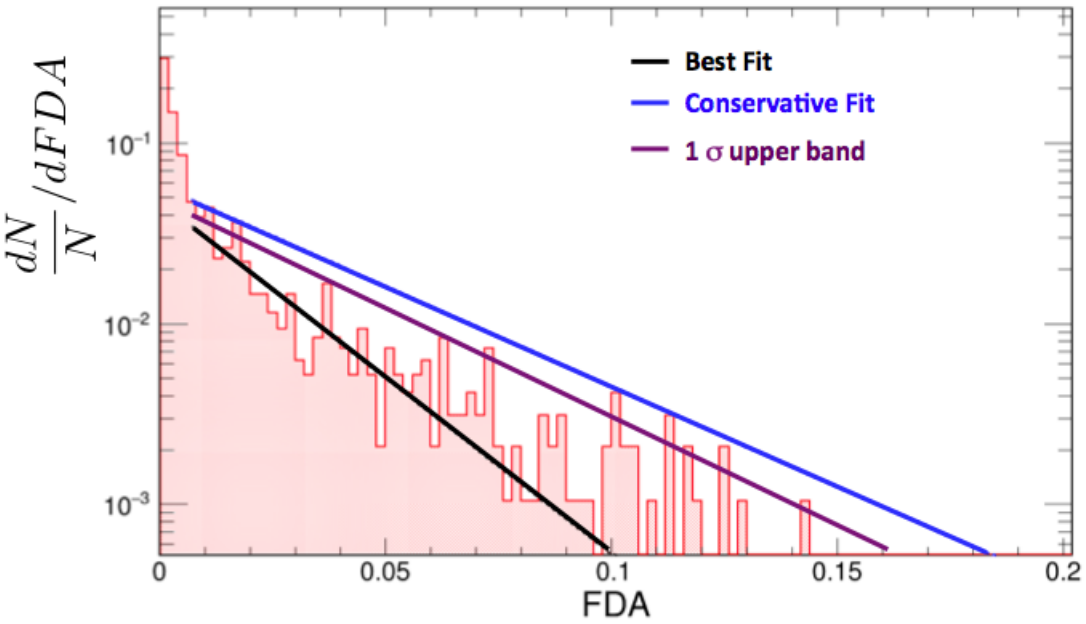

Figure 6.28: The background FDA score distribution (with unit normalization) from the training data set with the best fit (black) line, the 1σ upper band (purple) line, and the conservative fit (blue) line to the tail of the distribution. Since the p_0 and p_1 are correlated, the conservative fit is not the 1σ upper band.

Using the prediction from the background sideband, we present the time it would take to accumulate enough data to have a far detector event with a FDA score larger than a given FDA cut. Figure 6.29 shows that time for the best fit and the conservative background sideband predictions.

The largest FDA score of the background events in the training data set (for those that passed the preselection cuts) is 0.144. According to the conservative estimate, an event in far detector with an FDA score larger than 0.4 appears every 1.9 live years on average. It takes 314 live years to observe 1 event with an FDA score larger than 0.6, again according to the conservative estimate, and 7.78×10^7 live years according to the best-fit estimation. We expect a background-free search in that region.

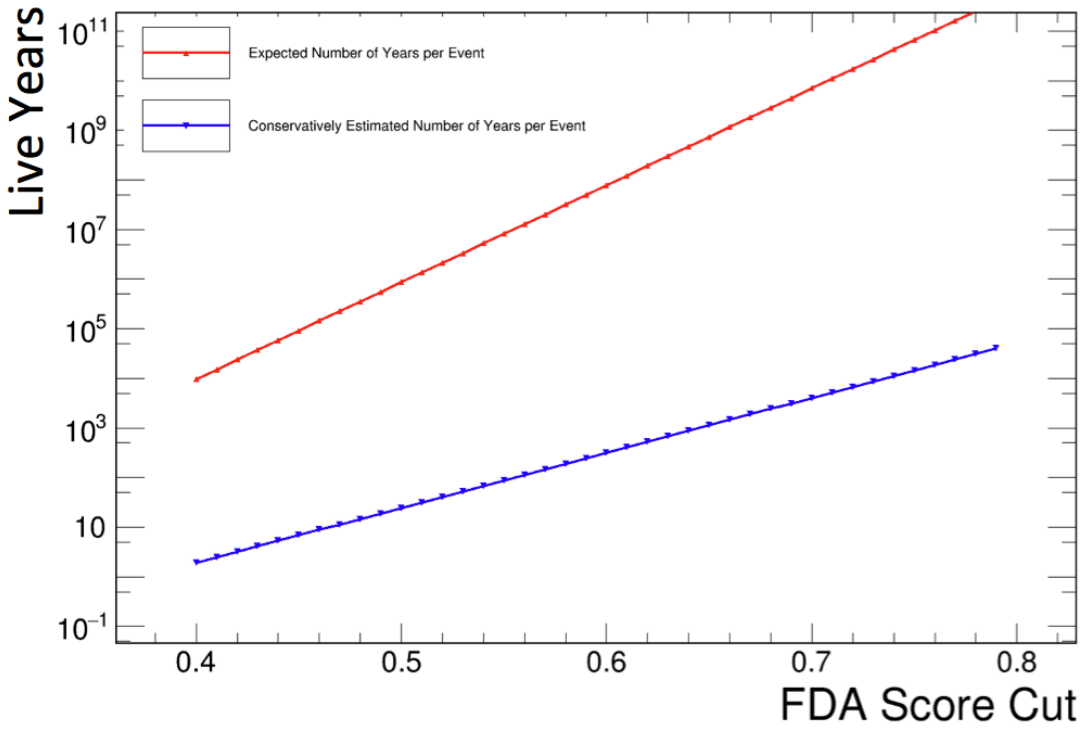

Figure 6.29: The FDA background predictions, in live years per event, in the NOνA far detector for the: (a) standard (given by the best fit) and (b) conservative estimates.

A region we call the control region is set to (0.4, 0.6), which is comfortably above the largest FDA score in the background training data set. It is used to first check if the background FDA extrapolation is reasonable. And only if that is the case, is the signal region of FDA > 0.6 opened up for examination.

We have calculated the detection efficiency with three sets of simulations (optimistic, standard and conservative), shown in Fig. 6.30, as we did for the calculation of the fast monopole trigger efficiency. This efficiency includes the trigger efficiency, reconstruction efficiency, preselection efficiency and functional discriminant efficiency.

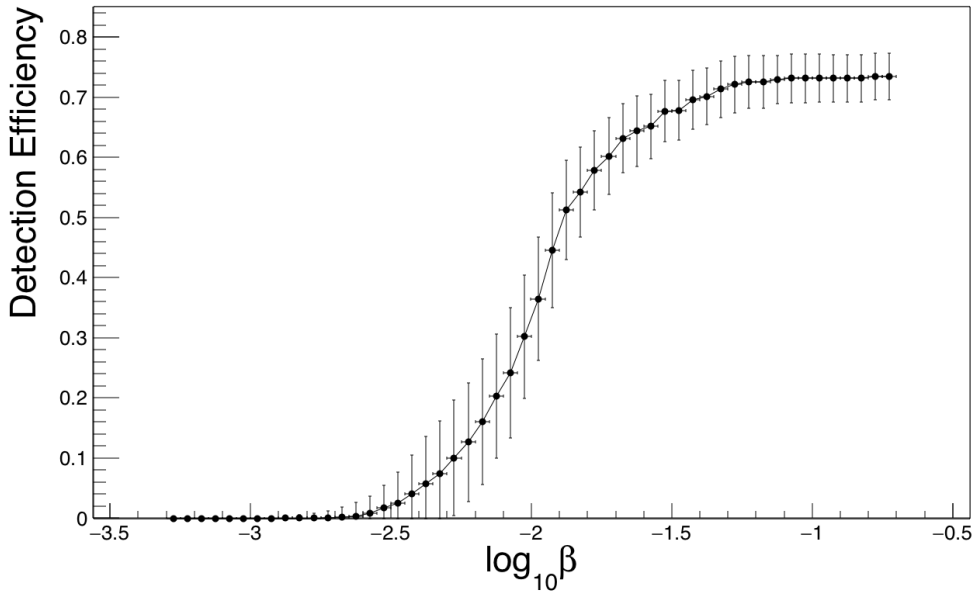

Figure 6.30: The final monopole detection efficiency with an FDA cut $\geqslant 0.6$. The optimistic estimation and the conservative estimation efficiency represent the upper and lower systematic uncertainties introduced in the simulation of the detector response to monopoles. The uncertainties in the individual points are statistical, and the bars in β represents the velocity bin size.

The final result is discussed in the next chapter.

6.5 Investigation of a Heavily Ionizing Flash Event

In the background training data set, we discovered an interesting heavily ionizing event recorded by the fast monopole trigger and reconstructed in offline, which is shown in Fig. 6.31. This event has a particularly high FDA score (0.75) but is cut out by the preselection cuts. Although very high-energy muons are expected to have wider tracks than minimum ionizing particles due to bremsstrahlung, this event is much wider than what is expected from such events. Hits with a large amount of deposited energy produce electronic noise hits in the same module due to crosstalk in the front end boards (FEB). These electronic noise hits are referred to as FEB flash hits. The event shown in Fig. 6.31 has FEB flash hits along the trajectory of a heavily ionizing cosmic track in the 59 planes which it crossed.

The time distribution of hits in two modules in two different planes (at two ends of the track) is shown in Fig. 6.32. The hits cluster around two time periods: an early time which is that of the particle producing the ionization, and a later time which is due to the FEB crosstalk caused by the real hits. All the FEB crosstalk hits have times more than 5 μs after the high-energy hits which caused them, and most of them have smaller DCS values: between 300 to 400 ADC. The two planes are at either end of the track, and are thus well separated in space.

This behavior is well understood in bench tests done in Caltech [50] [51]. An FEB channel with a large signal (high DCS value) through crosstalk produces a negative signal of about 2% of the amplitude in all the other channels in the FEB. If the initial signal (DCS value) is larger than about 250 times the threshold of the channel, then when the crosstalk signals return to baseline they re-trigger to produce hits more than 5 μs later. The FEB flash is the only type of crosstalk noise we have observed in the data so far which is not simulated in the Monte Carlo signal data set.

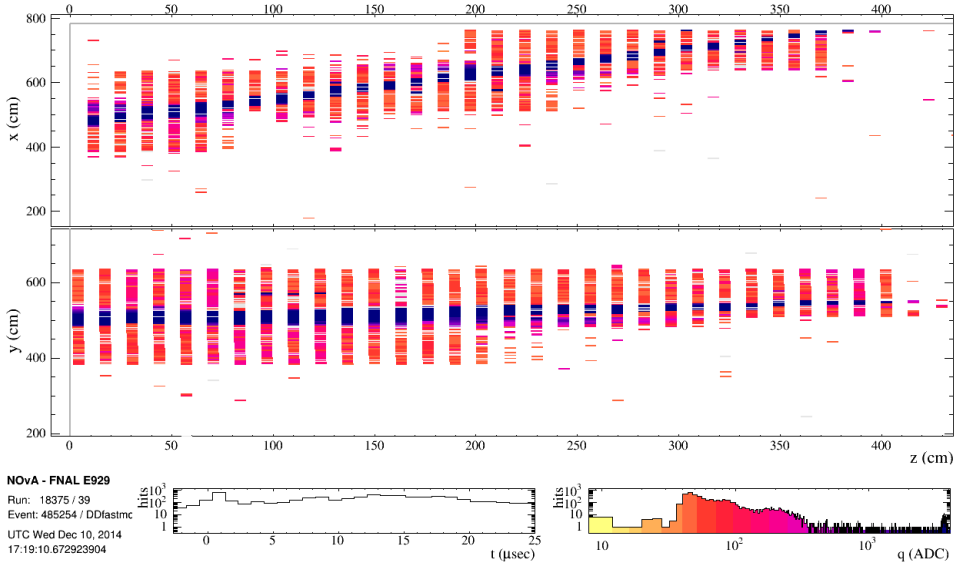

(a)

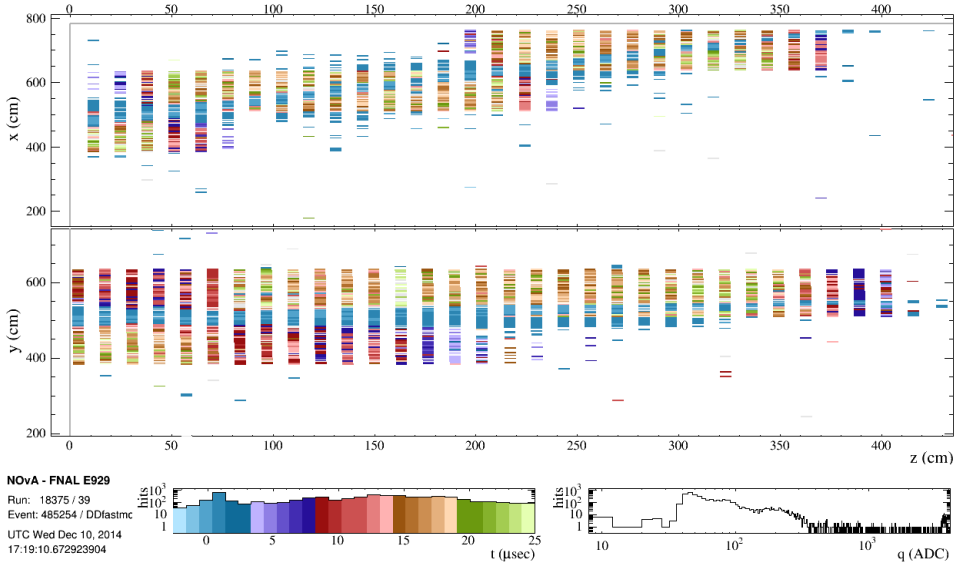

(b)

Figure 6.31: Event display of an interesting heavily ionizing flash event, where hits are colored by (a) DCS value and (b) raw hit time. Only a portion of the detector is shown in this plot.

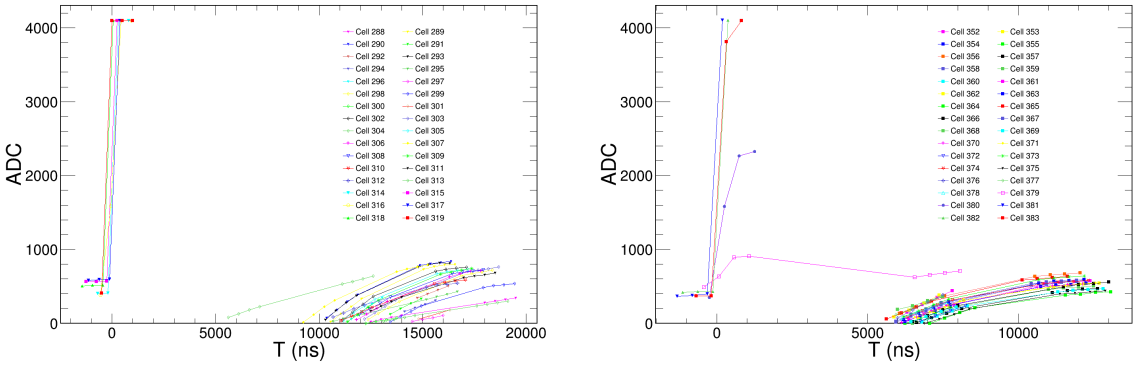

(a) (b)

Figure 6.32: The time distribution of hits in the flash event in two modules (FEBs) at different ends of the track. The ADC time samples of all the channels in one FEB of (a) module 9 of plane 2 and (b) module 11 of plane 55 are shown. The hits near time 0 are presumably from a heavily ionizing track, whereas later (> 5000 ns) hits are from crosstalk.

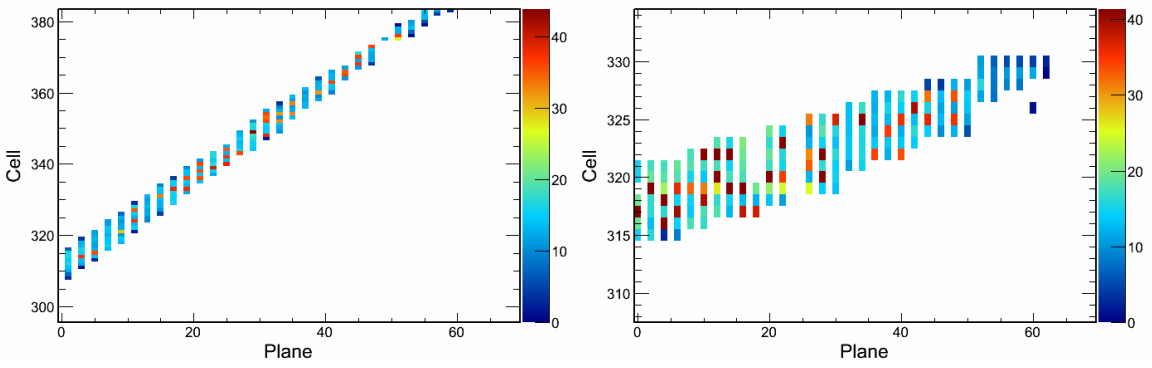

(a) (b)

Figure 6.33: The hits attached to the flash event after final reconstruction in the (a) X view and the (b) Y view. The color of each hit corresponds to the reconstructed visible energy in units of MIPs. Note that the scale is different (the Y view has a smaller cell range, and thus it looks wider).

How does the FEB flash affect the identification of such an event as a monopole? Not much due to the large separation in time between the FEB flash crosstalk hits and the high-energy hits causing them, as well as the low DCS values of FEB flash crosstalk hits (most are lower than the 500 ADC threshold applied when slicing). Hence the slicing algorithm applied in trigger and reconstruction will exclude most of the FEB flash hits from the monopole slice, as shown in Fig. 6.34. The track reconstruction algorithm described in Chapter 5 will further reject the remaining FEB flash hits in the monopole slice by excluding hits more than 14 cm away from the main trajectory, as illustrated in Fig. 6.33.

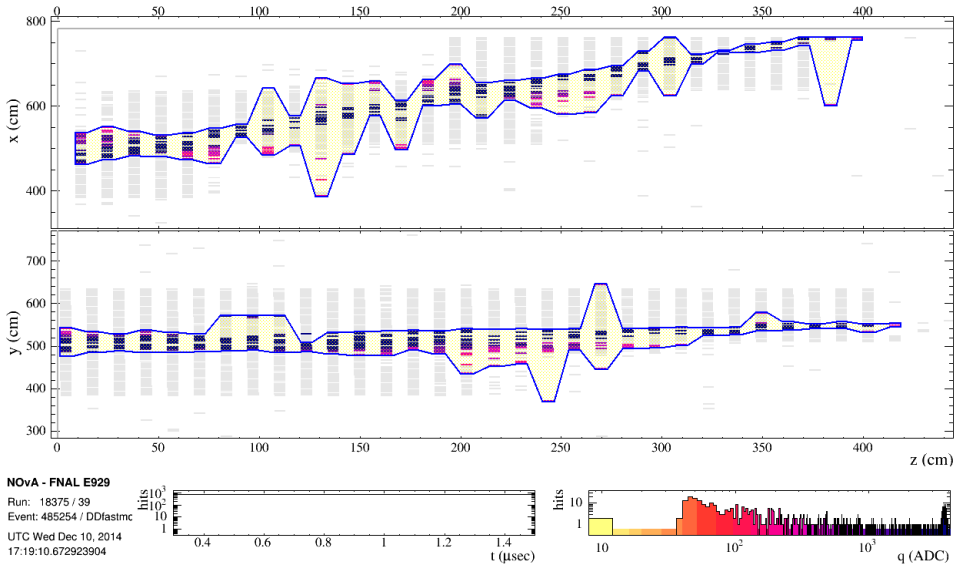

Figure 6.34: The event display of the flash event reconstructed offline by the fast monopole slicer. Hits not included in the reconstructed slice have been dimmed.

The hits associated with the reconstructed track in the event are shown in Fig. 6.33. This track has a reconstructed track length of 523 ± 6 cm, with 344 saturated hits out of 374 total number of hits attached to the track, and a visible energy deposit of 71.9 GeV. The reconstructed velocity of this track is $\beta = 0.57$ with an uncertainty of 262%, which suggests this is a relativistic particle which we are unable to tell its

direction given the poor timing resolution of the saturated hits. Hence, this track does not pass the velocity validation preselection cut. The track fatness is $\sigma_{Lx} = 638$ cm^2 in X view and $\sigma_{Ly} = 111$ cm^2 in Y view, indicating the bremsstrahlung process of a charged particle, which would not occur for a monopole track. Hence, it does not pass the track fatness preselection cut either.

Chapter 7

Results

7.1 Search Result

After performing the preselection cuts on the reconstructed tracks we obtain the FDA score distribution of the 3-month data set selected by the fast monopole trigger. Before we opened the box to check the entire FDA distribution, we performed an exponential fit in the region (0.006,0.4) with the function:

$$F_N(\beta, \rho) = Ne^{-p_0 - p_1 \cdot \mathrm{FDA}}. \tag{7.1}$$

as we did using the one-week training data set. The parameter N is the total number of events in the background region. The best fit to the distribution is consistent with the predicted best fit from the training data set, as shown in Fig. 7.1. No events were found in the control region (0.4,0.6). We then opened the blinded box in the signal region [0.6, 1.0] and we found no events.

7.2 Monopole Flux Upper Limits in NOνA

The null result that we have observed can be used to set an upper limit on the monopole flux that reaches the NOνA far detector. As discussed in Chapter 1 and

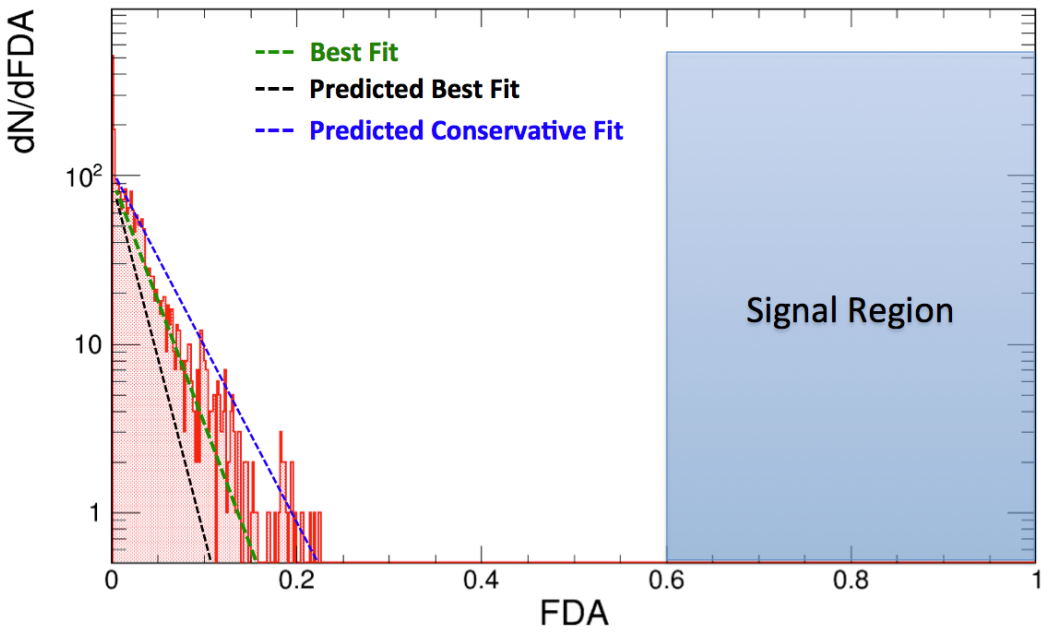

Figure 7.1: The FDA score distribution of the reconstructed tracks in the three-month data set after preselection cuts with the signal region blinded. The best fit values are $p_0 = 2.97 \pm 0.13$ and $p_1 = 31 \pm 16$. Note this plot is not unit normalized and we use the same bin size (0.01 FDA) as we use in Fig. 6.28. After opening the blinded signal region no events were found.

shown in Fig. 1.11, NOνA is sensitive to phase-space regions in monopole mass and velocity that have not been explored by previous experiments. The flux limit with 90% of CL $\Phi_{90\%C.L.}$ is calculated using :

$$\Phi_{90\%C.L.}(M,\beta) = \frac{4\mu_{90\%}}{A\Omega(M,\beta)T}\,, \tag{7.2}$$

where A is the effective detector surface area (4,082 m^2), Ω is the exposure solid angle at mass M and velocity β, as shown in Fig. 1.10, T is the accumulated live time, and $\mu_{90\%}$ is the upper limit of the expected number of monopole events at 90% CL. Note that for a fixed value of the final detection efficiency η, the value for $\mu_{90\%}$ is 2.3 with zero background events.

Assuming a Poisson distribution with the a mean number of events λ, the probability of observing k monopole events, using the Poisson limit theorem is:

$$P(k) = \int e^{-\lambda} \frac{\lambda^k}{k!} f_s(\eta) d\eta \,, \tag{7.3}$$

where η is the detection efficiency, f_s is the probability density for a given η, and $\lambda = \eta\mu$, where μ is the actual number of events. As shown in Fig. 7.1, no background events are expected.

The detection efficiency is shown in Fig. 6.30. We take the uncertainty in the final detection efficiency to be any value between the conservative and the optimistic estimates given in that figure. Applying the Rolke Model [52] and assuming the detection efficiency is equally likely for any value between $[\eta_1, \eta_2]$, where η_1 is the conservative detection efficiency and η_2 is the optimistic detection efficiency, we have calculated $\mu_{90\%}$ as a function of monopole speed β. The corresponding flux upper limit shown in Fig. 7.2. The flux limit varies from 9.6×10^{-12} cm^{-2}s^{-1}sr^{-1} at $\beta \approx 10^{-3}$, $M \approx 4 \times 10^8$ GeV, to 3.6×10^{-15} cm^{-2}s^{-1}sr^{-1} at $\beta \approx 0.2$, $M \approx 1 \times 10^{18}$ GeV. The low mass and low β region in the left-hand corner of Fig. 7.2 is particularly interesting as it is virgin territory first probed by NOνA, as explained in Chapter 1. We have tabulated the results in this phase-space region in Table 7.1.

Table 7.1: Monopole (with one Dirac charge) flux upper limits (cm^{-2}s^{-1}sr^{-1}) at 90% CL in the low mass region.

Mass (GeV) \ β	2.1×10^{-3}	6.7×10^{-3}	1.9×10^{-2}	8.4×10^{-2}
3.55×10^8	1.16×10^{-12}	3.01×10^{-14}	9.42×10^{-14}	7.37×10^{-15}
8.91×10^8	2.72×10^{-13}	2.47×10^{-14}	8.86×10^{-14}	7.27×10^{-15}
4.47×10^9	1.94×10^{-13}	2.25×10^{-14}	8.59×10^{-15}	7.22×10^{-15}
8.91×10^9	1.87×10^{-13}	2.23×10^{-14}	8.56×10^{-15}	7.21×10^{-15}

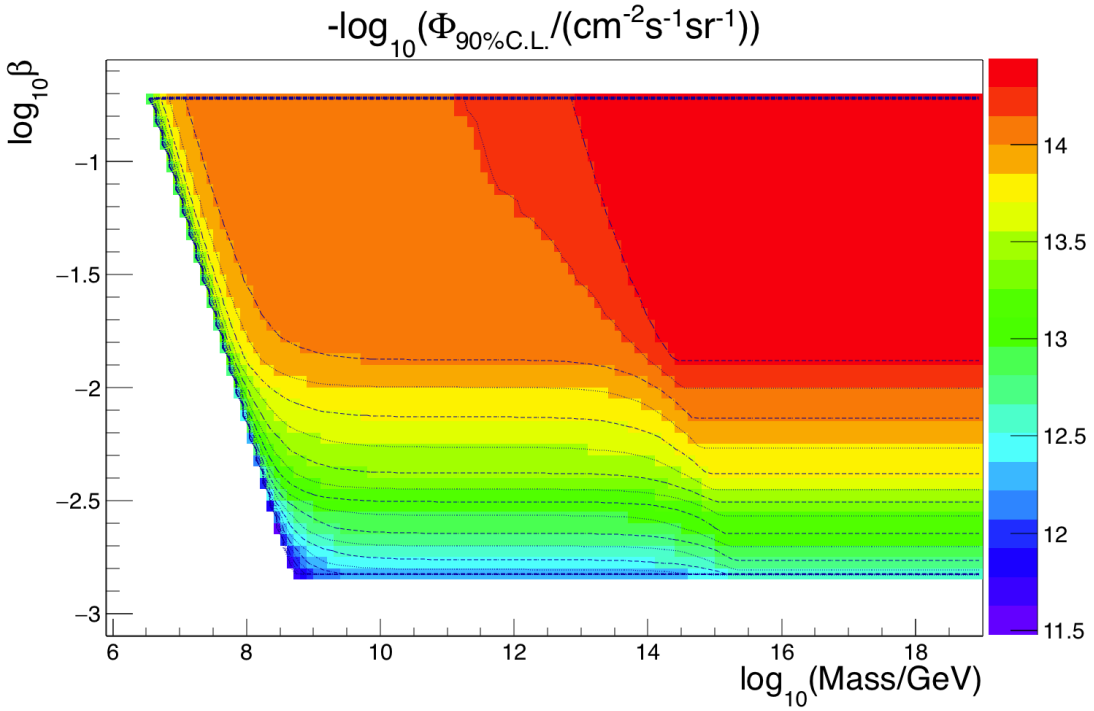

Figure 7.2: The flux upper limit with 90% CL for monopoles with one Dirac magnetic charge ($g_D = 68.5e$).

Chapter 8

Conclusions and Future Work

8.1 Conclusion

We have implemented the simulation of monopoles in the NOνA detector, developed monopole track reconstruction algorithms, and monopole data-driven triggers. Using a strictly blind analysis procedure, we have observed no monopole events in a 3-month exposure at the NOνA far detector.

The monopole flux limit includes a phase-space region not covered by previous experiments. Combining this result with limits set by previous experiments (see Fig. 1.11 in Ch. 1), we present the updated flux limits for monopoles only carrying one Dirac magnetic charge without additional electric charge in Fig. 8.1. In this analysis, the detection efficiency depends on the energy loss via ionization and atomic excitation of monopoles in the scintillator, and not monopole catalysis of proton decay. Assuming the current detection efficiency (and assuming monopoles do not catalyze proton decay), we will have the best limits for $0.01 < \beta < 0.8$ monopoles after a six-year run.

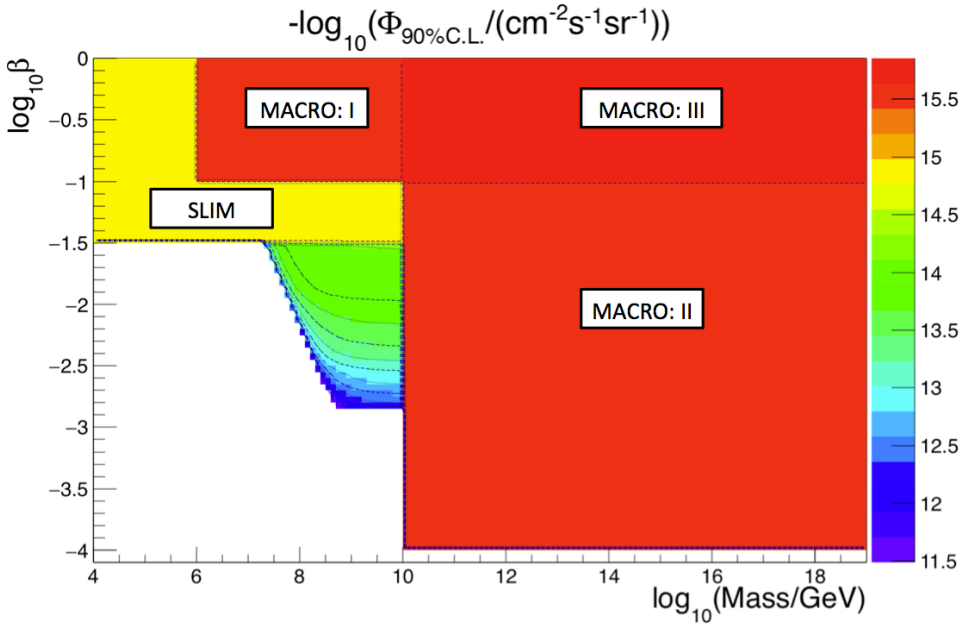

Figure 8.1: The flux upper limits of magnetic monopoles with one Dirac magnetic charge at 90% CL, combined with the limit set by MACRO (I and II: 2.8×10^{-16} $\mathrm{cm^{-2}s^{-1}sr^{-1}}$; III: 1.4×10^{-16} $\mathrm{cm^{-2}s^{-1}sr^{-1}}$) and SLIM (1.3×10^{-15} $\mathrm{cm^{-2}s^{-1}sr^{-1}}$) [31] [32] .

8.2 Future Work

We have developed all the tools needed to trigger, simulate, and analyze NOνA far detector data to search for magnetic monopoles. And we have presented results for a first search which shows this capability of the NOνA far detector. For future work, we plan to overlay the simulated monopoles with real data. This will allow a more precise estimate of trigger and reconstruction efficiencies to be made. Upgrades to the data-driven trigger hardware are planned to enable all 200 buffer nodes to be used, rather than the 47 used in this analysis. This would allow 13 seconds for trigger decisions to be made, rather than 3 seconds. This timing cap affects the slow monopole trigger more as it has to consider many more hits in a much larger time window. Once all the buffer nodes are included, we will lower, and perhaps remove the DCS value cut in the slow monopole trigger, which will increase the trigger efficiency in the slower velocity region, where monopoles are expected to be minimum ionizing particles. In

the future work, we are considering measuring the scintillator response to heavily ionizing particles, which can reduce the systematic uncertainty in simulation.

The tools for the monopole search have been developed and are functioning well. Both monopole triggers will be taking data for some years and the search will continue.

Appendix A

Slow Magnetic Monopole Trigger

We explain here the algorithms and performance of the slow monopole trigger. Though the analysis of the data recorded by the slow monopole trigger is not included in this thesis, it contains some important work I carried out in conjunction with the analysis described in this thesis.

A.1 Slow Monopole Trigger

Adjacent hits in a slow monopole track have large time separation. Thus, a large time window ($TWindow$) is required to group all the hits belonging to a slower monopole event. However, simply extending the allowed time gap in slicing to determine if two hits are causally related would cluster all the hits in the milliblock into one slice, making the clustering process meaningless. This causes the drop of the fast monopole trigger efficiency as the monopole velocity goes down, shown in Fig. 4.16. Thus, we have developed an entirely different algorithm from the slicing algorithm introduced previously, to find possible slow monopole tracks.

A.1.1 Triangle Algorithm of the Slow Monopole Trigger

The triangle algorithm triggers on any slowly moving charged particle as long as it penetrates the detector. The main challenge of this trigger is to finish the trigger decision within the limited time available. Thus the algorithm only operates on the hits from one view. Due to the fact that we generally have more hits in horizontal planes (Y-view hits) in our selected ADC range [150,4095],[1] the algorithm is naturally applied in the X view.

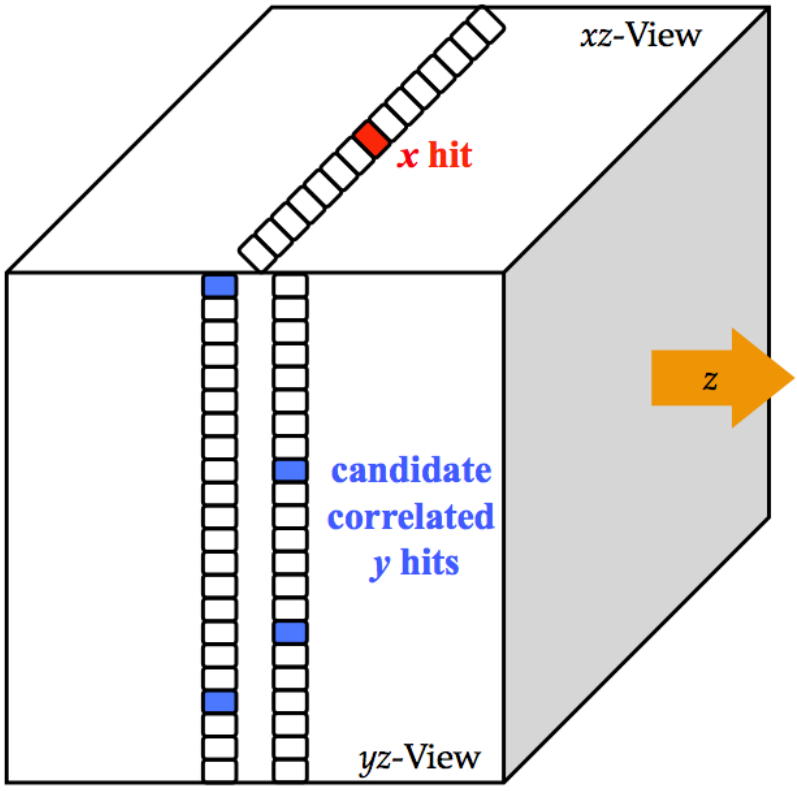

Figure A.1: Illustration of the view check process: an X-view hit is considered noise if it does not have any Y-view hits in the adjacent planes within $[t_x - \Delta T, t_x + \Delta T]$, where t_x is the X-view hit time and $\Delta T = 2000$ ns.

[1] This is determined by the limit of execution time, which we shall talk about in the following section.

To reduce the number of hits involved in the triangle algorithm, a view check, illustrated in Fig. A.1, judges whether an X-view hit is correlated with any Y-view hit in adjacent planes. The X-view hit is considered to be a surface hit, if either itself is close to the surface of the detector, or it has a correlated Y view hit that is close to the surface of the detector, as illustrated in Fig. A.1. Figure A.4 is the flow chart of the entire slow monopole trigger algorithm, and view check is immediately performed for the incoming hits. The boundary hits and the contained hits are stored as separate groups simultaneously with view check process.

The Penetration Test is adopted in the slow monopole trigger as well. However, unlike the fast monopole trigger using the Penetration Test as one of the trigger cuts after the reconstruction, the slow monopole trigger starts with it for a simple 2D track reconstruction.

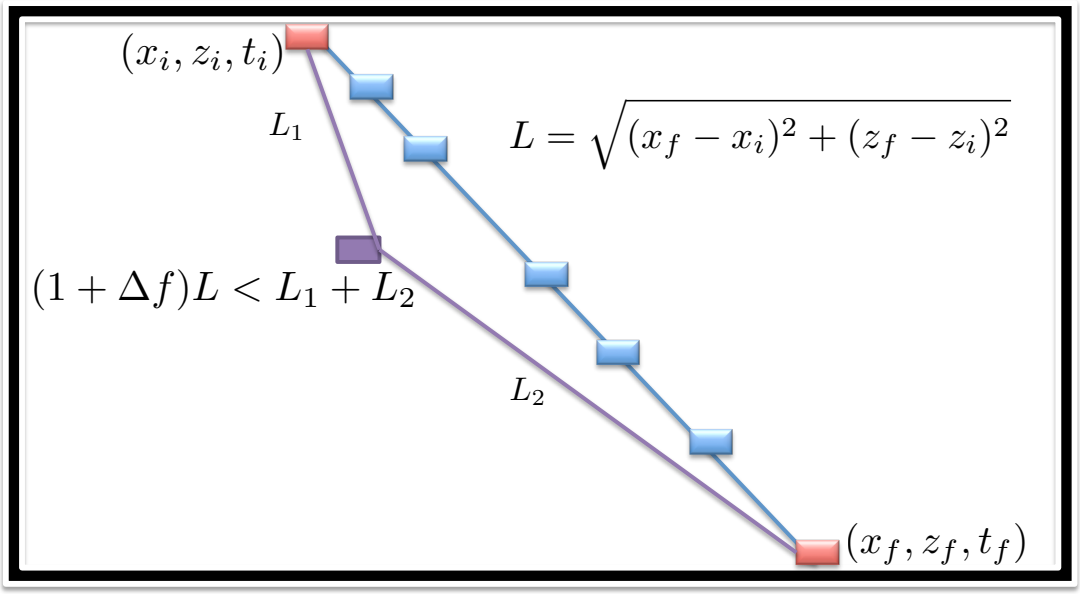

Figure A.2: Illustration of the triangle algorithm to judge whether a hit is on track.

First, it looks for hits close to the surface of the detector to be possible entry and exit hits. As illustrated in Fig. A.2, for every possible combination of entry (with

space-time coordinate (x_i, z_i, t_i)) and exit (with space-time coordinate (x_f, z_f, t_f)) hits (the red cell hits in Fig. A.2), it loops over all the hits within the time window (t_i, t_f) and the space region $x \in (x_i, x_f)$ and $z \in (z_f, z_i)$. These hits are referred to as "intermediate hits" for a particular surface hits combination. To judge whether a hit belongs to this possible track, the distance is calculated from the intermediate hit to the two surface hits. The distance to the "entry" (earlier) hit is L_1, and to the other surface hit is L_2. Their summed values are compared to the distance between the entry and exit hits (L). If the hit is geometrically on the line, L should be equal to $L_1 + L_2$ within a fractional uncertainty Δf: $L_1 + L_2 < (1 + \Delta f)L$, where Δf is set to be 0.01.

For each combination of surface hits, the inverse speed of the putative track is obtained, $Vpro = (t_f - t_i)/L$. There are two expected hit times for each cell based on either the "entry" or "exit" hit times:

- **based on entry hit:** $t_{exp1} = t_i + L_1 \times Vpro$
- **based on exit hit:** $t_{exp2} = t_f - L_2 \times Vpro$

Figure A.3 shows the difference between the calculated time and the true hit time for MC generated monopoles, which indicates that the calculation based on the surface hit further away is best as expected.

To reduce the execution time, we set a list of requirements to meet before we perform the triangle algorithm for a certain combination of surface hits:

- **Cross Plane Check** – The plane difference of the two surface hits is required to be no less than 4 planes. This cut gets rid of vertical tracks which cannot be reconstructed in 3D.

- **Distance Check** – The two surface hits are required to be adequately separated. To simplify the calculation, the plane and cell number are used to characterize the length.

- **Velocity Check** – The inverse velocity projection in the X view calculated using the two surface hits is required to be within range (1.472, 200) cells/TDC, which roughly corresponds to the range $\beta \in (10^{-4}, 10^{-2})$.

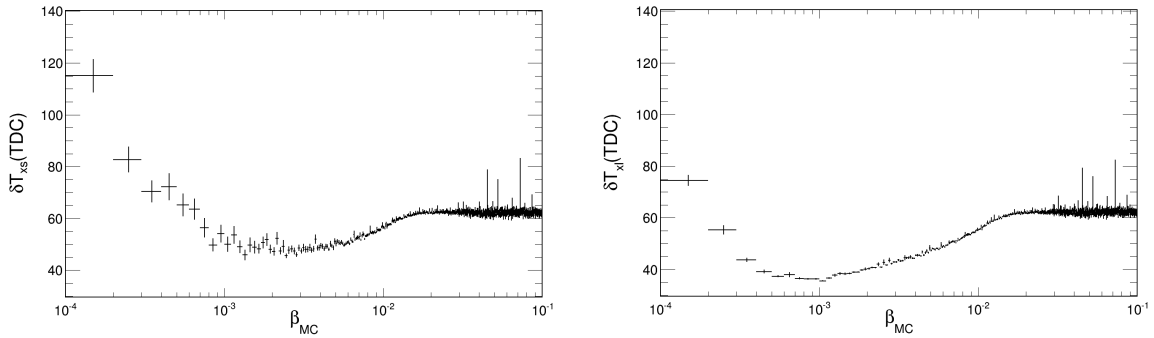

Figure A.3: The absolute value of the difference between the true hit time and calculated hit time based on the (a) closer and the (b) further surface hit used to determine the putative track.

The signal to trigger a possible slow monopole event is to check whether the accumulated intermedia hits has reached the cut: ρL, where the linear hits density cut ρ is set to be 0.1 and L is the putative track length.

If the total execution time has exceeded the maximally allowed time (the so called "execution time cap"), the process will terminate and issue a smallest inclusive trigger window: $[t_i - \Delta T, t_f + \Delta T]$, where t_i is the time of the current "entry" hit, t_f is the time of the corresponding "exit" hit, and the additional buffer time $\Delta T = 50$ ns. This avoids a drop of efficiency, and the waste of the computation done upon the incoming milli-block data.

Table A.1: List of parameters in the slow monopole trigger.

Parameter	Value	Description
$Dist_{min}$	100 cells	The minimum 2D distance required for two surface hits to be considered as a possible combination of entry and exit hits belonging to a same slow track.
$\frac{1}{v_x\,min}$	1.472 (TDC/cells)	The minimum allowed inverse velocity projection on X view estimated by the combination of surface hits.
$\frac{1}{v_x\,max}$	200 (TDC/cells)	The maximum allowed inverse velocity projection on X view estimated by the combination of surface hits.
δP	2	A hit as well as its correlated hits on the other view, is assigned to the surface hits container if it took place within this number of planes away from the boundary of the detector.
δC	6	A hit as well as its correlated hits on the other view, is assigned to the surface hits container if it took place within this number of cells away from the boundary of the detector.
Δf	0.01	Maximum allowed additional length relative to the distance between the two surface hits. This parameter is used in determining whether an "intermediate" hit is geometrically along the track.
σT	64 TDC (1 μs)	Maximum allowed time difference cut in determining whether an "intermediate" hit belongs to a certain "slow" track candidate. This value is determined by b) of Fig. A.3, which includes the single-cell-hit time uncertainty and the geometry resolution(involved when calculating the velocity of a surface hits combination).
ΔT	128 TDC (2 μs)	Maximum allowed time difference cut in determining the associate hits on the other view; Time buffer added to extend the trigger window size on both ends.
ρ_{min}	0.1	Minimum number of linear hits density to trigger a putative track.

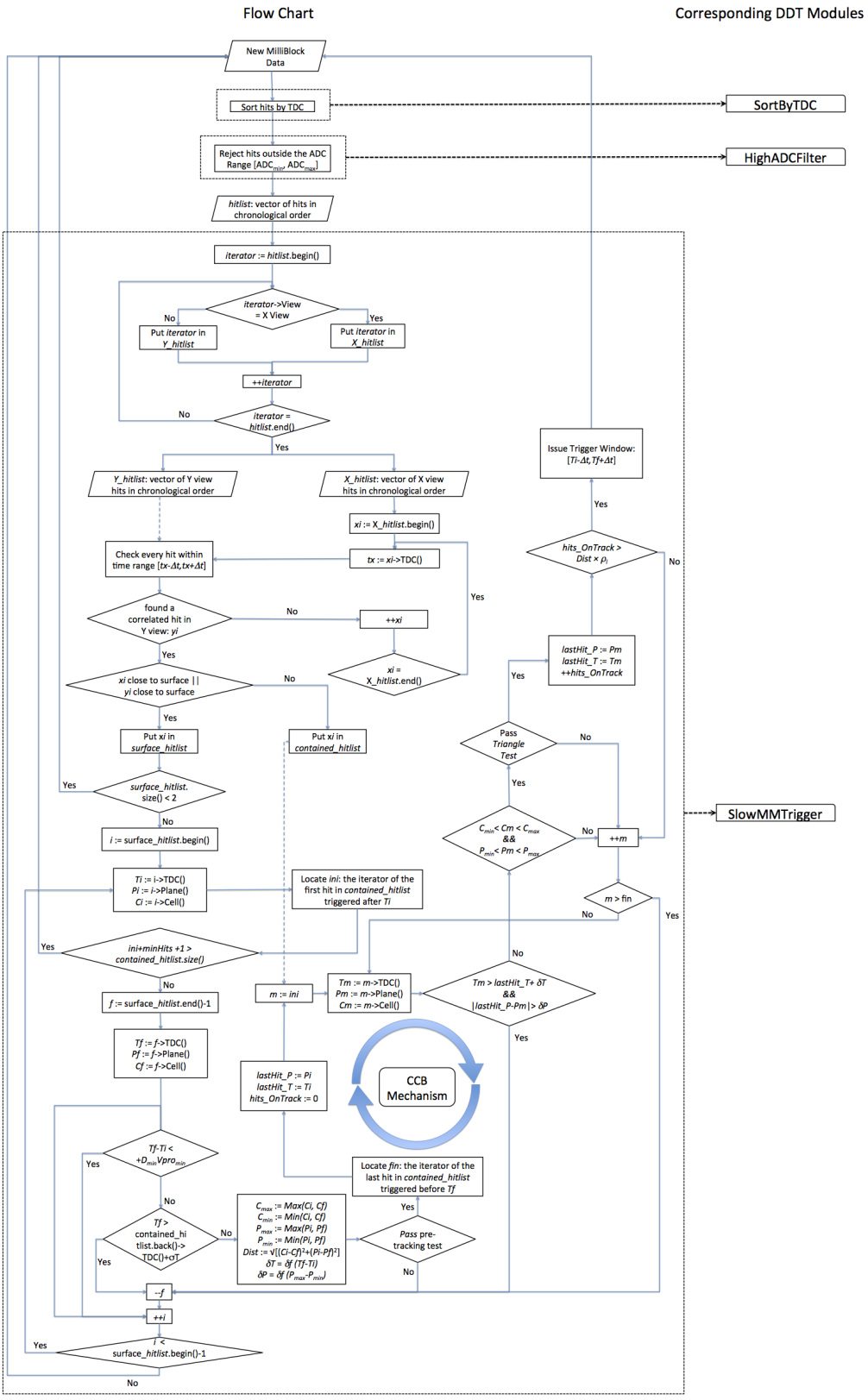

Figure A.4: The flow chart of the slow monopole trigger algorithm.

To further reduce the number of calculations of "entry" and "exit" hits, we implemented a "Continuity Check and Break" mechanism taking advantage of hits being sorted by time, as shown in the flow chart A.4. If an obvious "continuity break" has been discovered, we will move on to the next combination of surface hits.

A.1.2 Triangle Algorithm Complexity and computation time

The execution time of the slow monopole trigger algorithm is closely related to the number of surface hits (denote as N_s) and the number of contained hits (N_c). The total number of pairs of surface hits is proportional to N_s^2, as every contained hit is checked for fitting into every possible pair of surface hits. So, we define the complexity (C) of the triangle algorithm as following:

$$C = N_c \cdot N_s^2 \,. \tag{A.1}$$

The total computation time of the slow monopole trigger module should have a linear relation to the triangle algorithm complexity:

$$T = p \cdot C + t_0 \,, \tag{A.2}$$

where p is a scale factor to be fitted, and t_0 is the time needed for the preparation before processing the triangle algorithm, including assigning the surface hits and contained hits.

A test of the computation time for slow monopole trigger has been done with real environment and minimum bias far detector data. By varying the cuts in δP and δC (detector surface boundary cut in number of planes and cells, see Table A.1), we have different number of contained hits (N_c) and number of surface hits (N_s). And thus, we obtain different computation time with different complexity as shown in Fig. A.5.

The test result supported the simple model of relation between the complexity and computation time. The least χ^2 fit suggests $p = (9.6 \pm 0.3) \times 10^{-12}$ s and $t_0 = 1.4 \pm 0.1$ s.

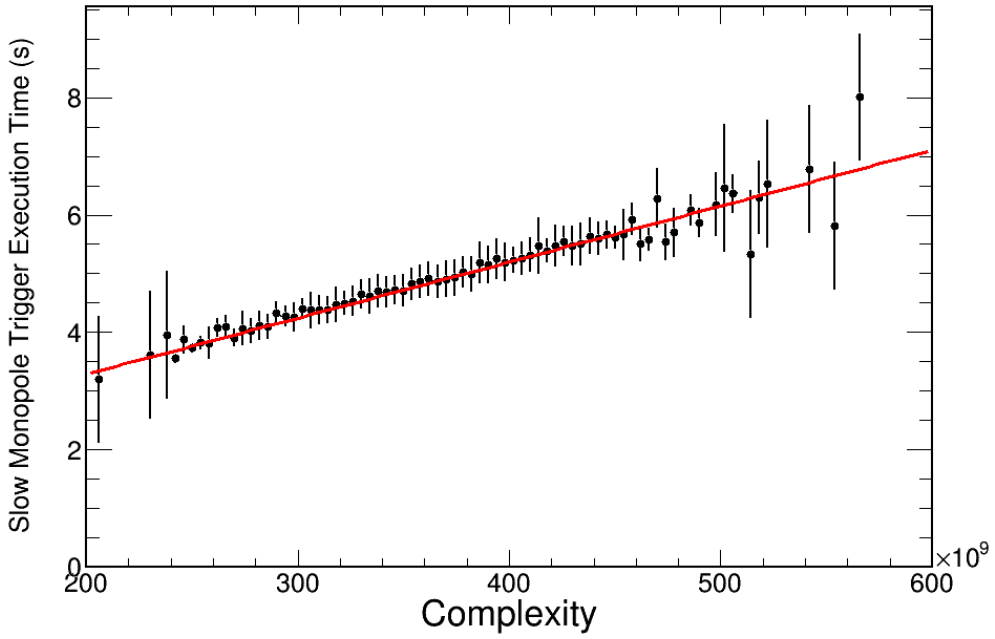

Figure A.5: The computation time of the slow monopole trigger as a function of complexity.

A.1.3 Slow Monopole Trigger Efficiency and Performance

Due to restrictions in computation time, we have to deploy a cut based on the DCS value to reduce the total number of hits in a milli slice, like what we have done in fast monopole trigger. We tested the efficiency of slow monopole trigger when different DCS cuts on hits were chosen, as shown in Fig. A.6.

Maximizing the efficiency while keeping the execution time within required time limits, we finally choose to filter hits with a DCS value less than 150 ADC (approximately 0.3 to 2.4 MIPs). The execution time is capped at 20,000,000 CPU ticks (around 2 seconds). If the slow monopole trigger cannot make a decision within that

time, a slow monopole trigger decision will be made using the time window of the current pair of surface hits. The trigger algorithm is designed so that the issued trigger time window is as small as possible without losing efficiency.

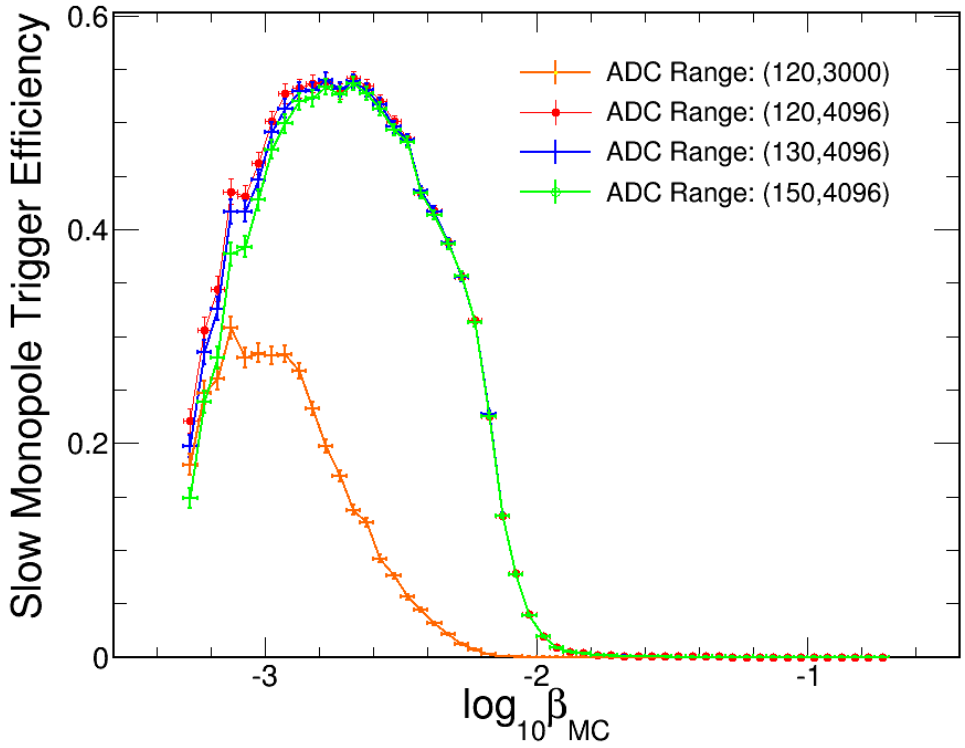

Figure A.6: The Monte Carlo estimation of the efficiency of the slow monopole trigger as a function of the monopole's velocity, based on the optimistic energy loss and light yield in the monopole simulation.

The slow monopole trigger rate is the lowest among all the data-driven triggers, as shown in Fig. A.7. The majority of the triggered events are caused by hitting the timing cap.

A.2 Combined Monopole Trigger Efficiency and Performance

The overall monopole trigger efficiency (either triggered by the fast or the slow monopole trigger), is shown in Fig. A.8. The execution time with real environment

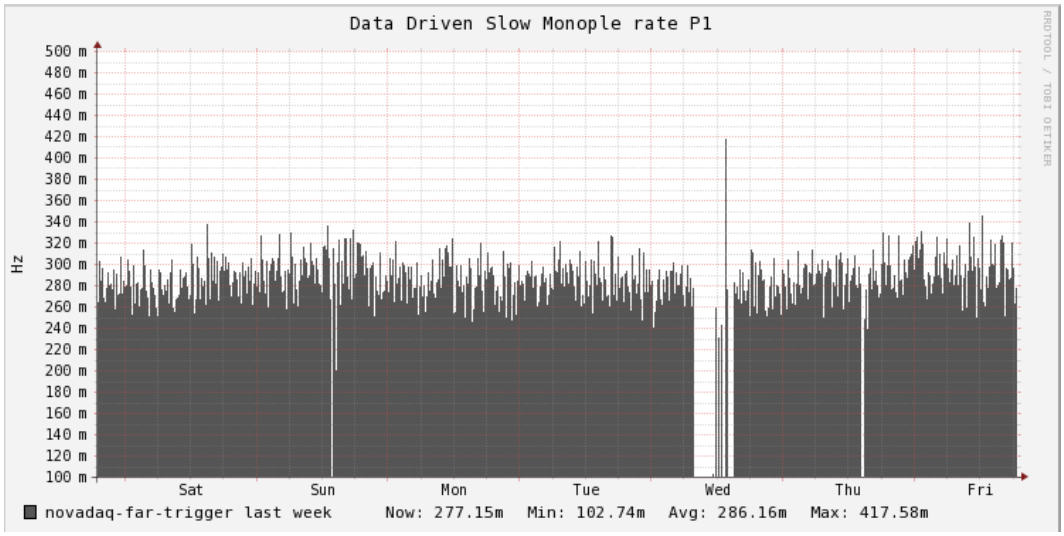

Figure A.7: The slow monopole trigger rate in the far detector in a week.

has also been examined for every module which is related to making monopole trigger decisions. Most of the modules take negligible time to finish, as shown in Fig. A.9. The slow monopole trigger, due to its more complicated algorithm, has a much wider distribution in execution time, though with a timing cap at 2 seconds.

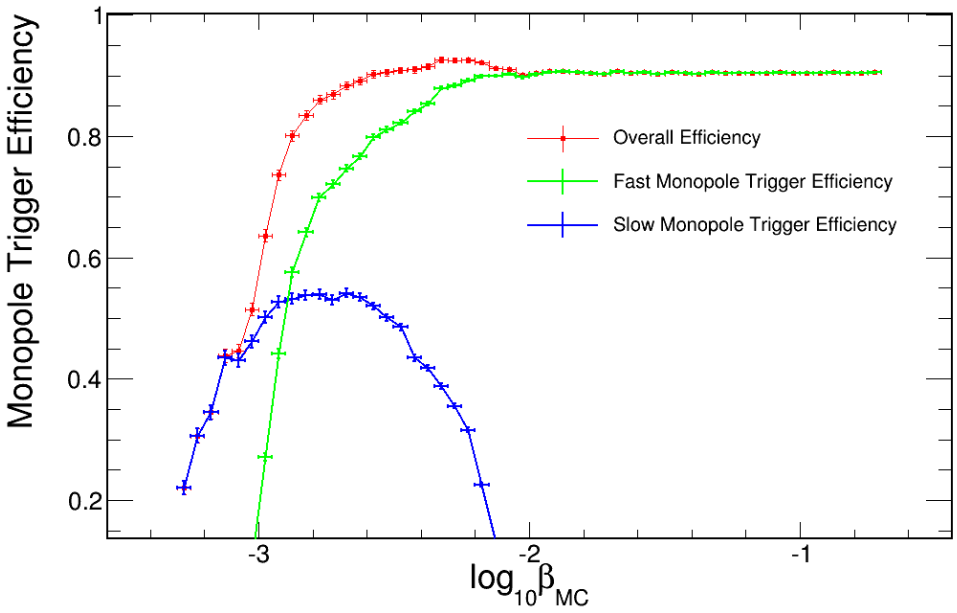

Figure A.8: The Monte Carlo estimation of the combined efficiency of both monopole triggers as a function of the monopole's velocity, assuming the optimistic energy loss and light yield in the monopole simulation.

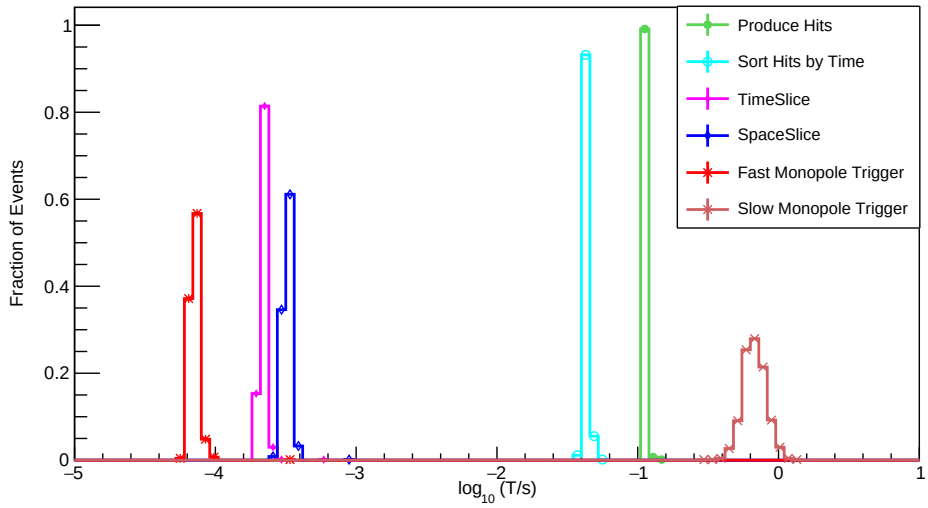

Figure A.9: The execution time of all the important modules related to the two monopole trigger decisions.

Bibliography

[1] J. D. Jackson, *Classical Electrodynamics*. (Wiley, Berkeley, 1975).

[2] G. ′t Hooft, *Nucl. Phys.* **B79**, 276 (1974).

[3] A. M. Polyakov, *JETP Lett.* **20**, 194 (1974).

[4] A. S. Goldhaber, *Phys. Rev.* **B140**, 1407 (1965).

[5] P. A. M. Dirac, *Proc. Roy. Soc. Lond.* **A133**, 60 (1931).

[6] A. Abulencia, et al. (CDF Collaboration), *Phys. Rev. Lett.* **96**, 201801 (2006).

[7] G. Aad, et al. (ATLAS Collaboration), *Phys. Rev. Lett.* **109**, 201803 (2012).

[8] W. N. Cottingham and D. A. Greenwood, *An Introduction to the Standard Model of Particle Physics*. (Cambridge University, Cambridge, 2007).

[9] H. Georgi and S. L. Glashow, *Phys. Rev. Lett.* **32**, 438 (1974).

[10] C. P. Dokos and T. N. Tomaras, *Phys. Rev.* **D21**, 2940 (1980).

[11] K. Nakamura, et al. (Particle Data Group), *J. Phys. G: Nucl. Part. Phys.* **37**, 075021 (2010).

[12] T. W. B. Kibble, *J. Phys.* **A9**, 1387 (1976).

[13] E. C. Katsavounidis, PhD thesis, (California Institute of Technology, June 1995).

[14] P. A. R. Ade, et al. (Planck Collaboration), *arXiv: 1303.5062* [astro-ph.CO].

[15] E. N. Parker, *Astrophys. J.* **160**, 383 (1970).

[16] E. N. Parker, M.S. Turner, and T.J. Bogdan, *Phys. Rev. Lett.* **70**, 2511 (1993).

[17] B. Cabrera, *Phys. Rev. Lett.* **48**, 1378 (1982).

[18] B. Cabrera, M. Taber, R. Gardner, M. Huber, J. Bourg, *Monopole '83*, 439 (1984).

[19] M. G. Aartsen, et al. (IceCube Collaboration), *arXiv: 1402.3460* [astro-ph.CO].

[20] C. N. Yang, Y. Kazama, and A.S. Goldhaber, *Phys. Rev.* **D15**, 2287 (1977).

[21] S. P. Ahlen, *Phys. Rev.* **D17**, 229 (1978).

[22] H. Bethe, *Ann. Phys. (Leipzig)* **5**, 325 (1930).

[23] F. Bloch, *Ann. Phys. (Leipzig)* **16**, 285 (1933).

[24] E. Fermi and E. Teller, *Phys. Rev.* **72**, 399 (1947).

[25] S. P. Ahlen and K. Kinoshita, *Phys. Rev.* **D26**, 2347 (1982).

[26] J. Lindhard, *Mat. Fys. Medd. Dan. Vid. Selsk* **28**, 8 (1954).

[27] V. P. Matem'yanov and S. K. Khakimov, *Zh. Eksp. Teor. Fiz* **62**, 35 (1972).

[28] L. M. Landau and E. M. Lifshitz, *Electrodynamics of Continuous Media*. (Addison-Wesley, New York, 1960).

[29] D. E. Groom, *Physics Reports*, **140**, 323 (1986).

[30] R. Abbasi et al., *Phys.Rev.*, **D87**, 022001 (2013).

[31] M. Ambrosio, et al. (MACRO Collaboration), *Eur. Phys. J.*, **C25**, 511 (2002).

[32] S. Balestra et al., *Eur. Phys. J.* **C55**, 57 (2008).

[33] D. S. Ayers, et al. (NOνA Collaboration), The NOνA technical design report (2007).

[34] S. Orito, M Imori, K. Yamamoto, H. Yamakawa, T. Suzuki, K. Anraku, M. Nozaki, M. Sasaki, T. Yoshida, K. Kuwahara, et al., *Phys. Rev. Lett.*, **66**, 1951 (1991).

[35] A. Norman, et al. (NOνA Collaboration), NOνA Document 4390, Fermilab (2014).

[36] S. Mufson, B. Baugh, C. Bower, T. Coan, J. Cooper, L. Corwin, J. Karty , P. Mason, A. Pla-Dalmau, M. Proudfoot, *arXiv: 1504.04035* [physics.ins-det] (2015).

[37] C. Backhouse, Intro to art tutorial, NOνA Document 11006 (2014).

[38] A. Aurisano and C. Backhouse, The NOνA simulation chain, NOνA Document 13370 (2015).

[39] A. V. Bagulya, M. S. Vladimirov, V. N. Ivanchenko, and N. I. Starkov, *Bulletin of the Lebedev Physics Institute, Vol.* **36**, No. 5, 127 (2009).

[40] J. B. Birks, *Proc. Phys. Soc.* **A64**, 874 (1951).

[41] V. I. Tretyak, *EPJ Web of Conferences* **65**, 02002 (2014).

[42] G. Bellini, et al. (Borexino Collaboration), *Phys. Rev.* **C81**, 034317 (2010).

[43] V. I. Tretyak, *Astropart. Phys.* **33**, 40 (2009).

[44] H. O. Back, et al. (Borexino collaboration), *Nucl. Instrum. Meth.* **A584**, 98 (2008).

[45] R. L. Craun and D. L. Smith, *Nucl. Instrum. Meth.* **80**, 239 (1970).

[46] C. Hagmann, D. Lange, and D. Wright, In *Nuclear Science Symposium Conference Record*, 2007. NSS'07. IEEE Vol. 2, 1143 (2007).

[47] J. N. Oliver, Signals and noise in the NOνA detector - analysis and simulation, NOνA Document 9384 (2009).

[48] J. Coelho, Fardet good runs tutorial, NOνA Document 12733 (2015).

[49] A. Hoecker, P. Speckmayer, J. Stelzer, J. Therhaag, E. von Toerne, H. Voss, M. Backes, T. Carli, O. Cohen, A. Christov, et al., *PoS ACAT* **040** (2007).

[50] J. Liu, Quantifying crosstalk in avalanche photodiodes used in the NOνA detector, NOνA Document 7992 (2012).

[51] L. Mualem, Light level tuning and data/mc comparisons, NOνA Document 13008 (2015).

[52] W. A. Rolke, A. M. Lopez, and J. Conrad, *Nucl. Instrum. Meth.* **A551**, 493 (2005).